Prediction of Fatigue Crack Propagation in Orthotropic Steel Decks using XFEM based on LEFM and VCCT

Ravi Shankar Gupta

4751310

TU**Delft** Delft University of Technology

Rijkswaterstaat
Ministerie van Verkeer en Waterstaat

Prediction of fatigue crack propagation in orthotropic steel decks using XFEM based on LEFM and VCCT

by

Ravi Shankar Gupta

in partial fulfilment of the requirements for the degree of

Master of Science

at the Delft University of Technology,

to be defended publicly on Friday July 19, 2019 at 11:00 AM.

Student number:	4751310	
Supervisor:	Prof. dr. M. Veljkovic,	TU Delft
Thesis committee:	MsEng. O. Joostensz,	Rijkswaterstaat
	Dr. Ir. F.P. van der Meer,	TU Delft
	Dr. H. Xin	TU Delft
	Ir. L.J.M Houben	TU Delft

An electronic version of this thesis is available at http://repository.tudelft.nl/.

TUDelft
Delft
University of
Technology

Rijkswaterstaat
Ministerie van Verkeer en Waterstaat

Acknowledgement

Summary

Orthotropic Steel Decks (OSDs) are widely used in various types of steel bridges due to their benefits of light weight, high load bearing capacity and speedy construction. Although many improvements in aspects of design, fabrication, inspection, and maintenance have been achieved over the years for such bridge decks, fatigue remains a predominant problem, mostly because of the complexity of prediction methods. Many researchers have tried to investigate this component through experiments. However, performing only experiments may not lead to a cost-effective solution. Therefore, it is necessary to combine the experimental data with the numerical approaches.

Particularly Linear Elastic Fracture Mechanics (LEFM) allows to model and analyse the crack propagation until subsequent failure, and significantly reduces the requirement of experiment. ABAQUS® provides an enriched feature, commonly referred to as the Extended Finite Element Method (XFEM) which incorporates two enrichment function namely the discontinuity function which represents the gap between the crack surface and asymptotic function which captures the singularity and thus can be used to model discontinuity independent to the finite element mesh. To evaluate the modelling efficiency and validate the simulation methodology, two XFEM-model based on LEFM and Virtual Crack Closure Technique (VCCT) are developed and the simulated results are compared with the experimental data.

The first phase of the thesis deals with the numerical simulation to investigate the crack propagation rate in Compact-Tension (CT) specimen for different stress ratios. The results of two-dimensional (2D) model are found to be in good agreement (within 1.48%) with the fatigue coupon test results. As most of the work concentrates on 2D shell model, the extension to three-dimensional (3D) solid requires the investigation of related parameters to consider through-thickness effects. Nevertheless, the mechanism of 3D model is studied, and the simulated results match with the 2D results for fatigue crack growth (a, N). Moreover, a reliable technique of computing Stress Intensity Factor (SIF) is obtained by comparing with the ISO 12108 standard formulation. However, when the SIF and fatigue crack growth are combined, the crack propagation rate in 3D is overestimated (about 26%) when compared to the experimental data possibly because of the imperfection in the application of boundary conditions.

The second phase deals with the numerical simulation in welded connection of OSD to determine the Paris law constants (C, m) by correlating the numerical result of fatigue crack growth with the beach mark measurements obtained in the fatigue experiments. Prior to automated XFEM simulation, a set of finite element analyses are performed to determine the vertical deformation, longitudinal stain distribution and hotspot stresses to validate the numerical model as per the test setup. The results of numerical analyses showed a good correlation (within 18%) with test data and Paris law constant C is predicted to be lower than the recommended value by IIW standard.

The validated methodology is then applied on large scale to an existing bridge (Suurhoff bridge) structure which was built in 1971. In this case study, a crack length of 230 mm was detected in the deck plate originating from the root of the stiffener-to-deck plate welded connection between the cross-beams using TOFD measurements. To verify the problem, a numerical model is developed based on the dimension of the bridge to evaluate the crack initiation period and the crack propagation period. The crack initiation period is predicted using hotspot stress method and the crack propagation period is evaluated using automated XFEM simulation. Overall, the total fatigue load cycles are predicted to be 7.86 million which is equivalent to 48 years. A similar crack length was however detected after a service life of 44 years. This overestimation can be possibly explained as the model did not take residual stresses and other welding defects into account. The numerical model showed a good correlation with the real scenario and is therefore used to predict the permissible limit of deck plate crack length of 500

mm. The model predicted 8.02 million load cycles for a crack length of 500mm, which is equivalent to 34 years after the crack initiation period. Nevertheless, the fracture mechanics approach showed improvements in the assessment of fatigue life.

List of Abbreviations

2D	Two-dimensional
3D	Three-dimensional
ASTM	American Society for Testing and Materials
CCRB	Circumferentially Cracked Round Bars
CT	Compact-Tension
FE	Finite Element
FEM	Finite Element Method
HAZ	Heat Affected Zone
IIW	International Institute of Welding
ISO	International Organization for Standardization
LEFM	Linear Elastic Fracture Mechanics
OSD	Orthotropic Steel Deck
PHILSM	Signed function to describe the crack surface
PSILSM	Signed function to describe the initial crack front
RP	Reference Point (ABAQUS®)
RWS	Rijkswaterstaat
SEM	Scanning electron microscope
SIF	Stress Intensity Factor
STATUSXFEM	Status of the enriched element
TOFD	Time-of-flight-diffraction
VCCT	Virtual Crack Closure Technique
XFEM	eXtended Finite Element Model

List of Symbols

$2c$	Crack length
a	Crack size
C, m	Material dependent parameters of the Paris Law
C_1, C_2, C_3, C_4	Material constants based on fracture energy release rate
E	Elastic modulus
G_{pl}	Energy release rate upper limit
G_{thres}	Energy release rate threshold
N	Number of load cycles
R	Stress ratio
ΔF	Applied load range
ΔK	Stress Intensity Factor range
ΔK_{eff}	Effective Stress Intensity Factor range
υ	Poisson's ratio

Contents

List of Figures

List of Tables

Chapter 1

INTRODUCTION

1.1 Background information

1.1.1 Motivation

Structural components are often found to fail under stresses below the ultimate or even below the yield stresses in the presence of fatigue loading. The fatigue phenomenon is due to micro-cracks initiation, nucleation and gradually forms macrocracks [1]. The macrocracks will propagate under cyclic loading. The conventional static strength analysis is not enough to predict the service behaviour of steel structures. Therefore, over the past few decades many scientists and structural engineers have focussed their attention to fatigue fracture problems while designing and analysing structural components. Orthotropic steel decks (OSDs) are one of such typical structural components which has suffered from fatigue problems over the past decades. Although many improvements in aspects of design, fabrication, inspection, and maintenance have been achieved for such bridge decks, fatigue remains its predominant problem, mostly because of the complexity of prediction methods. One of the critical fatigue details is the welded connection between the deck plate and the longitudinal stiffener due to direct contact of wheel load and its corresponding high-stress ranges. The closed stiffeners restrict the transversal movement of the deck plate making this critical detail prone to fatigue failure. Many researchers have tried to investigate this detail through experiments [2]. However, performing only experiments may not lead to a cost-effective solution. Therefore, it is necessary to combine the experimental data with the numerical approaches and preferably assuming basic material properties to predict behaviour of critical details.

1.1.2 Methodology

Methods based on fracture mechanics could be used to model and analyse the fatigue crack propagation and subsequent failure of the structure. These methods have already shown their reliability in the aerospace and automobile industry. The use of Linear Elastic Fracture Mechanics (LEFM) model has several advantages as it significantly reduces the requirement of experiments. Furthermore, this method can predict the crack propagation until subsequent failure, which implies that the total fatigue life of the structure can be predicted for a certain crack length. Therefore, remaining lifetime predictions could be made for existing bridges [3].

ABAQUS® provides an enriched feature, commonly referred to as the Extended Finite Element Method (XFEM) to model discontinuity independent to the finite element mesh. This removes the requirement of the modelling domain and mesh to correspond to each other explicitly. Using XFEM, it is possible to evaluate automated crack propagation by arbitrarily inserting the crack into the existing model. The mesh around the crack tip should be sufficiently small to have to get an accurate prediction which leads to the high computational effort. Two options are available to model crack propagation, either by cohesive segment method or the linear elastic fracture mechanics (LEFM) approach in conjunction by phantom nodes [4].

Therefore, to understand the fatigue crack propagation mechanism is essential to study the mechanics of the material involved such development microcracks, defects, etc. This information together with the understanding of the basis of the XFEM is essential to better understand and analyse the simulation results.

1.2 Research Objective

The main objective of this research is to numerically model and verify the problem of fatigue crack propagation using XFEM-model based on LEFM which can be summed up in two main questions.

1. **How to model the fatigue crack propagation in Compact Tension (CT) -specimen and in welded connection (rib-to-deck plate) of an Orthotropic Steel Deck (OSD) using XFEM based on LEFM?**

How to implement the material parameters and formulate Paris law in the XFEM model for numerical simulation of fatigue crack propagation?

2. **What is the accuracy of XFEM model developed for this research when compared with the experimental/inspection data to predict the fatigue crack propagation?**
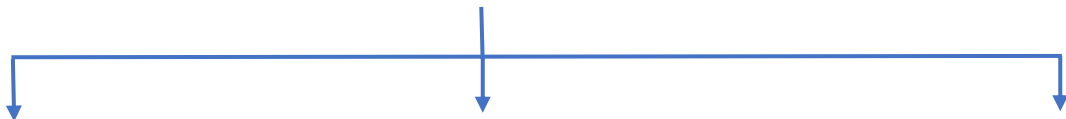
2.1. Compact-Tension (CT) Specimen	2.2. Orthotropic Steel Deck (OSD) Specimen	2.3. Suurhoff Bridge

2.1. What is the accuracy of XFEM model developed in this research to predict the fatigue crack propagation rate in CT-specimen for different stress ratios?

2.2. How to predict the Paris law constants (C and m) using XFEM-model based on the beach mark measurement?

2.3. What is the total fatigue life (crack initiation period and crack propagation period) of the Suurhoff bridge (existing bridge) based on numerical analyses in welded connection (rib-to-deck plate) of an Orthotropic Steel Deck (OSD)?

1.3 Thesis Structure

In order to approach the main objectives of this research project, it is essential to divide the workflow into distinctive parts. Hence, the chapters are categorised based on the numerical model and the methodology is discussed below.

Chapter 2 illustrates some fundamental information in understanding the linear elastic fracture mechanics. Some valuable insight on the evolution of fatigue crack is discussed, mainly focussing in the welded joint between the deck plate and the longitudinal stiffener. In addition to that, some basic of numerical XFEM feature in ABAQUS® is covered.

Chapter 3 deals with the prediction of fatigue crack propagation rate in CT-specimen using 2D-XFEM and 3D-XFEM model for several stress ratios. The simulated results are compared with the experimental data, to determine the efficiency of assumed parameters. The mechanism of 3D-XFEM is studied and the results are compared with 2D-XFEM. In addition to that, the effect of LEFM parameters on crack propagation is discussed.

Chapter 4 deals with the prediction of fatigue crack growth in OSD using XFEM-model. The simulated results are correlated with the beach marks measurements, to estimate the Paris law constant C and m. Prior to crack simulation, some static analyses such as deformation, strain measurement, and hot-spot stress were performed, and the results are compared with the experimental data to ensure actual behaviour of the test specimen.

Chapter 5 involves in developing a numerical model to predict the crack initiation period and the crack propagation period of Suurhoff bridge (existing bridge). The simulated results are compared with the inspection data (TOFD measurement) and/or existing numerical model to determine the accuracy of the numerical model and to verify the problem.

Finally, chapter 6 contains a set of conclusions drawn from this research and corresponding answers to the research questions. In addition, some recommendations are made for further research in improving the XFEM model on this topic.

Chapter 2

THE STATE OF THE ART (LITERATURE OVERVIEW)

2.1 Linear Elastic Fracture Mechanics (LEFM)

Linear elastic fracture mechanics was first introduced by A. A. Griffith [5], to explain the behaviour of flaw in materials [3]. He proposed a relation that the product of the square root of the flaw length a and the stress at fracture σ_f is nearly constant (equation 2.1). He tried to illustrate this relation in terms of linear elastic theory. As this approach showed some problems as the stress (or strain) at the tip of a sharp flaw in linear elastic material was infinite. Later, this theory was therefore explained taking energy considerations through thermodynamic approach, which was later modified by Irwin [6].

$$\sigma_f \sqrt{a} \approx C \tag{2.1}$$

2.1.1 Crack characterization

Crack geometry

The extreme ends of the crack can be considered as crack tip. If the crack is considered in two-dimensional (line), the crack tip is a single point. Whereas, if the crack is analysed in three-dimensional, then the crack tip can be complex crack front. This complexity depends upon the crack propagation in through-thickness direction. Such type of fatigue which propagates through the entire thickness can be referred as through cracks (Figure 2.1). Moreover, the crack front is generally curved in thick materials. Such cracks are referred as part through cracks (Figure 2.1-corner cracks and surface crack). The first conditions can be treated as the 2D-crack tip region can be used, while the later will lead to more complex 3D crack tip region [7].

Both the types of crack are characterized by a cartesian coordinate system (x, y, z) and polar reference system (r, θ) with x lying on the uncracked region and z being the tangent to the crack line.
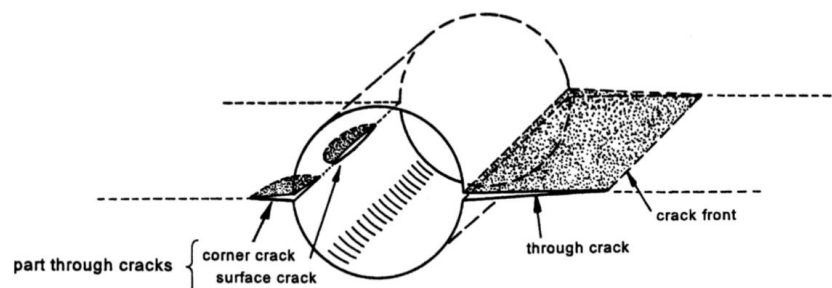
Figure 2.1 Different crack types [3]
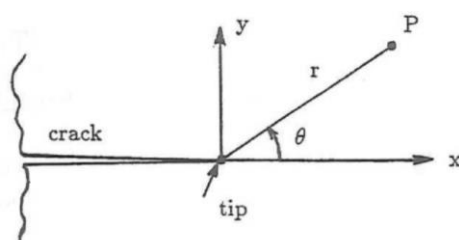
Figure 2.2 Crack tip region- 2D [4]
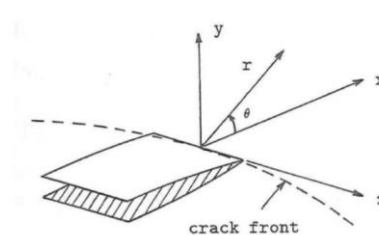
Figure 2.3 Crack tip region-3D [4]

Crack propagation

It is true that direction of crack growth derives from the stress intensity distribution along the crack front and the rate of propagation depends of the magnitude of the stress intensity factor however, 3D problems are more complex and are associated with the mechanistic phenomenon known as crack closure effect. A typical example of crack propagation direction is shown in Figure 2.4 for curved crack front in through thickness direction and an elliptical crack front situated at the surface.
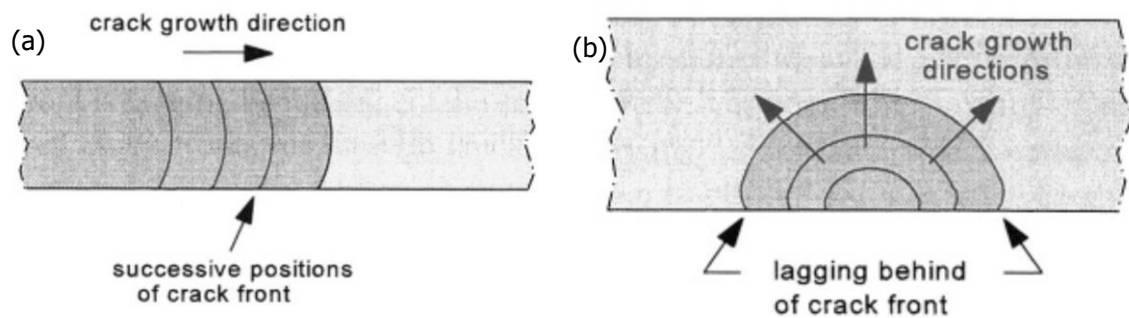
Figure 2.4 Crack closure effect at the material surface on crack front shapes [8]: (a) Through crack- Curved crack front (b) Deviations of semi-elliptical crack front at material surface

Fracture modes

There are three ways that a crack can extend namely Mode I, Mode II and Mode III.   From Figure 2.5, Mode I is referred as opening mode where the crack surface moves apart; Mode II is referred as sliding mode (in-plane shear mode) where the crack surface slide apart perpendicular to the crack front; and Mode II is referred as tearing mode (anti-plane shear mode) where the crack surface slides apart parallel to the crack front. Mode I is considered as most common and important in crack growth analysis because the crack developed under pure shear loading quickly transit to a tensile mode [9].
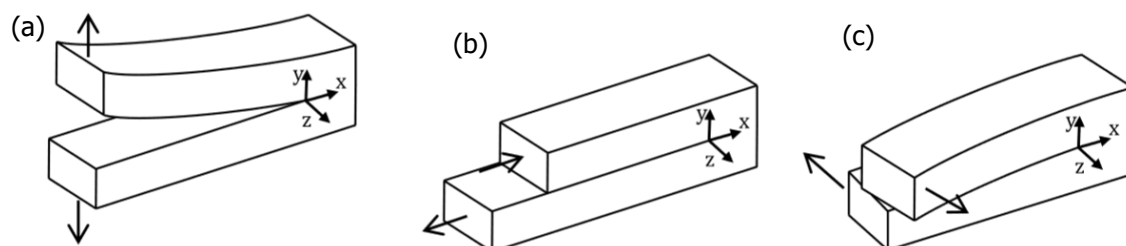
Figure 2.5 Fracture modes a) Mode I b) Mode II c) Mode III [9]

2.1.2 Stress intensity factor

The Griffith criterion

Griffith criterion states that the crack extension Δa in a plate of thickness t is only possible "if the work done by the applied force is more than or equal to the summation of the change in the elastic energy and the energy absorbed at the crack tip, then it will lead to unstable fracture" [10]. This statement can be represented as

$$dW_e \geq dU^{el} + G_c t \Delta a \tag{2.2}$$

where dW_e implies the work done to form a crack extension Δa, dU^{el} is the change in elastic strain energy and G_c is the critical energy release rate which signifies the toughness of the material or extension of crack. For a simple case, the failure in an infinite plate with central crack can be expressed as (equation 2.3) in terms of critical energy release rate in relation with critical stress (σ_c).

$$G_c = \frac{\sigma_c^2 \pi a}{E} \tag{2.3}$$

which can be further related in

$$\sigma_c \sqrt{\pi a} = \sqrt{G_c E} = K_{IC} \tag{2.4}$$

where K_{IC} denotes the fracture toughness of the specimen. The stress intensity factor can be expressed in $N.mm^{3/2}$ or $MPa\sqrt{m}$. Through the fundamental definition, the potential energy P is related to the crack growth da proposed by Irwin [8]

$$G = -\frac{dP}{da} \tag{2.5}$$

From equation 2.5 and equation 2.3, the most important relation can be derived as the change in potential energy to close a small section of crack da, equating with the quantity to the work required to close that section of crack without any external effort.

The following equation (2.6 and 2.7) [10] is valid for different crack mode, when plane stress situation is assumed.

$$G = \frac{1}{E}\left(K_I^2 + K_{II}^2\right) + \frac{(1+v)}{E} K_{III}^2 \tag{2.6}$$

Similarly, when the plane-strain situation is assumed:

$$G = \frac{1-v^2}{E}\left(K_I^2 + K_{II}^2\right) + \frac{(1+v)}{E} K_{III}^2 \tag{2.7}$$

11

Fatigue crack propagation regime

Paris and Erdogan [11] studied crack growth behaviour through experiments and found a relation between the crack growth rate da/dN and the stress intensity factor range ΔK. Additional test indicated two vertical asymptotes occur when da/dN is plotted against the ΔK in log-log scale. The two extreme asymptotes indicate the start and the end of the crack life. More precisely, the left asymptote at $\Delta K = \Delta K_{th}$ signifies that K-values below this threshold level are two low to cause crack growth. On the other side, the right asymptote at $K_{max} = K_c$ signifies for a ΔK cycle with $K_{max} = K_c$ reaches a critical value which leads to complete failure of the structure. With these two vertical asymptotes the function can be divided into three different regimes as I, II and III illustrated in Figure 2.6 as (i) the threshold fatigue crack propagation regime (ii) the fatigue crack propagation regime and (iii) the near unstable fatigue crack propagation regime respectively. Therefore, the fatigue crack propagation regime can be formulated as:

$$\frac{da}{dN} = C\Delta K^m \qquad (2.8)$$
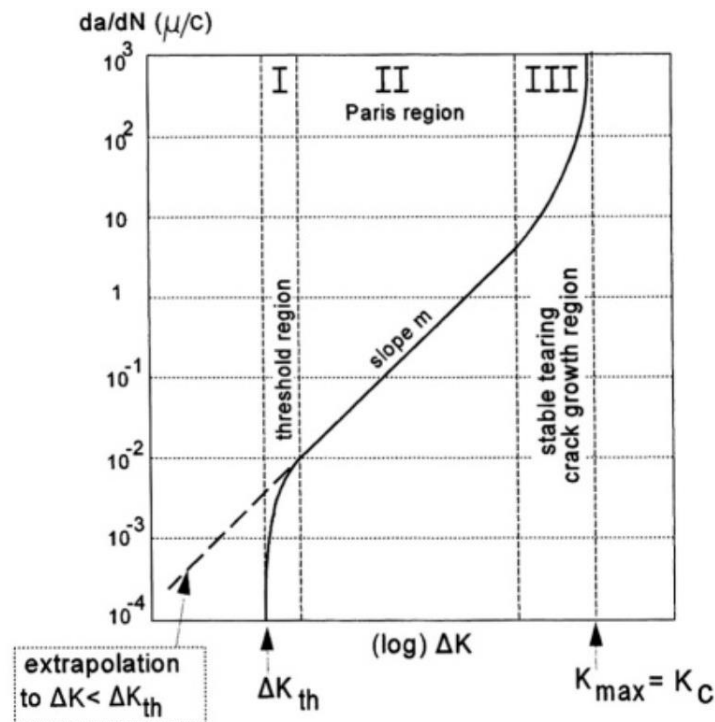
Figure 2.6 Three regime of the crack propagation rate as a function of ΔK [8]

12

2.2 Fatigue of welded connections

Fatigue crack development

In general, fatigue can be attributed to the crack development until complete fracture after ample amount of stress fluctuation. Thereby in context of fatigue, the lifetime of structure can be divided into three stages: fatigue crack initiation, fatigue crack propagation and final failure.

The crack nucleation stage can be stated as the period from an initial defect to the detectable crack. According to [12], this stage can be further subdivided into two phases: microstructural and mechanical (Figure 2.7).
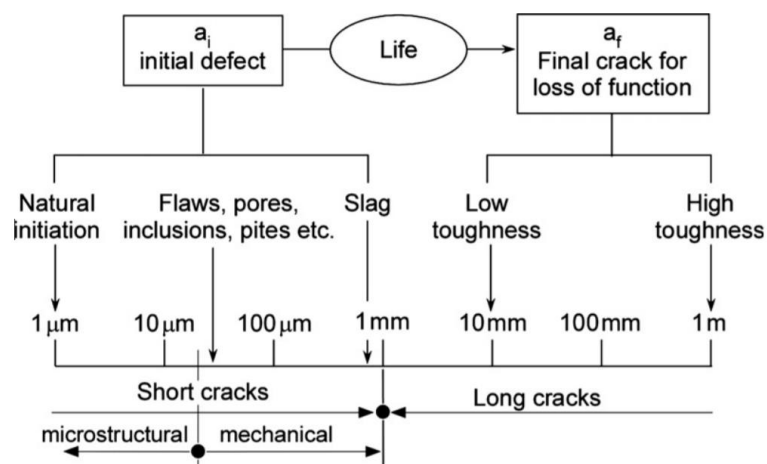
Figure 2.7 Length scales of the life cycle of a component subjected to cyclic loading [12]

In the first phase, the crack develops due accumulation of irreversible plastic deformation at pre-existing defects such as pores, inclusions, etc. which acts as the micro-notches. However, the crack is still small which can be comparable to the dimensions of the grain size and therefore it is attributed as microstructurally short crack. These cracks extend and tries to overcome the microstructural barriers (twin or grain boundaries) when the applied stress range is high enough. Once the crack encloses the number of grains the influence of local microstructural characteristics diminishes. As a result, the crack propagation in the next phase becomes steadier and these cracks can be attributed as mechanically short cracks. However, these crack still does not behave by the linear elastic K factor due to crack closure effects.

For non-welded components, the crack initiation stage covers the majority portion of total fatigue life. In contrast, the crack initiation stage is comparatively small for welded component due to welding defects and residual stresses. Lack of penetration, lack of fusion, slag inclusion, linear porosity (gas), sagging, undercut, overlap, excess of weld metal, incompletely filled groove are common examples of welding defect. Furthermore, poor workmanship can significantly decrease the fatigue strength. Although, these defects are sometimes unavoidable but with the help weld improvement techniques fatigue strength can be significantly enhanced. Grinding, re-melting, peening, coining, overstressing are some common weld improvement techniques. These techniques are used to reduce the stress concentration, to remove crack like defects at the weld toe and harmful tensile residual stress.

Deck-to-Rib welded joint

Orthotropic steel decks (OSDs) are one of such typical structural components which suffered from fatigue problems. One of the critical fatigue details is the welded connection between the deck plate and the longitudinal stiffener due to direct wheel loading and local high stress ranges

For this type of welded connections, there are four types of possible crack paths.

Crack I: initiates at the weld toe in the deck plate and propagates through the deck plate.
Crack II: initiates at the weld root and propagates through the deck plate.
Crack III: initiates at the weld toe in the trough web and propagates through the trough web.
Crack IV: initiates at the weld root and propagates through the weld throat.
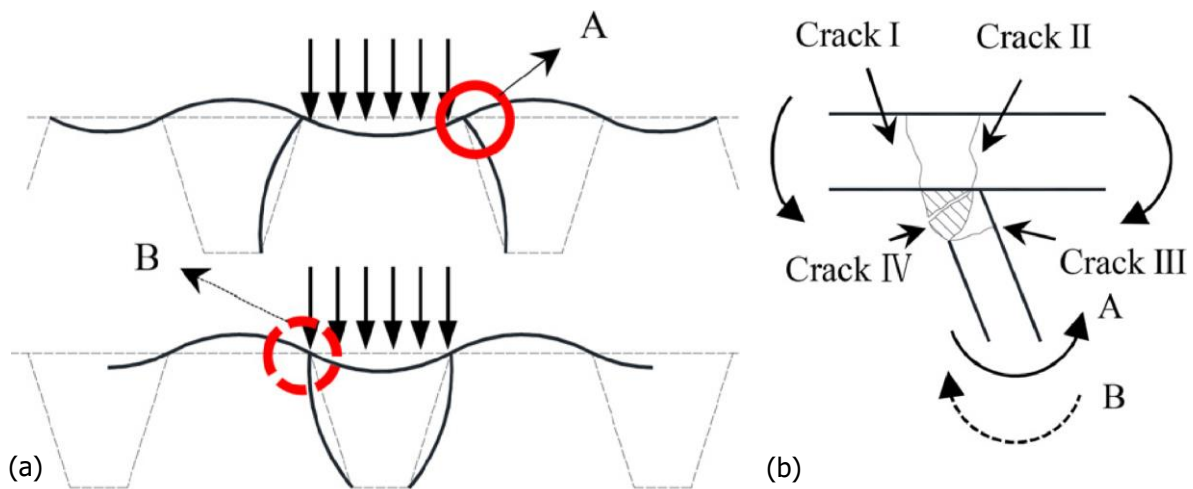
Figure 2.8 Illustration of the deformation and cracks of the bridge deck [13]: (a) Representative loading scenarios and the corresponding deformations (b) Typical fatigue crack patterns

Fatigue crack originating from the weld root propagate simultaneously in both vertical (through-thickness of the deck plate) and longitudinal directions, thus becoming large invisible cracks which are not detected until it damages the wearing surface. The significant effect due to out-of-plane bending moment between the deck plate and the trough induced by vehicles can pose serious threat to the structure's integrity and service life when the length becomes large [14].

Furthermore, several researchers have tried to investigate this detail through experiments and numerical approaches which can be summarised as follows:

- ✓ (Nagy, Backer, & Bogaert) [3] studied crack propagation behaviour in deck-to-rib detail of Temse bridge in Belgium. Two approaches namely the traditional approach (Palmgren-Miner hypothesis and SN-curves) and the fracture mechanics approach were performed and compared. To investigate the problem, they used an FEM-model to predict the number of cycles needed for a crack length of 600 mm. Approximately 38.5×10^6 load cycles was evaluated which is more than the traditional calculations (21×10^6 load cycles). However, this difference was justified as they did not take residual stresses and other welding defects into account in their model. Nevertheless, this paper showed a sign of improvement in

calculation of fatigue by use of fracture mechanics. As a continuation of work [15], a crack length of 461.703 mm was evaluated based on XFEM-simulation followed by exponential extrapolation, while a crack length of 600 mm was detected in reality. However, their model did not consider any residual stresses, which is most likely to be present in weld especially because multiple welds intersect at the crack location and the welds were not chamfered. Even though the residual stresses were not implemented, such results showed that fracture mechanics can be used for improved fatigue life assessment. Further, an improved analysing tool using LFEM and XFEM [16] evaluated the thickness effects for both, deck plate and longitudinal stiffener incorporating the residual stresses into their model. Based on the result, the authors concluded that the fatigue life increases with increase in thickness of deck plate while this is not the case with longitudinal stiffener thickness.

✓ In the analytical study (Xiaochen et. al) [17] on crack propagation behaviour based on FEA (Finite Element Analysis) and fracture mechanics. In analysing the crack direction, SIF under the mixed modes I, II and III were considered which indicated the complexity of stress field around the fatigue crack. Their numerical results showed that the crack direction change was due to Mode II and Mode III deformations near the crack tip caused by the out-of-plane bending of the rib wall along the crack. In addition to this, they also claimed that the crack direction could be evaluated by investigating the equivalent stress intensity factor.

2.3 XFEM (eXtended Finite Element Method)

In modelling a crack with traditional finite element method, it is necessary to refine the mesh around the crack in order to capture the singular asymptotic field accurately. Furthermore, modelling a growing crack can be even more cumbersome as the mesh should be at every crack propagation step to match the discontinuity. On the other hand, XFEM alleviates the drawbacks associated with meshing crack surfaces.

The XFEM was first developed by Belyschko and Black (1999) [18], an extension of the traditional finite element method based on the concept of partition of unity by Melenk and Babuska (1996) [19]. Two enrichment functions are incorporated in XFEM namely the discontinuity function $H(x)$ which represent the gap between the crack surfaces and asymptotic function $F_a(x)$ which capture the singularity around the crack tip. These functions are enriched with nodal degree of freedom $(\vec{a}_I, \vec{b}_I^a)$ and the vector function $\vec{u}$ with the partition of unity enrichment can be defined by the following equation:

$$\vec{u} = \sum_{I=1}^{N} N_I(x)\left[\vec{u_I} + H(x)\vec{a_I}\right]$$ (2.9)

where $N_I(x)$ is the nodal shape function; $\vec{u}_I$ represent the nodal displacement vector associated with the continuous part of the finite element solution.

However, the terms (equation 2.9) are associate with different domains. For instance, the 2nd term $H(x)$ in only applicable to the nodes with the discontinues function (crack interior), while the last term is applicable to the crack tip enrichment function (crack tip) and the 1st term $\vec{u_1}$ is associated to all nodes in the model. H(x) is the discontinuous jump function across the crack surface shown in Figure 2.9(a) is given in equation (2.10)

$$H(x) = \begin{cases} 1 & if\,(\vec{x} - \vec{x}^*).\vec{n} \geq 0 ; \\ -1 & otherwise \end{cases}$$ (2.10)

where $\vec{x}$ is a Gauss point, $\vec{x}^*$ is the point on the crack closest to $\vec{x}$ and $\vec{n}$ is the unit outward normal to the crack at $\vec{x}^*$.

(a)

Crack tip

Crack tip

X

s

n

s

n

r θ

n

s

X*

X*

X

X

(b) Blending elements

Enriched elements

Crack tip element

□ Crack tip function

○ Jump function
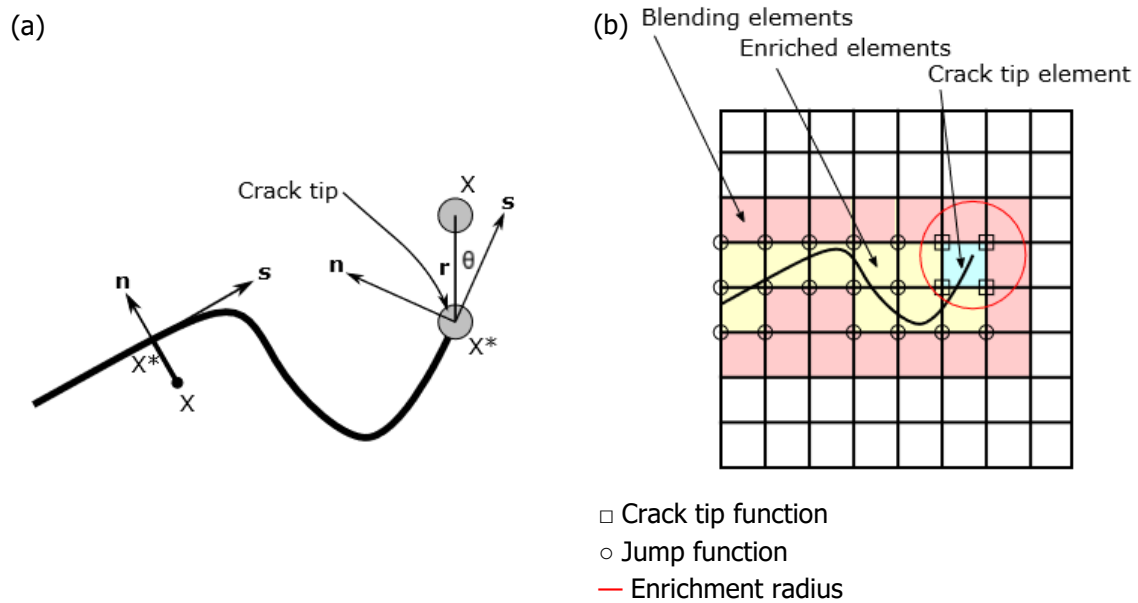
— Enrichment radius

Figure 2.9 (a) Representation of normal and tangential coordinates for a smooth crack. [4] (b) Representation of enriched nodes and enrichment radius in an arbitrary 2D mesh

An arbitrary crack in 2D mesh is illustrated in Figure 2.9(b). The nodes highlighted with square shape are associated with both the enrichment functions and responsible for capturing the singularity around the crack tip. Moreover, ABAQUS® provides the user the freedom to define the enrichment radius highlighted with circle (red) indicating the crack domain. Besides that, the nodes highlighted with circle (black) are only associated with discontinuous function. However, a more complex three-dimensional crack is represented using the level set method which is being used for analysing and computing interface motion. A description of such discontinuous geometry is illustrated in Figure 2.10.

orthogonal surface ($\psi = 0$)

crack surface ($\phi = 0$)

$\mathbf{m}^+$

$\mathbf{n}^+$

crack front (intersection of ψ and ϕ)
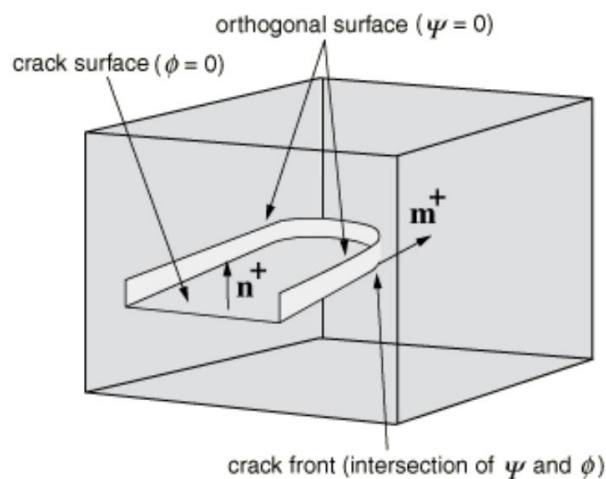
Figure 2.10 Illustration of a non-planar crack in the 3D by two signed distance function $\emptyset$ and ω [4]

17

The behaviour of the XFEM-based LEFM for automated crack propagation analysis is determined based on modified VCCT. XFEM enriched feature in ABAQUS® can be used to simulate crack propagation by using the direct cyclic approach in combination with Paris law formulation. The former setting provides the user to define a cyclic loading sequence (periodic, decay, user-define etc) while the latter setting defines the crack propagation, which adds more degree of freedom through XFEM. The direct cyclic simulates the cyclic load and requires the definition of a periodic function (for example-equation 2.12), which will be used by the software to apply the amount of load at its corresponding time.

$$x = A_0 + A_1 \cos(t - t_0) + B_1 \sin(\omega(t - t_0)) \tag{2.12}$$

The crack growth is described using Paris law, which is based on relative fracture energy release rates (Figure 2.11).
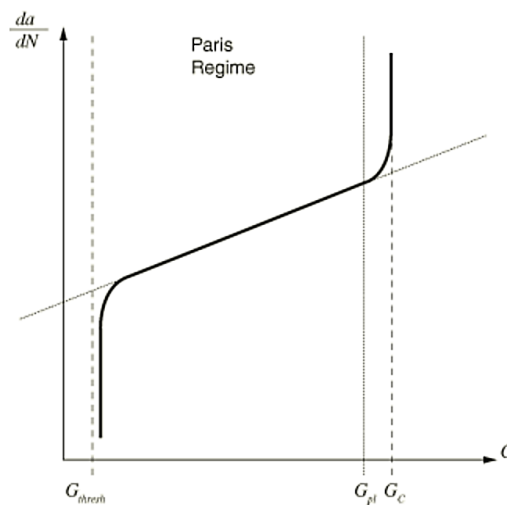
Figure 2.11 Fatigue crack growth [4]

The onset of the crack propagation indicates the starting of fatigue crack growth can be defined as (equation 2.13):

$$f = \frac{N}{C_1 \Delta G^{C_2}} \geq 1.0 \tag{2.13}$$

where ΔG is the relative fracture energy rate between its maximum and minimum values. Furthermore, the crack growth rate using Paris law can be formulated as (equation 2.14) only if $G_{thresh} < G_{max} < G_{pl}$:

$$\frac{da}{dN} = C_3 \Delta G^{C_4} \tag{2.14}$$

Abaqus® provides three common mixed mode model for evaluating the equivalent fracture energy release rate G_{equivC}: the BK law, the Power law and the Reeder law [4] . Although the choice of model

is not well defined for a given analysis, the most commonly used model is power law which can be illustrated as (equation 2.15):

$$\frac{G_{equiv}}{G_{equivC}} = \left(\frac{G_I}{G_{IC}}\right)^{a_m} + \left(\frac{G_{II}}{G_{IIC}}\right)^{a_n} + \left(\frac{G_{III}}{G_{IIIC}}\right)^{a_o}$$ (2.15)

Chapter 3

COMPACT-TENSION SPECIMEN

3.1 General

Compact-Tension (CT) specimen is a notched sample which is used to generate a fatigue crack through cyclic loading. Such specimens are standardised in accordance to ISO [20] and ASTM [21] , are extensively used in the field of fracture mechanics, to evaluate the material parameters through experiments. Fatigue being the predominant problem in steel infrastructure, such notched samples are good representation of real-life inconsistencies (discontinuities) introduced during manufacturing of steel products. Many researchers [22] have tried to investigate the fatigue behaviour of CT-specimen through experiments. However, performing only experiments may not be a cost-effective solution. Therefore, it is necessary to combine the experimental data with numerical approaches and preferably assuming basic material properties to predict behaviour of critical detail.

Numerical model based on fracture mechanics approach can be used to analyse fatigue crack propagation and has already shown its reliability. Commercial software such as ABAQUS® incorporates XFEM techniques to model discontinuities as an enriched feature. Using XFEM, it is possible to simulate automated crack propagation by inserting the crack into the model.

The main objective of this chapter is to predict the crack propagation rate for different stress ratios of CT-specimen using 2D and 3D XFEM-model based on LEFM and VCCT. To evaluate the efficiency of the assumed parameters, the simulated results are compared with the results of fatigue coupon tests [22]. The simulated results of crack propagation rate with different stress ratios were also studied and correlated with Elber's equation to study the crack closure mechanism. As the majority of works in LEFM concentrates on 2D shell model, the extension to three-dimensional (3D) solid requires the investigation of some parameters mainly through-thickness effect. Firstly, the mechanism of crack propagation will be studied and results of fatigue crack growth (a,N) will be compared with the 2D results. Secondly, an investigation is performed in determining a reliable technique to compute Stress Intensity Factor (SIF). Finally, the crack propagation rate in 3D is determined and will be compared with the test result.

3.2 XFEM model

3.2.1 Geometry
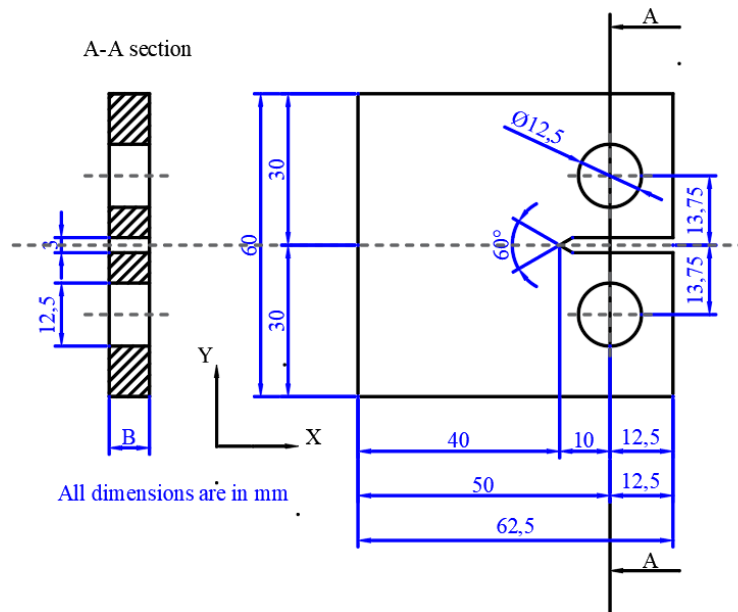
Figure 3.1 Geometry of CT-Specimen [22]

The set of simulation carried out in an adequate manner according to the experiment [22]. A full scale XFEM-model is developed based on the dimensions shown in the Figure 3.1. Moreover, the thickness of specimen is different for different stress ratios (see Table 3.2). The crack propagation behaviour is analysed using both 2D-XFEM and 3D-XFEM model.

3.2.2 Boundary conditions
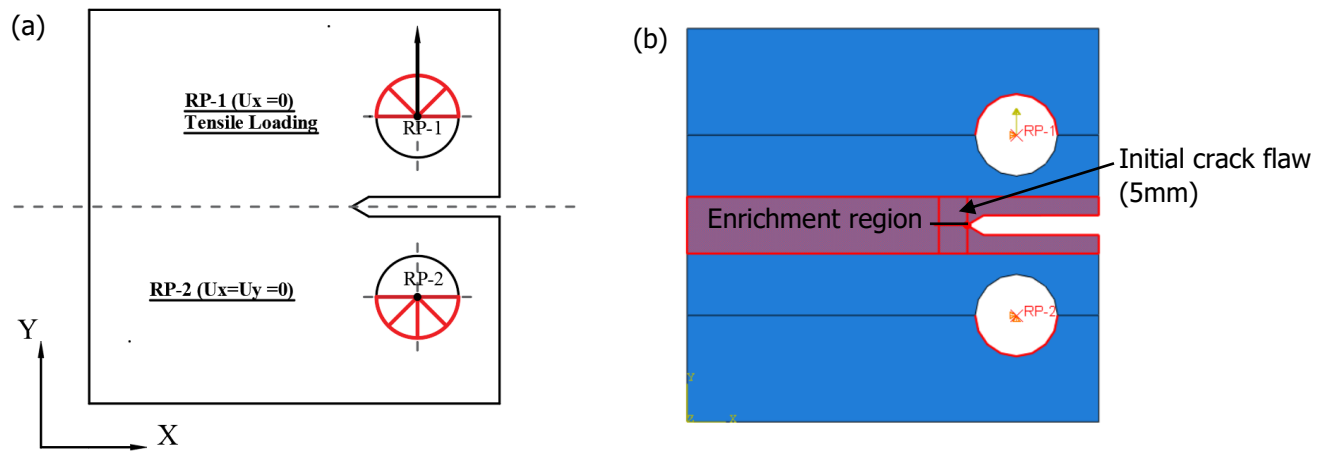
Figure 3.2 (a) Boundary condition of CT-Specimen (b) XFEM-model of CT-Specimen

In modelling relatively realistic boundary conditions of CT specimen, two reference points namely RP-1 and RP-2 were incorporated at the centre of the holes which were coupled (kinematically constraint in all the direction for translation and rotation) with the two-interior half holes of the CT specimen. The shell edge in 2D-XFEM model and the solid surface in 3D-XFEM model (see Figure 3.3). The boundary conditions were applied on these reference points as specified in Figure 3.2. RP-1 is translationally restrained in x-direction whereas RP-2 was restrained in both x- and y- direction. Moreover, the tensile cyclic load is applied at RP-1. Since XFEM simulation require a crack tip to be predefined. Therefore, a straight crack flaw of 5 mm length is assumed, and it is positioned at the notch of the model indicated in Figure 3.2 (b). Hence, the initial crack size was assumed to be of 15 mm. Crack domain represents the enrichment region contains a crack tip placed at the notch of the specimen illustrated in Figure 3.2 (b).
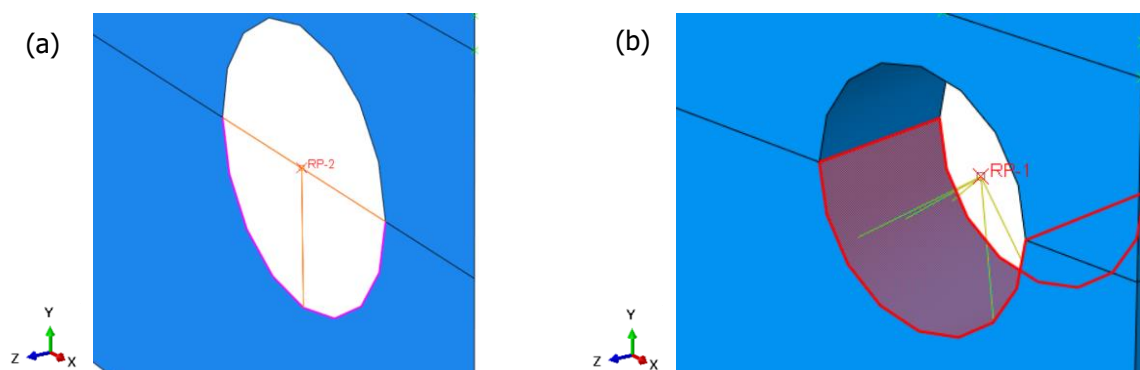
Figure 3.3 Illustration of reference -point coupled to a (a) Shell edge in 2D (b) Solid surface in 3D

3.2.3 Material property

The elastic material properties were assigned to the XFEM model as: Young's modulus $E=210500$ MPa and Poisson's ratio $\upsilon=0.3$. Furthermore, the fracture contact properties and Paris law constants are discussed in the following section.

LEFM implementation

Virtual Crack Closure Technique (VCCT) was used in the XFEM-based linear elastic fracture mechanics for crack propagation analysis using the direct cyclic approach with a time increment size of 0.05 per cycle. The direct cyclic load simulation is based on the periodic function (equation 2.12) and the parameter used for different stress ratios (Figure 3.4) are tabulated in Table 3.1.

Table 3.1 Direct cyclic parameters

R_σ	Load (N)	A_0	A_1	B_1	t_0	ω
0.0	6118.6	0.5	0	0.5	0	2π
0.25	7246.2	0.625	0	0.375	0	2π
0.50	9345.9	0.75	0	0.25	0	2π
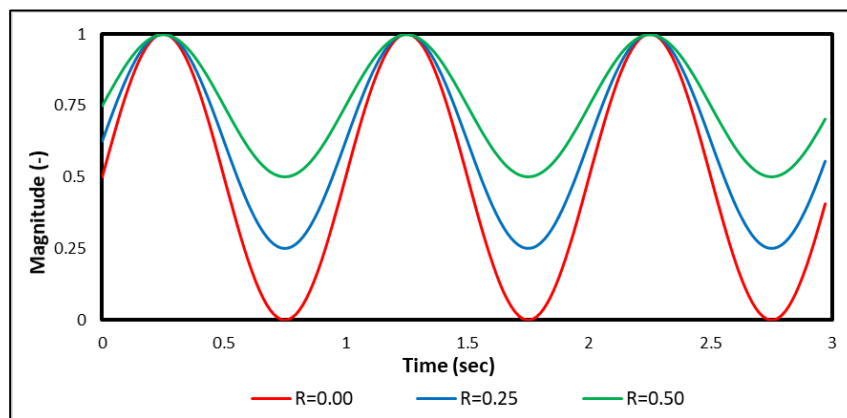
Figure 3.4 Graphical representation of different stress ratios

The direct cyclic approach is combined with the Paris law formulation to simulate the crack propagation. These fatigue crack growth rates are evaluated based on assigned VCCT parameters (Table 3.3). The crack propagation appears when the energy available for the crack is high enough to overcome the fracture resistance of the material. Since ABAQUS® analyses the fracture by the strain energy criterion approach, the Paris law parameters C_3 and C_4 were calculated assuming plane stress situation from equation (2.8) and (2.14) and are listed in Table 3.2 for several stress ratios. To ensure the start of crack growth process, material constants C_1 and C_2 were kept negligible as 0.001 and 0 respectively. Once the onset of the fatigue crack growth is satisfied (equation 2.13), the crack propagation rate can be computed based on the fracture energy release rate (equation 2.14).

Table 3.2 Constants of Paris' Law and XFEM Abaqus

R_σ	B (mm)	F_{max} (N)	F_{min} (N)	Experimental data		XFEM Abaqus	
				C^a	m	C_3	C_4
0.0	7.81	6118.6	61.8	2.5893E-15	3.5622	7.8419E-06	1.7811
0.25	7.47	7246.2	1811.5	2.5491E-15	3.7159	1.9790E-05	1.8579
0.50	7.41	9345.9	4672.9	8.2764E-16	3.8907	1.8768E-05	1.9453

In this study, Power law mix-mode model is selected for evaluating the equivalent fracture energy release rate represented in the equation (2.15) because of its simplicity in the relation of different modes of fracture.

The test results for the fracture toughness K_{IC} of the S355 steel grade obtained in the experiment [23] using circumferentially cracked round bars (CCRB) ranges from 35.78 MPa√m to 40.4 MPa√m. This scatter can be possibly used in Compact-Tension (CT) specimen, a single edge notched bend or three-point loaded bend specimen, which is standardized by a different institution. Therefore, this data was taken as the base of this study and applied to the XFEM-model tabulated in Table 3.3.

Table 3.3 Critical energy release rate G_c

XFEM model	Critical energy release rate Gc (Nmm^{-1})			Exponent		
	Mode I	Mode II	Mode III	α_m	α_n	α_o
CT- Specimen	6.5	6.5	6.5	1	1	1

3.2.4 Mesh quality

The 2D XFEM-model consisted of shell elements and was modelled using a 4-node plane stress quadrilateral with linear geometric order. The mesh size should be small to capture accurate stresses near the crack tip. However, a numerical model with fine mesh can be time-consuming, therefore a variable mesh was used. In the enrichment area (XFEM region) 0.5 mm mesh size was used and 2 mm in the non-enrichment area was used, as shown in Figure 3.5. On other hand, the 3D XFEM-model consisted of solid elements and was modelled using 8-node brick elements with linear geometric order. Similar to the shell model, a variable mesh was used but with 0.33 mm mesh size for the enrichment elements. All the meshing details are tabulated in Table 3.4.
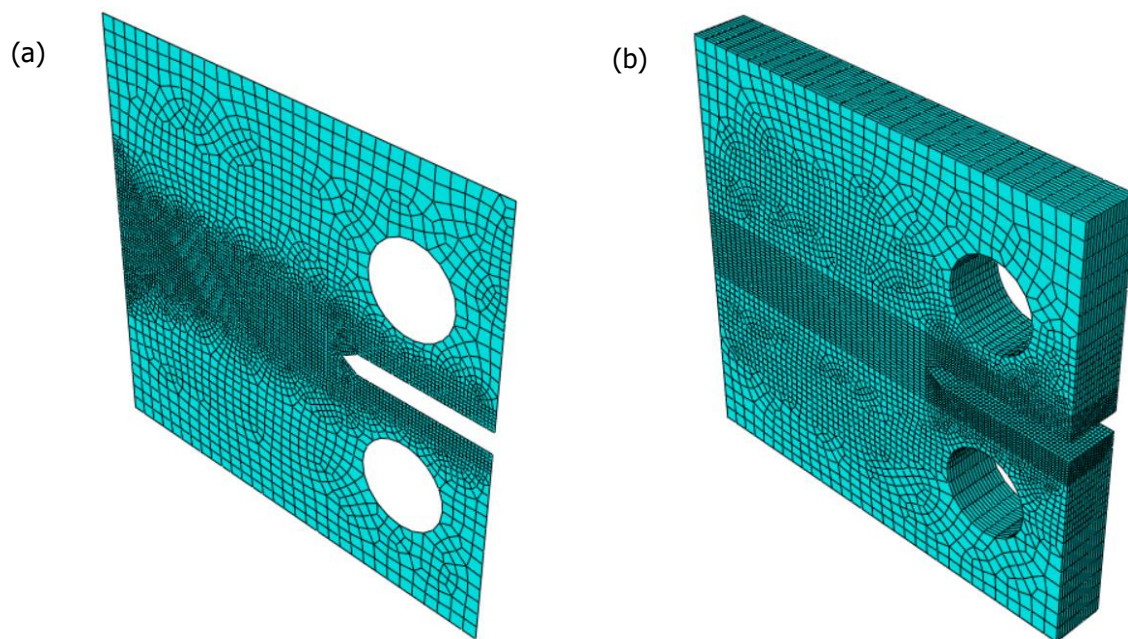
Figure 3.5 Mesh quality (a) Two-dimensional XFEM-model (b) Three-dimensional XFEM-model

Table 3.4 Meshing details of XFE model

Model	Region	Element type	Mesh size
2D-XFEM	Enriched shell	4-node plane stress quadrilateral (CPS4)	0.50 mm
2D-XFEM	Non- Enriched shell	4-node plane stress quadrilateral (CPS4)	2.00 mm
3D-XFEM	Enriched solids	8-noded linear brick (C3D8)	0.66 mm
3D-XFEM	Non-Enriched solids	8-noded linear brick with reduced integration (C3D8R)	2.00 mm

3.3 Output

An output result of crack propagation using direct cyclic loading is presented in this section. In the case of 2D-XFEM, it has been observed the crack propagated without changing the direction by fracturing the element (critical) at the end of the stabilised cycle ahead of the crack tip with zero stiffness. As the element (enriched) is cracked, the load is redistributed for the next cycle, and the stress intensity factor is captured based on fracture energy release. The fracture energy release rate was accounted for the enriched element ahead of the crack tip followed by the next enriched element when the previous enriched element is completely fractured. Simultaneously, the number of load cycles was precisely noted as the fatigue crack propagated over the element length. An example of the 2D-XFEM output is illustrated in Figure 3.6 representing the status of enriched element, the crack tip and crack surface from the crack tip opening as STATUSXFEM, PHILSM and PSILSM output variable respectively at 1.87×10^5 load cycles for zero stress ratio. In addition to that, different propagation stages are represented in Figure 3.7. In the case of 3D-XFEM, the mechanism is bit complex explained in section 3.4.3. An example of the 3D-XFEM output is presented in Figure 3.8 illustrating the crack shape and crack propagation mechanism along through-thickness direction at 2.15×10^4 load cycles for zero cycles.

3.3.1 2D-XFEM model
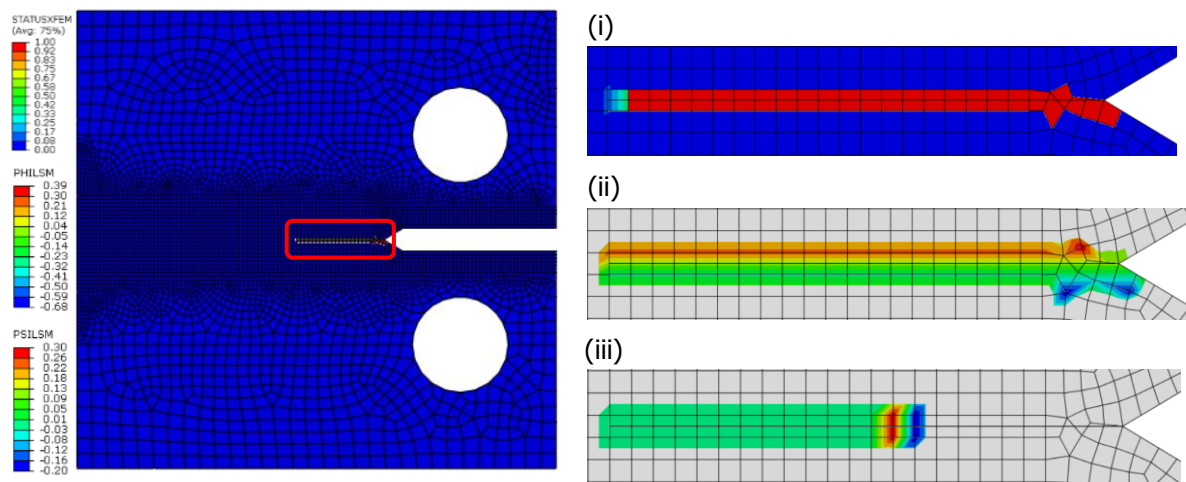
Figure 3.6 XFEM output (i) STATUSXFEM (ii) PHILSM variable output (iii) PSILSM variable output
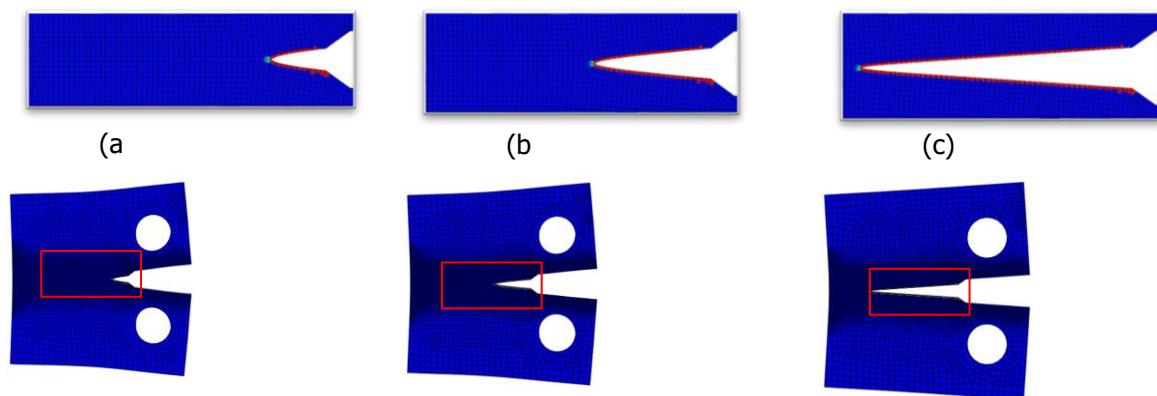
Figure 3.7 Representation of different crack propagation stages at (a) N= 1.23x10⁴ load cycles (b) N= 13.16x10⁴ load cycles (c) N= 24.42x10⁴ load cycles

3.3.2 3D-XFEM model
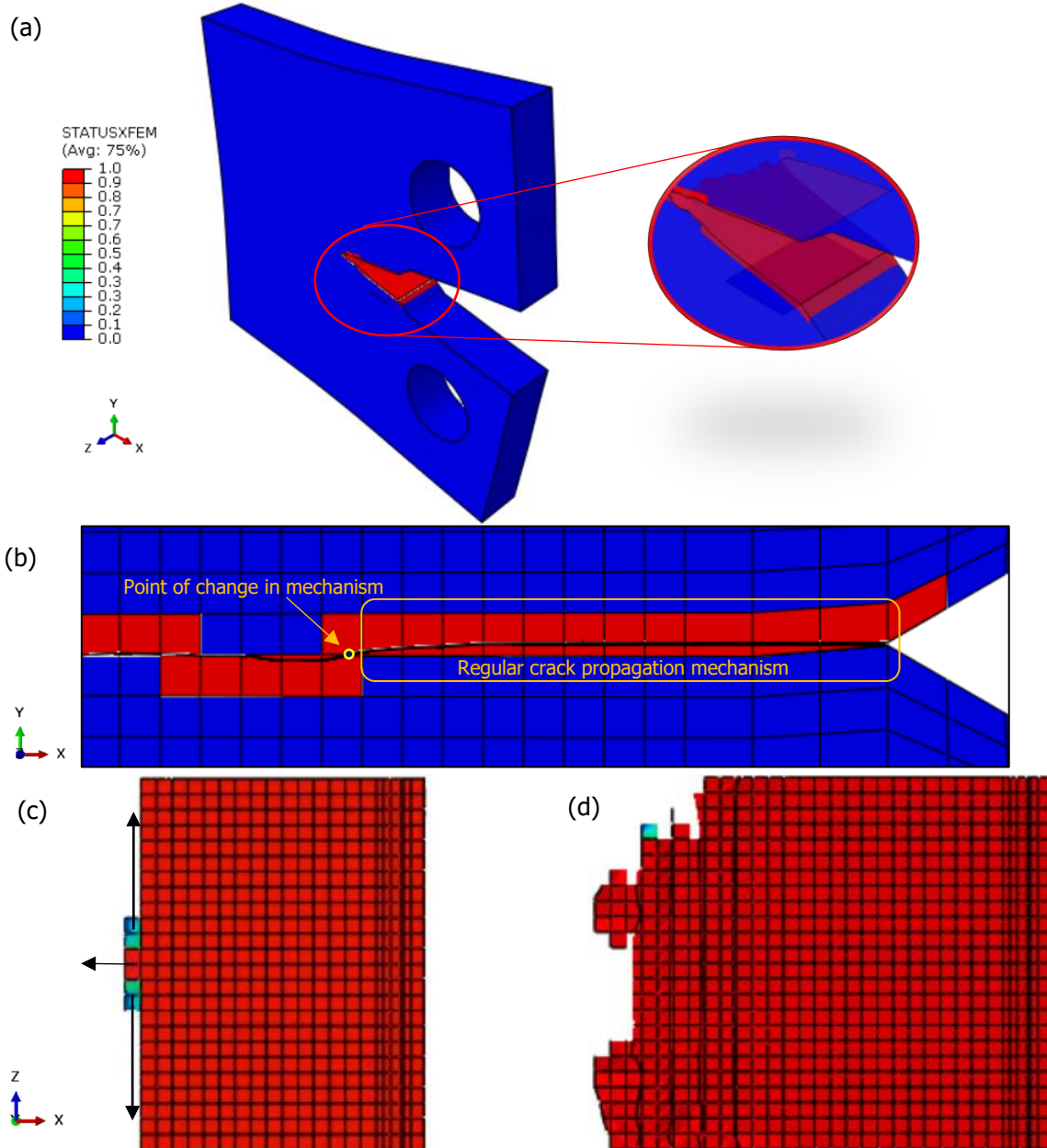
Figure 3.8 (a) 3D-Model STATUSXFEM output indicating the crack shape (b) Representation of crack propagation path and change in mechanism (c) Regular crack propagation mechanism (d) Irregular crack propagation mechanism

3.4 Result and Discussion

The results of the fatigue crack propagation obtained from numerical simulations are presented in this section. It should be noted that the stress intensity factor values were computed in the experiment using the formulation proposed in ASTM E647 for the CT specimens [21].

$$\Delta K = \frac{\Delta F}{B\sqrt{W}} \left(\frac{(2+\alpha)}{(1+\alpha)^{3/2}} \left(0.886 + 4.64\alpha - 13.32\alpha^2 + 14.72\alpha^3 - 5.6\alpha^4 \right) \right) \tag{3.6}$$

where $\alpha = a/W$, a is the crack size; B is the thickness of the specimen, W is the width of the specimen and ΔF is the applied load range. In automated crack simulation, the stress intensity factor range is computed based on fracture energy release rate. As the software (ABAQUS®) fails to compute K_{min} for corresponding applied F_{min} (cyclic load) load, the lower bound of SIF (K_{min}) was then calculated based on the following relation (equation 3.7).

$$R = \frac{K_{min}}{K_{max}} \tag{3.7}$$

3.4.1 2D shell XFEM-model

Figure 3.9 Fatigue crack propagation rates obtained from the numerical simulation (2D-XFEM) compared with the test results

In Figure 3.9, the numerical prediction of the fatigue crack growth rate *da/dN* is plotted as a function of the stress intensity factor range ΔK in a log-log graph. The stress intensity factor values are computed in numerical simulation using the fracture energy-based criterion and the crack propagation rate is evaluated as the crack propagated along the length of the element starting from 15 mm as the initial crack size as shown in the Figure 3.6.

After comparing with different stress ratios, it is observed that the rate of fatigue crack propagation is significantly increased as the stress ratio changes from 0 to higher positive values. This can be evaluated

comparing the slopes of the curve. For stress ratios R=0.0, R=0.25 and R=0.50, the slopes were 3.56, 3.71 and 3.89 respectively. The increase in crack propagation rate can be due to crack closure effects. Comparing with the test result, the simulated crack propagation provided good agreement with a maximum difference of 0.03% in the slope (m) and 1.48% in the intercept (C) of the power law equation.

3.4.2 Effect of stress ratio

Based on the above simulation for 2D-XFEM model, a fatigue crack growth is represented in a graph, with the crack size plotted as a function of number of load cycles for different level of stress amplitude (Figure 3.10 (a)). It is clear from the graph, the fatigue crack resulted in an exponential growth for all the stress ratios. However, the steepness of curve is significant as the stress ratio increase from zero to a positive value. With the decrease in the load range (ΔF) and corresponding increase to positive stress ratio (R), the cycles to failure is reduced drastically. It is to be noted that with a drop of 622.1 N in the force range (ΔF) from R=0.00 to R=0.25, the cycles to failure falls by 6 times. Moreover, the final crack size is diminished by 3.5 mm. However, the difference is more prominent, when the stress ratio R=0.25 is compared with R=0.50. With the decrease of load range ΔF of 761.7 N, the cycles to failure is decreased only by 4 times but the final crack length is diminished by 5 mm. This increase in the fatigue crack propagation rate can be explained by crack closure mechanism through similarity principle.
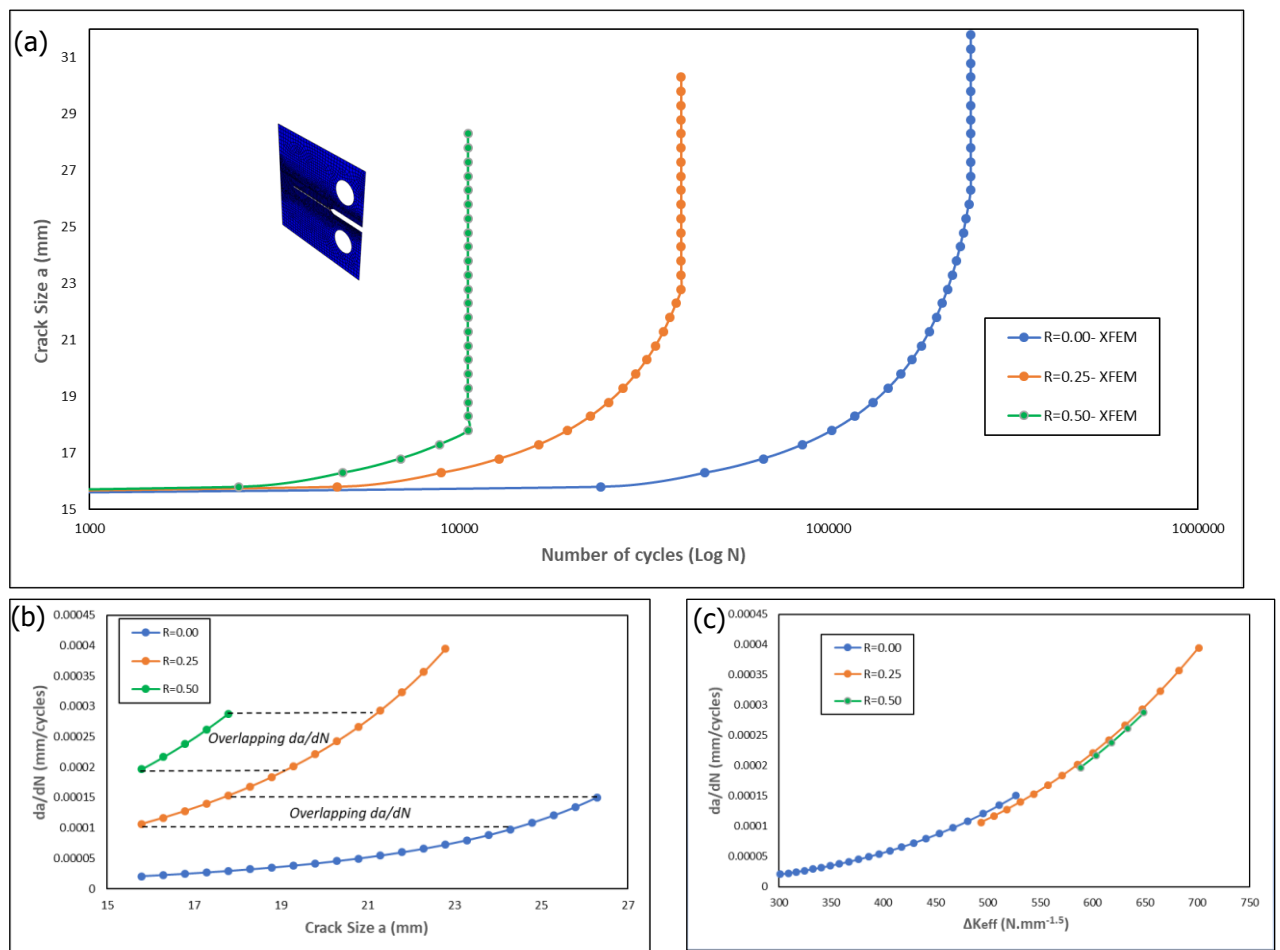
Figure 3.10 Fatigue crack growth for different stress ratios (b) Crack propagation rate (Similarity principle) (c) Effective stress intensity factor (Elber's crack closure mechanism)

According to similarity principle based on stress intensity factor, the extension of crack Δa is constant for constant ΔK cycles, which implies the crack growth rate is the function of K_{min} and K_{max} of the load cycles. In other words, the crack propagation rate is not only depending upon the stress intensity factor range ($\Delta K = K_{max} - K_{min}$) but also depends upon the stress ratio ($R = K_{min}/K_{max}$).

$$\frac{da}{dN} = f(\Delta K, R) \tag{3.8}$$

This effect can be observed with the simulated results, when the crack propagation rate is plotted against the crack size (Figure 3.10 (b)). The crack growth rates for different stress ratio R are partly overlapping, which indicates the similar crack growth rates occurs, although at different values of the crack size. This difference can be eliminated by taking in account the concept of crack closure.

The important aspect to be noted is that the stress singularity at the tip of the crack. The stress intensity factor is present as long as the crack tip is open, which can be termed as the effective stress intensity factor ΔK_{eff} (equation 3.8).

$$U = \frac{\Delta K_{eff}}{\Delta K} = \frac{K_{max} - K_{op}}{K_{max} - K_{min}} \tag{3.9}$$

Following the concept of Elber [24], the fatigue crack growth rate is defined (equation 3.10) and adapting the relation between the U and R which is valid for R-values in the range of -0.1 to 0.7 (equation 3.11):

$$\frac{da}{dN} = f(\Delta K_{eff}) \tag{3.10}$$

$$U = 0.5 + 0.4R \tag{3.11}$$

Using equation 3.9 and equation 3.11, the effective stress intensity factor is evaluated and plotted against the crack propagation rate for all the three stress ratios (Figure 3.10 (c)). The factor U is 0.5, 0.6 and 0.7 for stress ratios R=0.00, R=0.25 and R=0.50 respectively. The dependency of different crack size is eliminated by taking different stress ratio into account. Hence, the simulated results hold the crack closure mechanism and showed a good correlation with Elber's equation.

3.4.3 3D solid XFEM-model

Similar to 2D-XFEM model, a predefined straight crack front of 5 mm in 3D-XFEM model is assumed and positioned in the mesh in the middle of the crack element ensuring similar crack propagation path. When the crack simulation is performed, the crack propagates perpendicular to the load applied by fracturing the element from the middle of the element. Moreover, a regular crack propagation mechanism in through-thickness direction is observed. However, after a certain crack length, the crack propagation direction changes and intersect the boundary of the elements (see Figure 3.8 (b)). When the crack front encounters the top interface of the elements, the crack starts to propagate in an irregular fashion in through-thickness direction due to which the crack size calculation becomes more complex (see Figure 3.8 (d)). As a result, the crack growth is evaluated until the point of change in mechanism for several stress ratios. The change in direction of crack propagation is due to the imperfection in the method of applying boundary conditions. The reference point coupled to the surface of the hole generate an additional rotation due to eccentricity leading to the change in direction of propagation. Moreover, a non-uniform stress distribution is observed over the thickness of the respective holes. An example of principal stress distribution is presented in Figure 3.11 at crack size 15.1 mm.
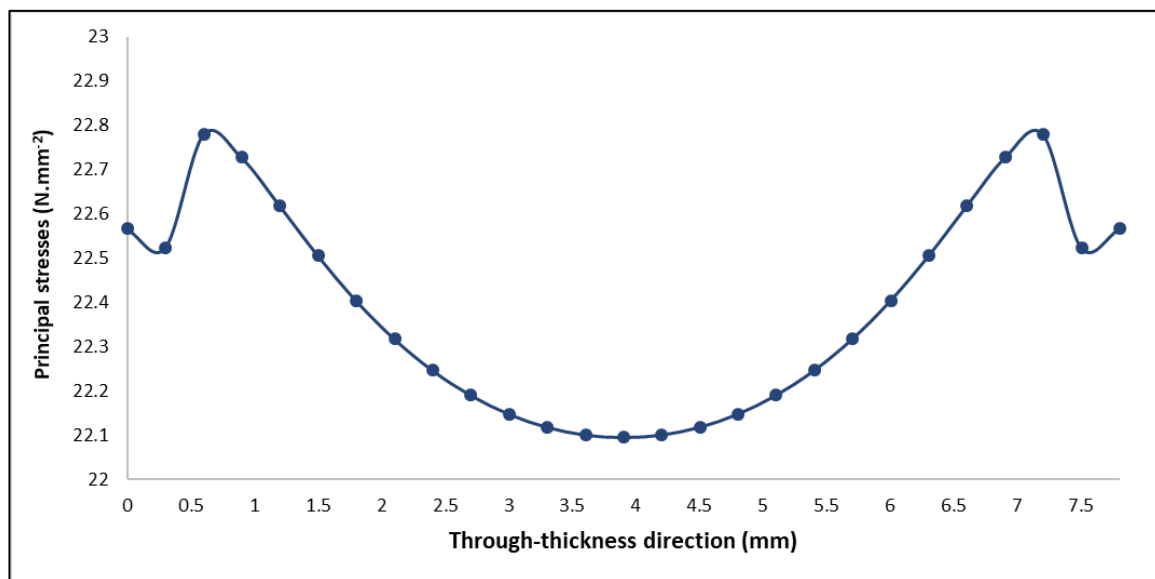
Figure 3.11 Non-uniform stress distribution over the thickness at holes

Comparison of fatigue crack growth

The results of 3D-XFEM for different crack size until the point of change in mechanism and corresponding number of cycles is plotted against each other and compared with the results of 2D-XFEM in Figure 3.12.
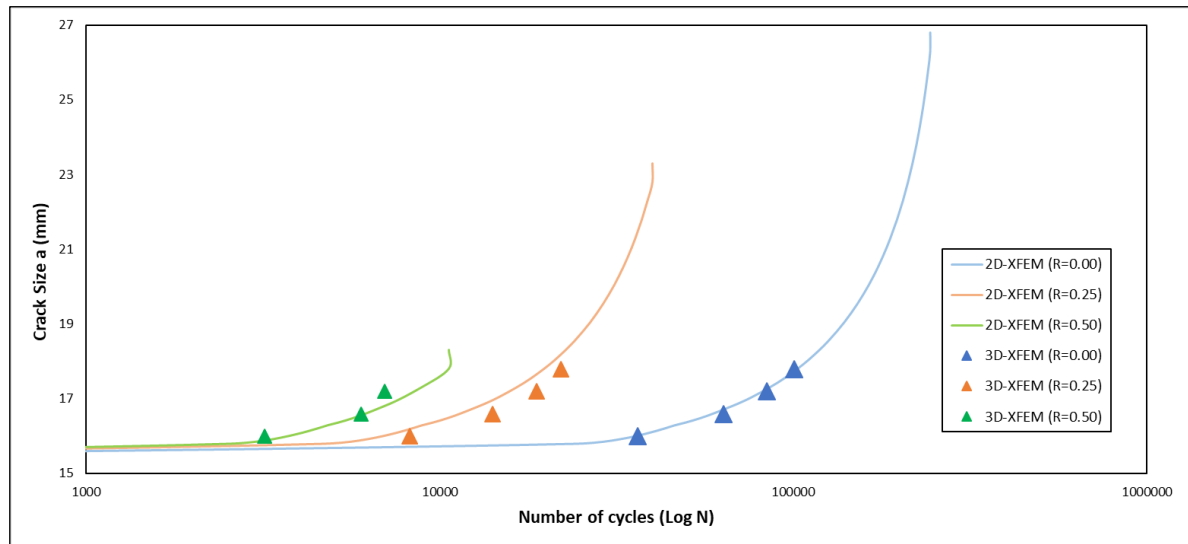
Figure 3.12 Comparison of fatigue crack growth between 2D-XFEM model and 3D-XFEM model

It was found that the simulated results of 3D-XFEM model is well correlated with the results of 2D-XFEM model up to a crack size of 17.8 mm. Although a small difference, both the models showed a similar crack growth. The difference between the models is higher, as the stress ratio increases from zero to a positive value. For stress ratio R=0.00, R=0.25 and R=0.50, the difference in load cycles goes up to 2.1%, 11.9% and 13.8% respectively. This is mainly due to crack propagation mechanism in through-thickness direction which is governed by non-uniform stress intensity factor distribution along the crack front.

Fatigue crack mechanism- 3D XFEM

The determination of stress intensity factor in 3D-XFEM model is more complex mainly due to its through-thickness effect. It is observed that the crack propagation starts from the centre of the thickness and propagates towards the edge of thickness for every crack length increment (mesh size of 0.3 mm) in the longitudinal direction (see Figure 3.8(c)). This crack mechanism holds for different mesh sizes up to 1 mm and is mainly due to the distribution of stress intensity factor along the crack front (see Figure 3.13). However, it is to be noted that the mechanism is depended on Paris law constant, which defines the rate of crack propagation. Figure 3.13 illustrates the stress intensity factor distribution in through-thickness direction along the crack front for different mesh sizes. This implies that the direction of crack propagation derives from the stress intensity factor distribution.
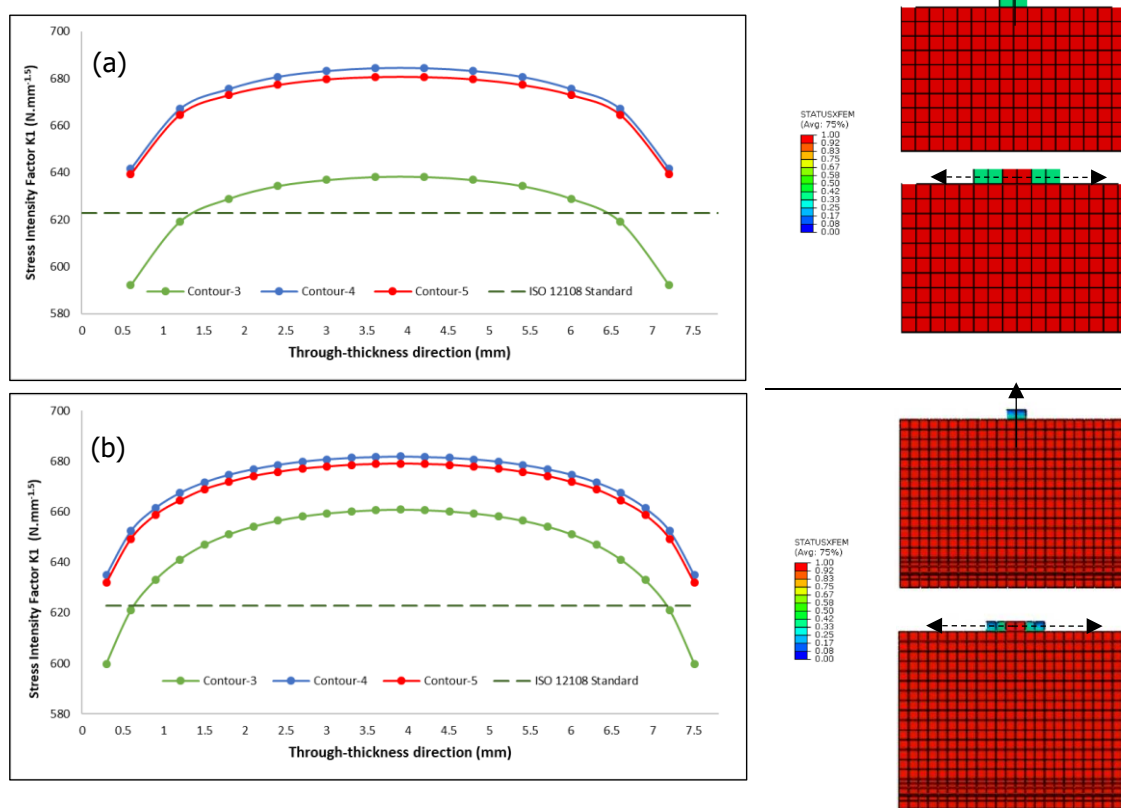
Figure 3.13 Stress Intensity factor distribution along the crack front in through-thickness direction compared to ISO 12108 standard for mesh size and crack propagation mechanism (STATUSXFEM output) (a) 0.6 mm (b) 0.3 mm

The through-thickness effect can also be explained by the crack closure mechanism. At the material surface, a greater crack closure mechanism is experienced due to which the crack opens first in the centre of the thickness followed by either side at the material surface. As a result, the crack front lag where the crack interests the surface leading to a curved crack front.

However, this crack growth mechanism does not provide a clear indication to compute the stress intensity factor. Therefore, in order to find a reliable way to determine the stress intensity factor an investigation is performed with different techniques available in ABAQUS® using 2D model and 3D model illustrated in section 3.4.4.

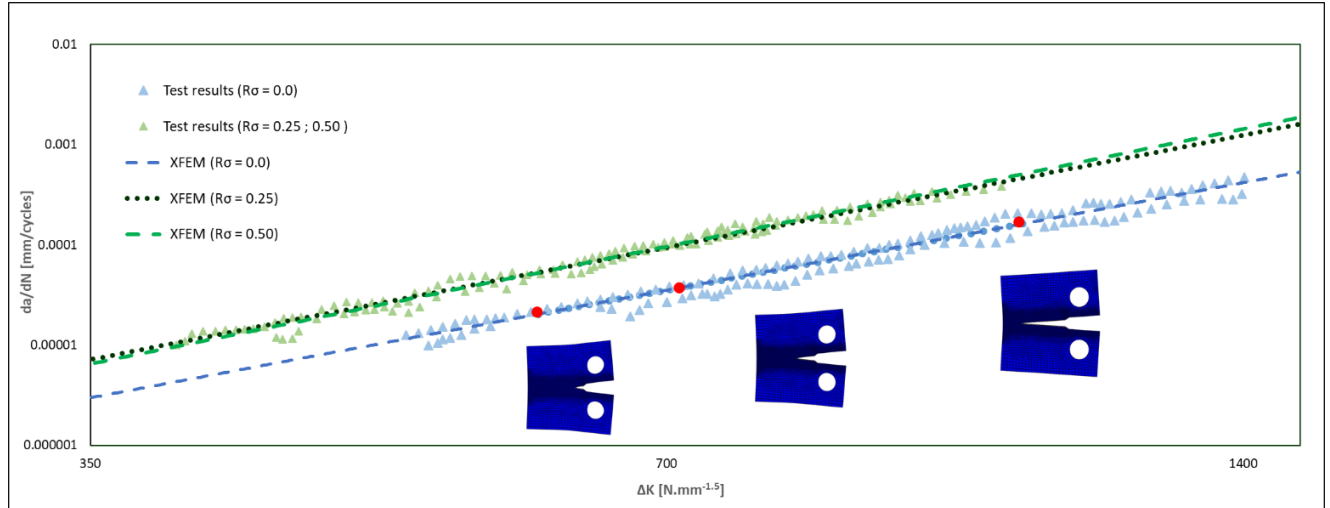## Fatigue crack propagation- 3D solid XFEM
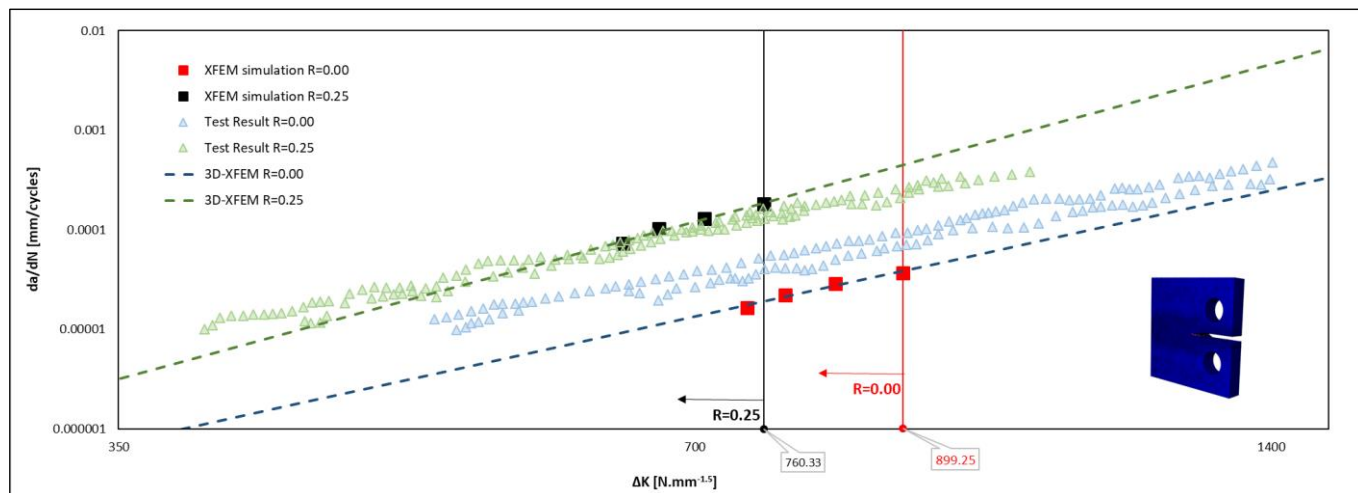
Figure 3.14 Fatigue crack propagation rates obtained from the numerical simulation (3D-XFEM) compared with the test results

In Figure 3.14, the numerical prediction of the fatigue crack growth rate *da/dN* is plotted as a function of the stress intensity factor range ∆K in a log-log graph. The stress intensity factor values are computed in numerical simulation using the fracture energy-based criterion from the edge (surface) element and the crack propagation rate is evaluated as the crack propagated along the length of the element starting from 15 mm as the initial crack size up to 17.8 mm where the regular crack propagation is valid.

It is observed that the rate of fatigue crack propagation is significantly increased as the stress ratio changes from 0 to a higher positive value. This can be evaluated comparing the slopes of the curve. The slopes for stress ratio R=0.00 and R=0.25 were 4.22 and 4.65 respectively for a crack length of 17.8 mm, which sets the boundary of the model as indicated in Figure 3.14. The increase can be explained through the crack closure effect. Furthermore, comparing the slopes with the test result, the simulated crack propagation provided a rough correlation with a maximum difference of 25.23 % in the slope (m) of the power law equation. The difference in the slope can be explained by the assumed crack flaw. A straight crack flaw resulted in variation of stress intensity factor along the crack front. Moreover, the effect the boundary conditions becomes predominant as the crack propagates over the length. Nevertheless, for comparison there is clear requirement of more evidence (value) as the crack only propagated in a regular fashion until the crack size 17.8 mm before changing the direction. Nevertheless, the range of applicability of 3D-XFEM model developed in this research is indicated in the figure as red and black for stress ratio R=0.0 and R=0.25 respectively. Therefore, a further investigation is recommended mainly to access the through-thickness effect and implementation of boundary conditions in the numerical model.

3.4.4 Stress Intensity Factor

ABAQUS® provide different techniques to capture the stress intensity factor around the crack tip. However, the investigation is limited to three techniques which will be performed using 2D-shell XFEM and 3D-solids XFEM. To evaluate the accuracy, the simulated results of all the techniques are compared with the stress intensity factor range formulation by ISO 12108 standard (equation 3.6).

Energy based -2D XFEM

Firstly, the automated simulated results of 2D-shell XFEM model (section 3.3.1) is taken as one the techniques to compute SIF which is evaluated based on fracture energy criterion is plotted against different crack sizes in Figure 3.16.

Contour Integral -2D

Beside automated XFEM crack simulation, it is also possible to determine the stress intensity factor range using stationary crack analysis. One of the most significant aspect of stationary crack analysis is contour integral calculation as it gives the measure to access critical crack size. Thereby, a stationary crack simulation is performed using 2D-shell model to determine the SIF values based on contour integral calculation. This 2D-FE model is similar to the previous 2D-XFEM model. Only, the mesh is modified with five concentric contour rings at the crack tip as illustrated in Figure 3.15. The size of the total contour domain is determined by the number of element rings which are included in the calculation of the integral. Theoretically, this calculation is independent of the size of the contour domain. However, the computed SIF varied for different element rings. This can be due to the approximation with the finite element solution. It was observed that the SIF values were converging as the domain is increased. Thereby, the SIF was calculated by taking the average value of last three contours.
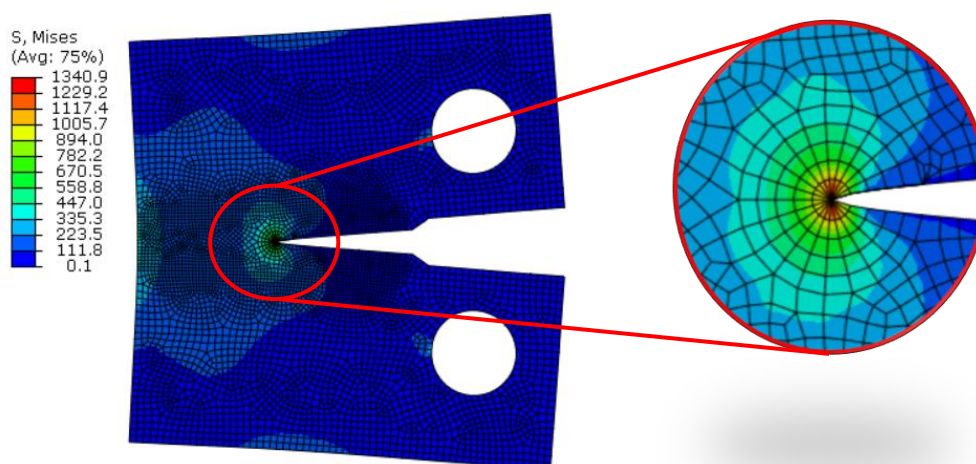
Figure 3.15 2D-shell FE model for contour integral calculation

XFEM- Stationary crack analysis

Similar to the contour integral method, it is also possible to compute the SIF value using 3D-XFEM stationary crack analysis. However, the only difference is the way of computation. XFEM stationary analysis requires the user to specify the enrichment radius, which by default is three-times the element characteristic size. It should be noted that the crack tip should be surrounded by a sufficient number of elements to obtain path independent contours. Using the default setting, SIF values are computed along the crack front for a finite number of positions. These points are chosen automatically by the software where the crack front intersects the element boundaries. This way the stationary crack simulation is performed by inserting crack of different sizes. An example of SIF values along the crack front is illustrated in Figure 3.13 for a crack size of 26.5mm. It is observed that the SIF values is not constant along the crack front, therefore two extreme values (minimum: at the edges and maximum: at the centre) were taken into consideration and plotted against the crack size as shown in Figure 3.16. Thus, providing a bandwidth (range) of SIF value.
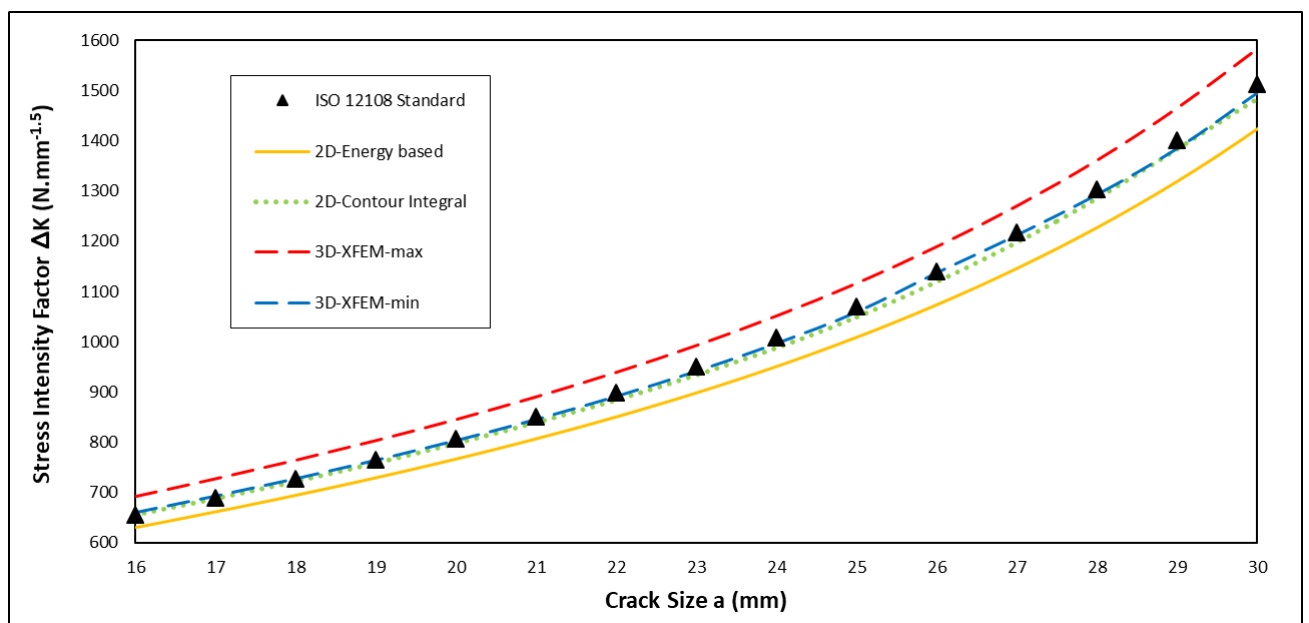
Figure 3.16 Stress intensity values for various crack size using different approaches

Figure 3.16 represents the variation of stress intensity factor value when plotted against different crack sizes using different techniques. Although difference in magnitude, the SIF obtained from different technique showed similar trend when compared to ISO 12108 standard. The difference increases as the crack size increase. This is because the crack size approaches towards the critical crack size a_c. Moreover, it is observed that 2D-energy based is underestimated throughout with a maximum variation of 5.81% compared to ISO 12018 standard. Furthermore, contour integral technique showed its reliability throughout with a maximum difference of 1.92%. However, in the case 3D-XFEM, the variation itself is quite significant between the max. SIF and min. SIF. Although XFEM-max showed an overestimation of SIF, XFEM-min showed its promising sign of being reliable with a maximum difference of 1.16%. Thus, in case of 3D-XFEM, XFEM-min (at the edges) can be the reliable technique in predicting SIF.

3.4.5 Effect of LEFM parameters (2D-XFEM)

One of the major complexities of XFEM is that there are too many constants required to set-up a problem. Since XFEM calculation is highly sensitive to LEFM parameters, it is important to study the effect on the crack propagation. Therefore, an investigation is performed using different parameters. For simplicity the simulation is carried out in 2D shell XFEM model and is limited to mode-I fracture (K_I) using power law mix-mode behaviour for zero stress ratio ($R_\sigma=0$). Firstly, the dependency of mesh on crack propagation rate and corresponding stress intensity factor range. Secondly, two parameters η_1, η_2 used in defining the boundaries of Paris law regime. Lastly, the parameters G_{IC} , a_m used in power law mix-mode behaviour to compute the equivalent strain energy release rate.

Mesh dependency

Table 3.5 Representation of modelling detail and computational time

Mesh size (mm)	Nodes	Elements	CPU time (sec)
1.00	2949	2222	157.1
0.50	7064	4778	215.9
0.25	22477	14106	1318.9
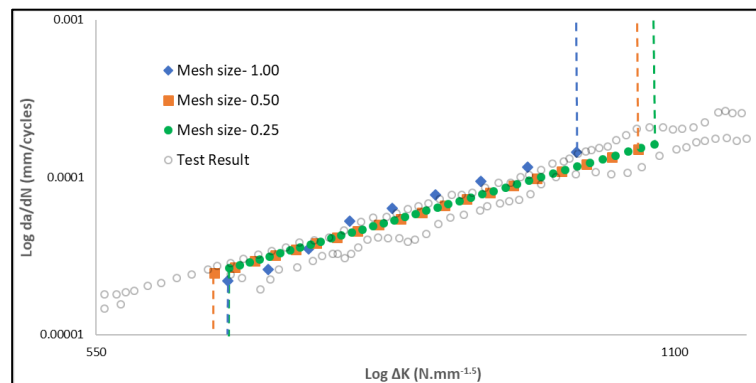
Figure 3.17 Fatigue crack propagation rates obtained from the numerical simulation for different mesh sizes

A finer mesh will certainly help in capturing the singularity around the crack tip simultaneously demanding high computational power. Therefore, it is important to find an equilibrium between the accuracy of result and the computational effort.

An initial crack size of 16.8 mm is kept constant and an automated crack simulation is performed for different mesh sizes to compute the stress intensity factor range and crack propagation rate. It was observed that the final crack size varied significantly especially for 1 mm mesh size. The final crack size for mesh size 1 mm, 0.5 mm and 0.25 mm were 25.8 mm, 26.8 mm and 26.5 mm respectively. As a result, the unstable crack asymptote varied noticeably. The inconsistency is observed mainly for 1 mm mesh size. Taking the computational time and accuracy of results into consideration, it is recommended to use 0.5 mm mesh size to adequately simulate crack propagation.

Table 3.6 Illustration of output results obtained from different mesh size

Mesh Size [mm]	K$_{threshold}$ [N.mm$^{-1.5}$]	K$_c$ [N.mm$^{-1.5}$]	N$_{initial}$ [cycles]	N$_{final}$ [cycles]	Crack size [mm]	
					Initial	Final
1.00	643.786	1040.67	45641.3	240179	16.80	25.80
0.50	633.647	1087.79	66661.0	243414	16.80	26.80
0.25	645.311	1091.49	75698.3	244154	16.75	26.50

Paris Law regime

$$\eta_1 = \frac{G_{thresh}}{G_c} \quad \text{and} \quad \eta_2 = \frac{G_{pl}}{G_c}$$

The crack simulation is performed keeping constant G_c = 6.50 N/mm and correspondingly varying η_1 and η_2. The G_{thresh} depends on various factors, one of which is elastic modulus E. When E=210500 MPa was assigned, the strain energy released to fracture the first element was found out to be 1.729 N/mm, which implies that the η_1 ratio should be lower than 0.266 to initiate the crack propagation. Many researchers have suggested a threshold value (see Figure 5.7) based on their investigation. If the threshold value (K_{thresh}) and the fracture toughness value (K_{IC}) are known, η_1 ratio can be determined.
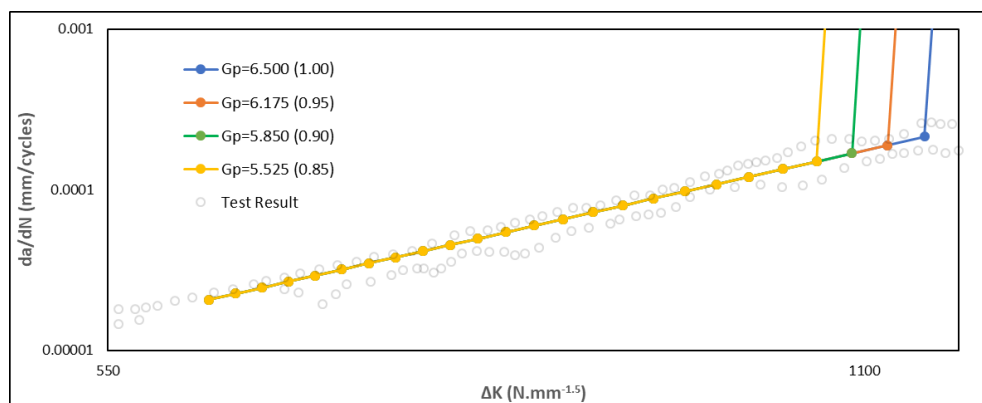
Figure 3.18 Fatigue crack propagation rates obtained from the numerical simulation for different Gpl ratios

On the other side, four different η_2 ratios were used ranging from 1.00 to 0.85. It was observed that the final strain energy release (N/mm) before entering unstable crack propagation region comes out to be 6.42, 6.00, 5.62 and 5.27 which is lower than 6.50, 6.175, 5.85 and 5.525 for η_2 ratio 1.00, 0.95, 0.90 and 0.85 respectively. This illustrates the usage of η_2 ratio which can be assigned as the fracture toughness of the specimen ensuring unstable crack propagation beyond the limit.

Power law equation

$$\frac{G_{equiv}}{G_{equivC}} = \left(\frac{G_I}{G_{IC}}\right)^{a_m} \rightarrow \quad G_{IC} \ \text{and} \ a_m$$

The crack simulation is performed keeping constant η_1 ratio = 0, η_2 ratio = 0.85 and varying two parameters critical strain energy release G_{IC} and exponent a_m. These two parameters are used to calculate the equivalent fracture energy release rate.
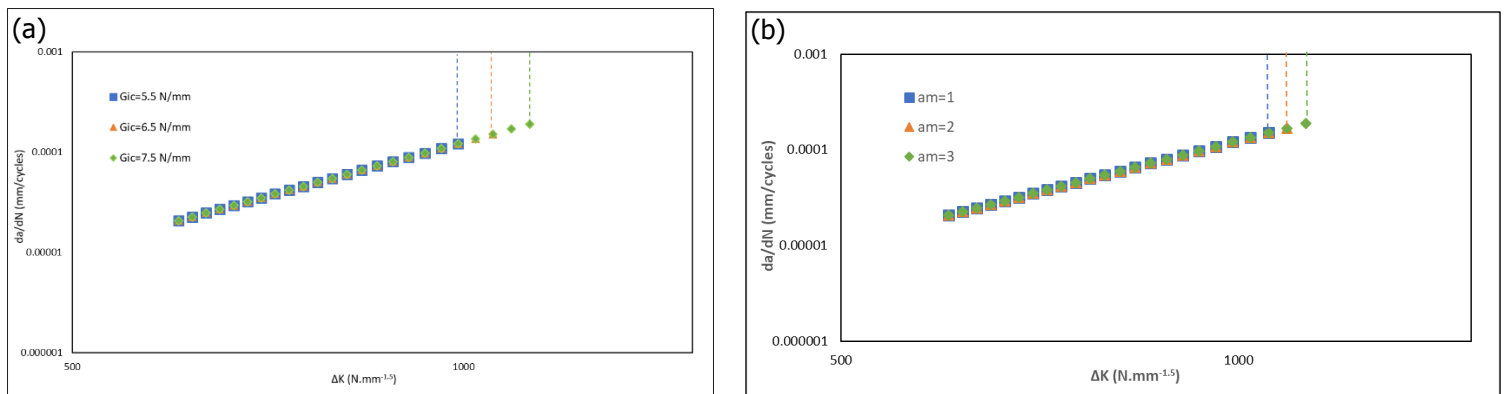
Figure 3.19 Fatigue crack propagation rates obtained from the numerical simulation for different (a) G_{Ic} (b) a_m

Table 3.7 Representation of fracture toughness and final crack size for different G_{Ic} values

G_{IC} [N.mm^{-1}]	Final crack size [mm]	Final Strain energy release [N.mm^{-1}]	Fracture toughness [N.mm$^{-1.5}$]
5.5	25.8	4.65	990.20
6.5	26.8	5.27	1053.45
7.5	27.8	6.00	1124.15

Figure 3.19(a) depicts the range in crack propagation by varying G_{IC}. It is observed as the crack propagation progresses the SIF range increase with increase in crack size. This parameter helps to define the fracture toughness of the material ensuring unstable crack propagation beyond the limit. Furthermore, the final failure crack size is changed correspondingly. Table 3.7 illustrates the fracture toughness (plane stress situation) and respective final failure crack size.

Table 3.8 Representation of fracture toughness and final crack size for different a_m values

a_m exponent	Final crack size [mm]	Final Strain energy release [N.mm^{-1}]	Fracture toughness [N.mm$^{-1.5}$]
1	26.8	5.62	1087.79
2	27.3	6.00	1124.15
3	27.8	6.42	1162.68

Figure 3.19(b) illustrates the range in crack propagation when a_m exponent is varied for constant G_{IC} 6.5 N/mm. The a_m exponent has a significant influence in computing G$_{equivC}$. As a result, final crack size is varied by 0.5 mm for every increase in the exponent. Table 3.8 illustrates the fracture toughness (plane stress situation) and respective final failure crack size.

With mesh size 0.5 mm, the difference is realised. Moreover, it is recommended to use finer mesh to precisely evaluate the above effect. Nevertheless, this investigation performed on various LEFM parameters allowed to explore the capabilities and understand the limitations of XFEM.

Chapter 4

ORTHOTROPIC STEEL DECK (OSD) SPECIMEN

4.1 General

Orthotropic Steel Decks (OSDs) are widely used in various types of steel bridges due to its benefits of light weight, high load bearing capacity and speedy construction. Over the past decades, many improvements have been achieved in various aspects of design, manufacturing, inspection and maintenance. Thereby, the structural behaviour of such bridge decks has been significantly enhanced. However, fatigue still remains its predominant problem. This is mainly due to numerous welding operations and its complexity involved in OSD. As a result, such bridge decks suffer from many sensitive crack locations. Moreover, various fatigue cracks were detected in recently built OSD [3], which proves the lack of understanding of the fatigue behaviour. Therefore, many researchers [2] have tried to investigate the fatigue behaviour of OSD through experiments. However, performing only experiments may not be a cost-effective solution. Therefore, it is necessary to combine the experimental data with numerical approaches and preferably assuming basic material properties to predict behaviour of critical detail.

Numerical model based on fracture mechanics approach can be used to analyse fatigue crack propagation and has already shown its reliability. Particularly, the use of LEFM models have several advantages as it significantly reduces the requirement of experiments. Commercial software such as ABAQUS® incorporates XFEM techniques to model discontinuities as an enriched feature. Using XFEM, it is possible to simulate automated crack propagation by inserting the crack into the model.

The main objective of this chapter is to predict the fatigue crack growth in OSD using XFEM-model. The set of analyses aims to simulate in an adequate manner according to the experiment [25]. Prior to automated XFEM simulation, a set of FE analyses are performed to validate the numerical model as per the test setup by evaluating the vertical deformation, longitudinal strain distribution and hotspot stress based on static cyclic loading sequence. Moreover, the simulated results will be correlated with the beach marks measurement derived from the fatigue experiment to determine the Paris law constants C and m.

4.2 Numerical simulation of fatigue- FEM

4.2.1 Experimental setup [25]

Wim Nagy [25] described a series of a fatigue test on orthotropic steel deck focusing on stiffener-to-deck plate detail. The main aim of his experiment was to adequately represent existing OSDs through a small specimen with possible realistic boundary conditions. As a result, the following geometry and boundary conditions were adopted illustrated in Figure 4.1
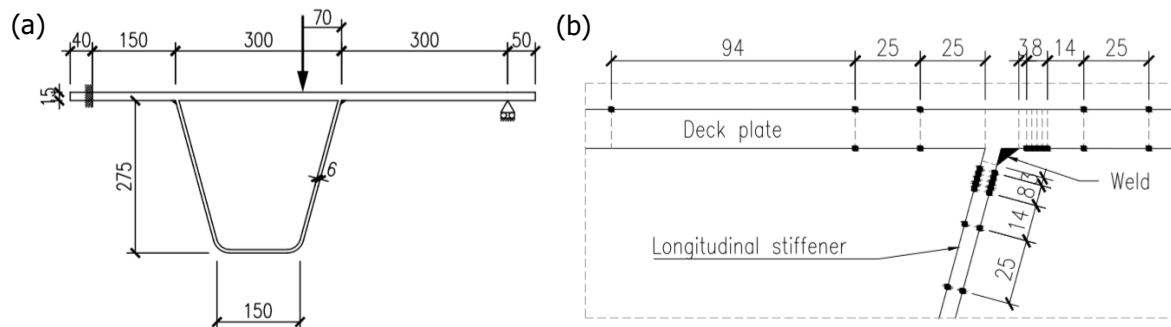
Figure 4.1 (a) Dimension of the OSD specimen [25] (b) Strain gauge location at the stiffener-to-deck plate connection [25]

The test specimen consists of one closed stiffener and a deck plate extended to the right by 300 mm and to the left by 150 mm. A closed stiffener of 275 mm high and 6 mm thick is welded to a 15 mm deck plate. The upper width of the closed stiffener is 300 mm while the lower soffit is 150 mm with 24 mm of radius. The deck plate is further extended to 40 mm and 50 mm from the left and right support respectively. The left support is fixed whereas the right support is roller (pinned). The load is situated at 70 mm from the right welded connection between the deck plate and the stiffeners.

Figure 4.1(b) describes the strain gauge pattern used in the fatigue test. Since the hot-spot stresses are computed from the linear extrapolation from the stress measured at a distance of 25 mm and 50 mm from the stress location, the strain gauges were placed at that location on either side of the corresponding plates.

Figure 4.2 illustrates the loading and support conditions in detail. The left support consists of fixed bolted connection whereas the right support is a free roller bearing with rectangular steel bars of 60 mm high and 40 mm wide. For loading, hydraulic jack system INOVA actuator AH200-200 is used.
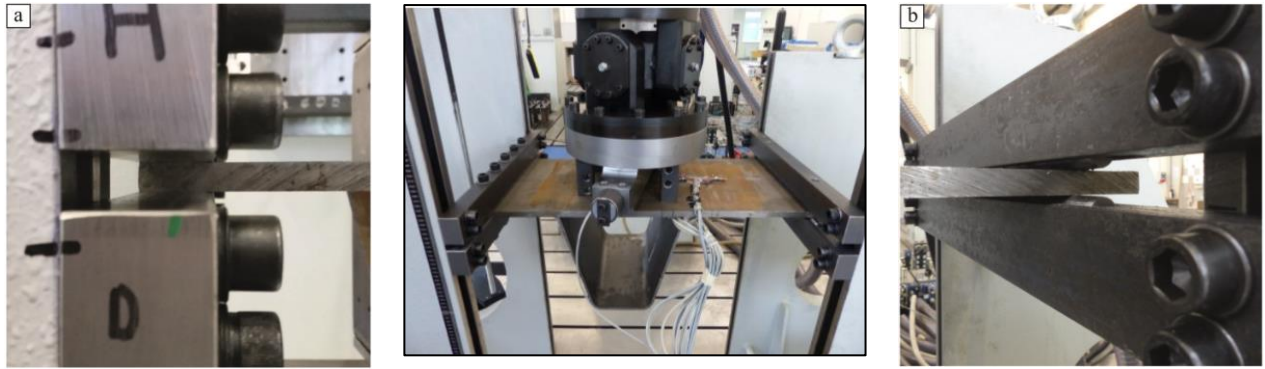
Figure 4.2 Detail of the loading and support conditions [25]

The cyclic loading sequence used in the static load test was different from the loading sequence used in the fatigue load test. In case of static load test, the load is gradually varied from 40KN to -40KN with an increment of 10KN held for 10 seconds before the next increment. However, a periodic cyclic loading sequence was used in fatigue test which varied from 0KN to -31KN with frequency $f = 1\,Hz$. A negative load corresponds in pushing the hydraulic jack system or a tensile load cycle at the weld toe.

4.2.2 Development of FE model

Geometry

A full-scale FE model is built based on the dimensions and boundary conditions specified in Figure 4.1(a) for a length of 400 mm. FEM calculations can sometime be time-consuming and can utilize a huge amount of computational power for a large model, the FE model was simplified. The OSD specimen model was developed in a combination of shell and solid elements. The solid elements were used in the welded connection between the deck plate and the stiffener where the crack investigation has to be carried out and the shell element were used in the remaining part. To ensure a rigid connection between these two parts, the edge surface of the shell was constrained to face region of the solid using shell-to-solid coupling. Since it is not possible to incorporate line-load in three-dimensional geometry in Abaqus®, a reference point (RP-1) was incorporated which is kinematically coupled in all the directions to a straight line on the surface and cyclic load is applied on it.

■ Shell part   ■ Solid part
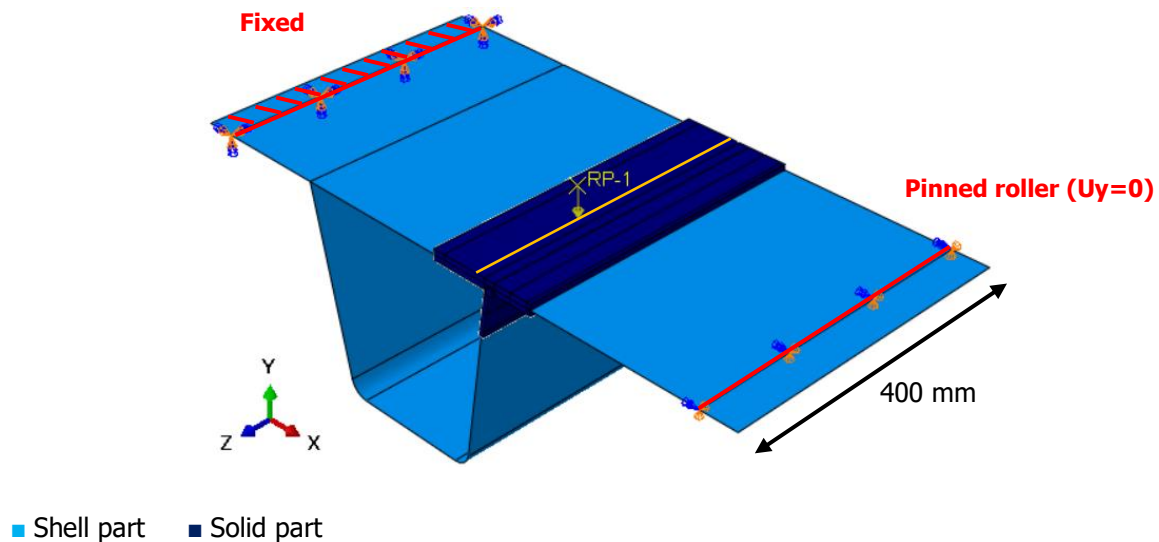
Figure 4.3 FE model: Interactions and boundary conditions

The displacement and rotation of the left support are restrained in all the three orthogonal x-, y- and z-direction. Whereas, the displacement is fixed in y- and z-direction allowing rotation in all the directions. In both cases, these conditions are applied to the edges of the top and bottom surface (Figure 4.3).

Material property

The elastic material properties were assigned to the FEM model as: Young's modulus E=210000 MPa and Poisson's ratio υ=0.3. Furthermore, the fracture contact properties and Paris law formulation will be discussed under LEFM implementation (section 4.4.2).

Mesh

3D tetrahedron elements are easily applicable to almost every structure and can be an ideal choice for complex structures. One of the major disadvantages of using tetrahedron elements is the locking problem. In fact, in case of bending, the shear should be zero or negligible but the inconsistent terms in the interpolation functions of linear elements make the shear strain much different from zero. Thereby, the non-zero artificial shear strains absorb more energy leading to a stiffer element consequently. To alleviate the shear locking issue standard high-order (for instance quadratic) elements can be used. Therefore, the solid part (enrichment region) was modelled using a 10-node tetrahedron (C3D10) with quadratic geometrical order of mesh size 2.5 mm. A numerical model with finer mesh can be time-consuming, therefore a variable mesh is used for non-enrichment region. Solid part (non-enrichment) was modelled using an 8-node linear brick with reduced integration (C3D8R) of average mesh size 5 mm whereas a 4-noded shell element of 10 mm mesh size is adapted in the shell part (Part-3). Meanwhile, the incompatibility mesh (interfaces between a tetrahedron and hexahedral) was automatically generated using tie-constraints.
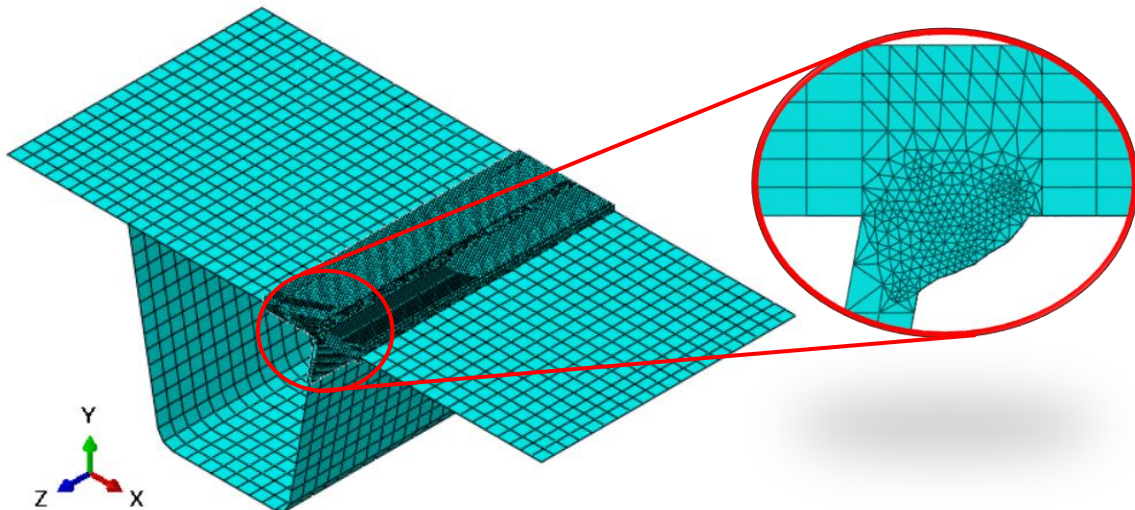
Figure 4.4 XFEM-model: Mesh quality

There are three types of element adapted in meshing the XFE model depending upon the shape and function in different regions is summarised in Table 4.1.

Table 4.1 Meshing details of XFE model

Part	Region	Element type	Mesh size
Part-1	Enriched solid	10-node quadratic tetrahedron (C3D10)	1.00 mm
Part-2	Non-enriched solid	8-node linear brick with reduced integration (C3D8R)	5.00 mm
Part-3	Non-enriched shell	4-node shell with reduced integration (S4R)	10.0 mm

4.3 Output
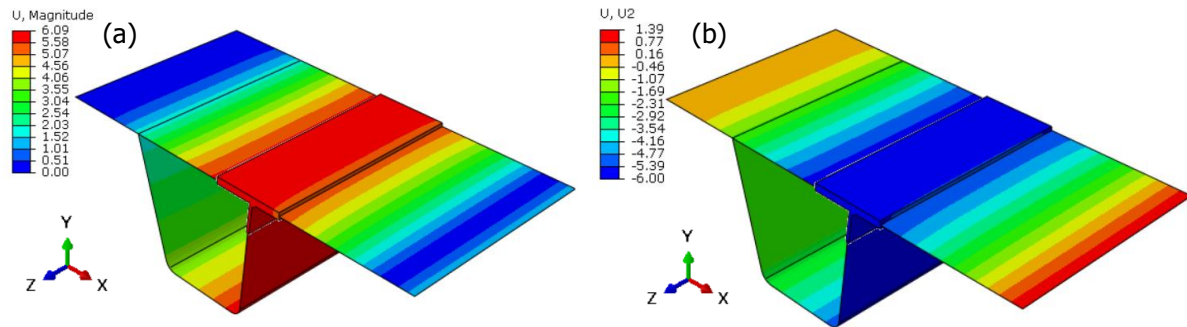
Figure 4.5 Deformation (a) Magnitude U (b) Vertical U2
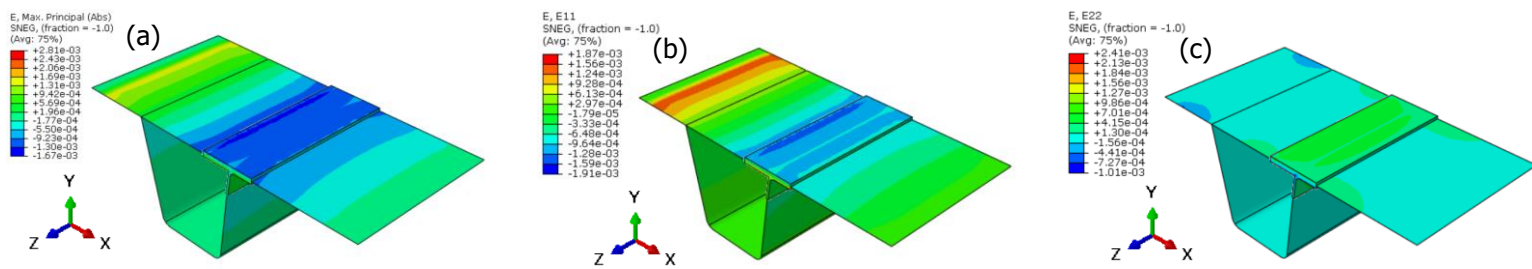
Figure 4.6 Strain Distribution (a) Max. Principal strain distribution (b) Strain distribution in x-direction (c) Strain distribution in y-direction
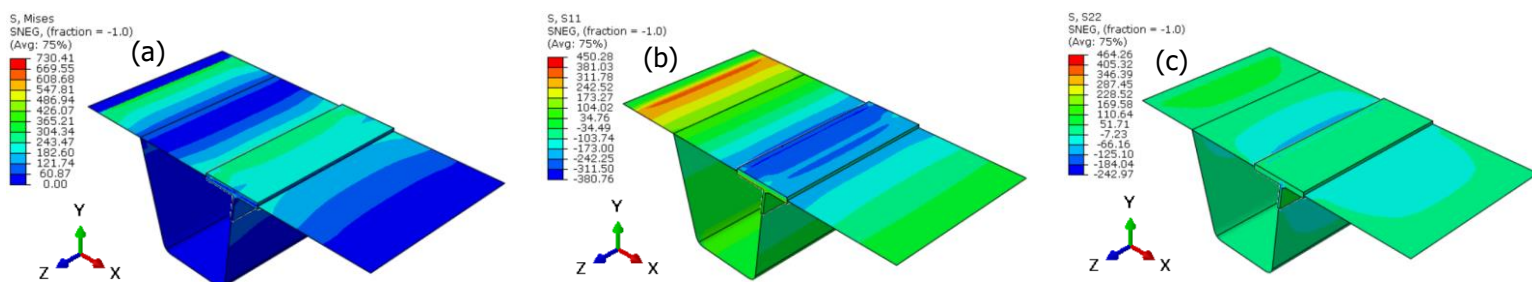
Figure 4.7 (a) Von-Mises stress distribution (b) Stress distribution along x-direction (c) Stress distribution along y-direction

Note: All the output results presented in this section are obtained from the static load simulation at -40 KN.

4.3.1 Results and Discussion

The reliability of FE model of defining fatigue behaviour depends upon the quality of the numerical model. Thus, a set of FE analyses are performed to validate the numerical model as per the test setup by evaluating the vertical deformation, longitudinal strain distribution and hotspot stress based on static cyclic loading sequence.

Comparison: Vertical deformation
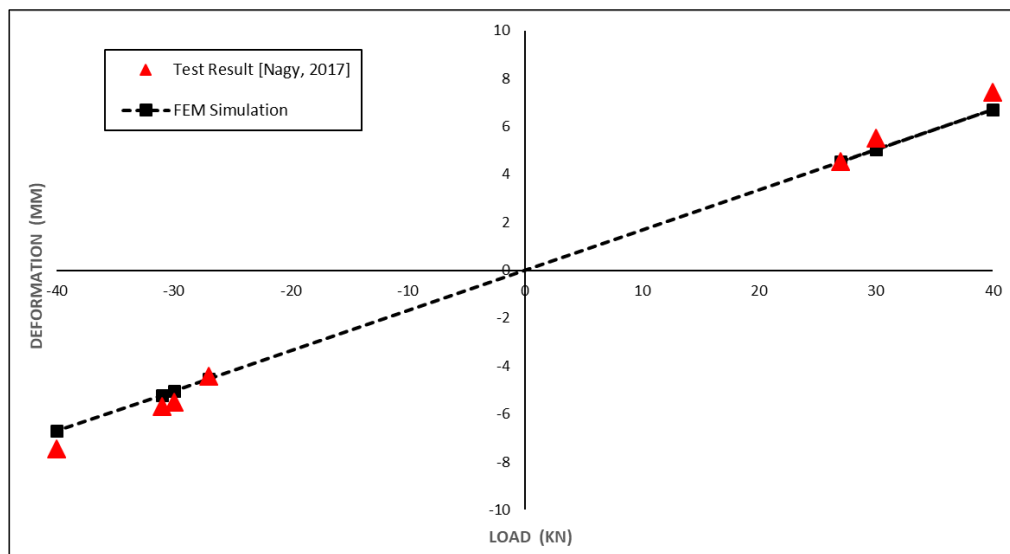
Figure 4.8 Comparison of the vertical deformation of FEM with test results

Figure 4.8 compares the results of vertical deformation of FEM simulation with the test data [25]. The simulated results showed a similar trend when compared with the test result. However, it can be noticed that the numerical vertical deformation is underestimated throughout. The difference increases with the increase in load (compression or tension) and goes up to a maximum difference of 9.2% at 40KN. The reason can be due to its configuration. In case of FEM, the results are those in vertical direction while those of the hydraulic jack system is according to the axle of the hydraulic jack itself which implies that if the hydraulic jack in setup was slightly inclined, this will result in large deflection due to its length. Another concern can be due to the imperfection in distribution of line load in the longitudinal direction. It is possible that more pressure is transferred to the edges or in the middle of the test specimen. Nevertheless, the simulated results were in roughly good agreement with the test data.

Comparison: Strain measurement
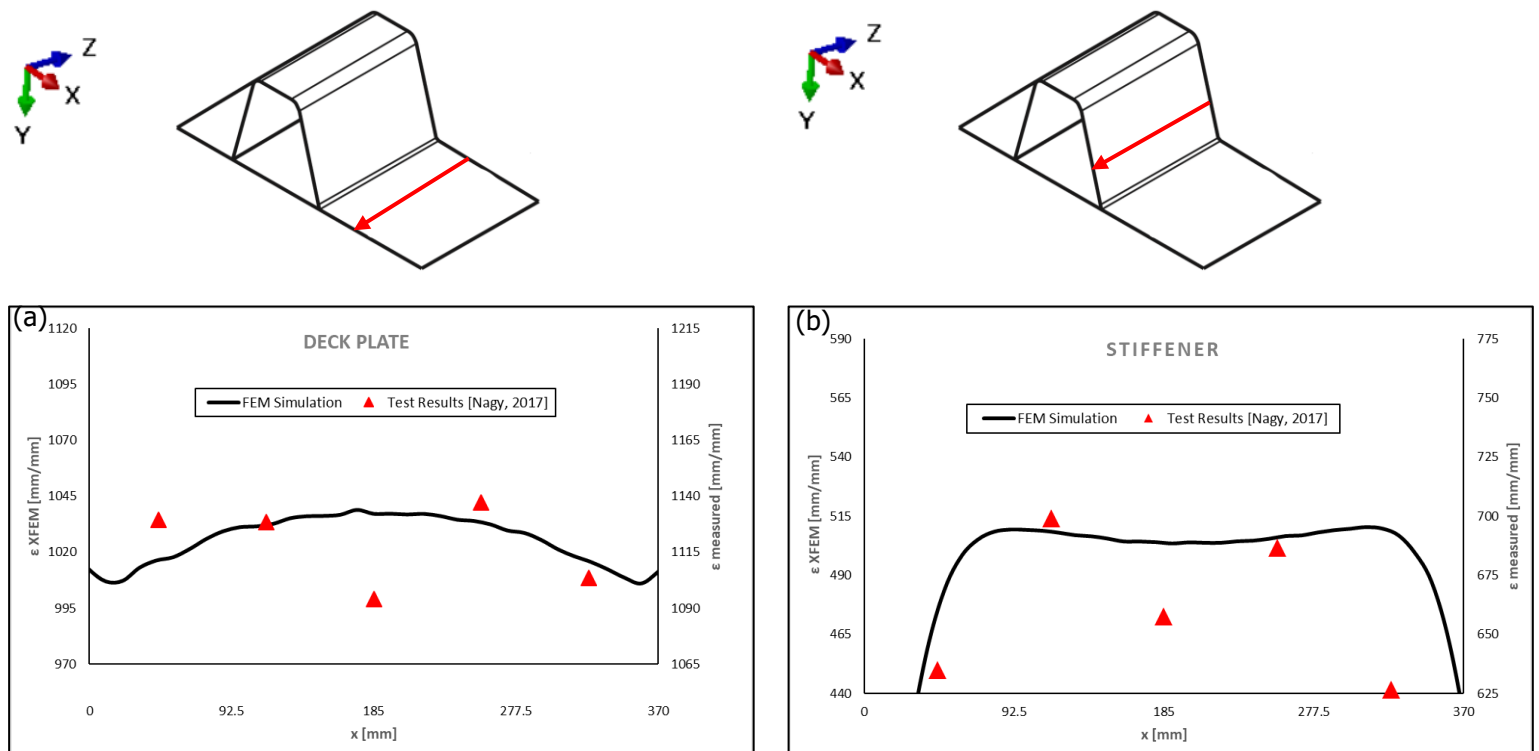
Figure 4.9 Comparison of longitudinal strain distribution between FEM and test results (a) Deck plate (b) Stiffener

The comparison of strain distribution along the longitudinal direction between the FEM simulation and the test result at -40KN of the applied cyclic load is illustrated in Figure 4.9. The simulated strain values (z-direction) are obtained at a distance of 25 mm away from the weld toe in both the plates while in the fatigue test, the strain was continuously recorded at specific locations in the longitudinal direction. When the simulated results are compared with test results, it is observed that the peak appears at one-quarter of the specimen in the both cases which can be due to the distribution of line load. However, there is a difference in the value which can be explained through the contact property. Since the FE model does not take friction (contact property) into account. Therefore, all the results from the strain gauges are arranged on an independent y-axis to able to shift the data points to the curve of the FE model for comparison. The difference in the magnitude is approximately about 7.8% in the case of deck plate whereas in case of the stiffener, the difference is much higher. Nevertheless, the simulated strain results showed a good correlation with the test results along the longitudinal direction for the respective plates.

Comparison: Hotspot stresses
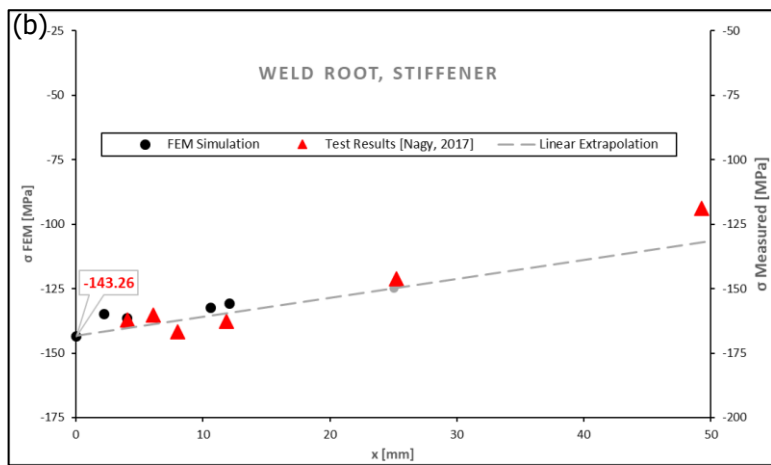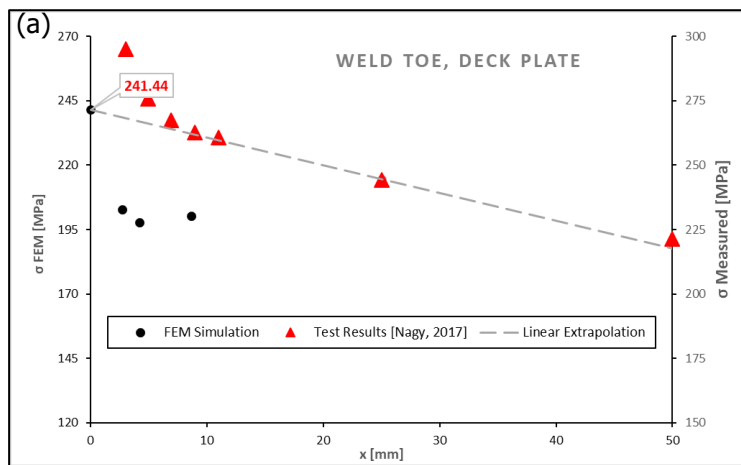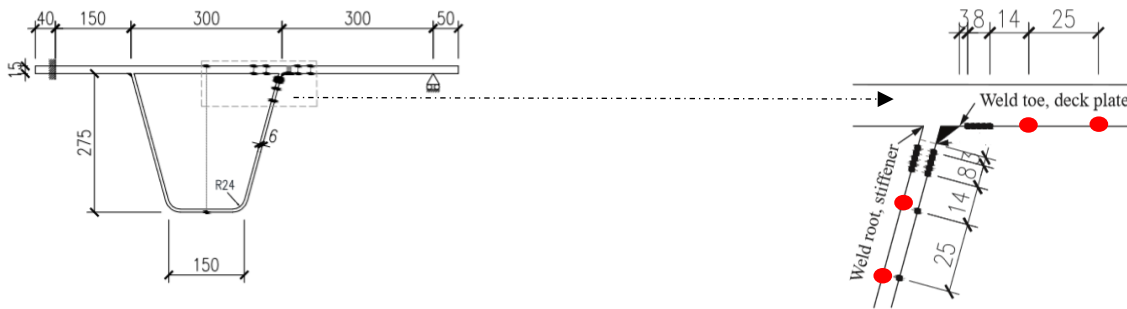
Figure 4.10 Comparison of hot-spot stress derived from FEM with the test results at weld toe (a) Deck plate (b) Stiffener

The hotspot stresses are derived at the weld toe in accordance with [26] by linearly extrapolating the stresses obtained at a distance of 25 mm and 50 mm away from the stress location. This methodology is used in FEM as it may lead to inaccurate stress peak result due to singularity (discontinuity). The results of the hot-spot stresses obtained at two critical locations from FEM are compared with test results illustrated in Figure 4.10. The left graph (Figure 4.10 (a)) represents the stresses in the deck plate towards the weld toe location. It is observed that the line of extrapolation almost coincides with the test result. However, the difference in the hotspot stresses can be due to the use of linear tetrahedral elements. These elements have one constant strain which can lead to the discretization of error. Moreover, an incompatibility of mesh is realised at the interface between the tetrahedral elements and the brick elements. On the other side, the right graph (Figure 4.10 (b)) represents the stresses in the stiffener towards the weld root location. In this case, the simulated results along with linear extrapolation line perfectly matches with the test result but slight difference in the magnitude. The possible explanation of this inaccuracy can be due to the imperfection in the geometry of the weld. As per the recommendation [27] , there should be a gap of maximum 2 mm in rib-to-deck welded connection at the root of the weld. However, this imperfection will hardly influence the result, if compressive stress exists at the location. Nevertheless, the simulated result showed a good agreement with the test data and this method of determining the hot-spot stress showed its reliability.

4.4 Numerical simulation of crack propagation- XFEM

4.4.1 Fatigue Test [25]

In the fatigue test, crack evolution was determined through beach mark measurement. These beach marks were measured at the location with the highest crack propagation in depth. Furthermore, the global crack shape resembles an elliptical shape. Furthermore, the crack not always originated from the middle of the specimen but sometimes at a quarter distance from the edge.

Figure 4.11 Longitudinal crack geometry during crack propagation for test specimen [25]

Based on the results carried out from the fractographic analysis, the initial crack length was estimated using SEM (Scanning electron microscope) while the final length was determined through the ductile tensile fracture. The initial and final crack length was found out to be $288.25\ \mu m$ and $2173.21\ \mu m$ respectively.

4.4.2 Development of XFEM model

While developing the XFEM-model for automated crack propagation, some assumptions were made based on the fatigue experiment (section 4.4.1). Firstly, a semi-elliptical initial flaw was assumed shape with half-length a of 0.3 mm along the minor axis and a half-length c of 0.6 mm along the major axis. Based on the fractographic results from the fatigue experiment, the size of the crack varies around 0.3 mm. The choice of the initial crack size is extremely sensitive to the fatigue life predictions. Often, an initial crack length is chosen between 0.1 mm and 1 mm [28]. Since the longitudinal stiffener is welded from only one side to the weld, and even the level of penetration is questionable, the initial elliptical crack length can go up to 1 mm and 0.5 mm in the longitudinal and transversal direction respectively [28]. Secondly, the crack is assumed to be originating from the centre of the specimen. Thereby, the initial flaw was positioned at the weld toe perpendicular to the deck plate (Figure 4.12 Figure 4.12).
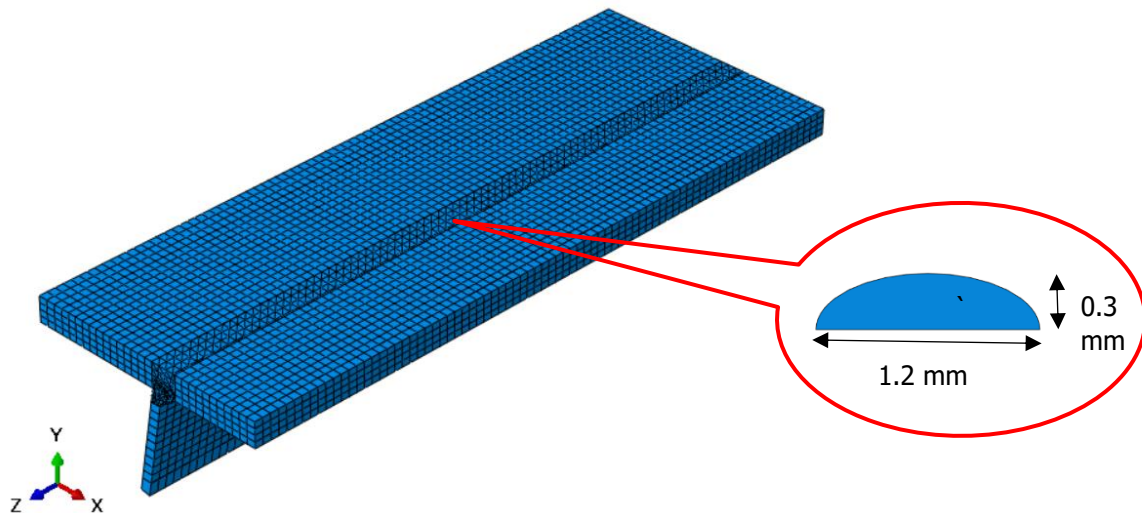
Figure 4.12 XFEM model: Location and definition of the initial elliptical shape

LEFM implementation

VCCT was used in the XFEM-based linear elastic fracture mechanics for crack propagation analysis using the direct cyclic approach with a time increment size of 0.05 per cycle. The direct cyclic load simulation is based on the periodic function (equation 2.12) and the parameter used is tabulated in Table 4.2.

Table 4.2 Direct cyclic parameters

R_σ	Load (N)	A_0	A_1	B_1	t_o	ω
0.0	31000	0.5	0	0.5	0	2π

The direct cyclic approach is combined with the Paris law crack growth to simulate the crack propagation. These fatigue crack growth rates are evaluated based on assigned VCCT parameters (Table 4.3). The crack propagation appears when the energy available for the crack is high enough to overcome the fracture resistance of the material. Since ABAQUS® analyses the fracture by the strain energy criterion approach, the Paris law parameters C_3 and C_4 were calculated assuming plane stress situation from equation (2.8) and (2.14) and are listed in Table 4.3.To ensure the start of crack growth process, material constants C_1 and C_2 were kept negligible as 0.001 and 0 respectively. Once the onset of the fatigue crack growth is satisfied (equation 2.13), the crack propagation rate can be computed based on the fracture energy release rate (equation 2.14).

Power law mix-mode model is selected for evaluating the equivalent fracture energy release rate represented in the equation (2.15) because of its simplicity in the relation of different modes of fracture.

It should be noted that the fracture toughness depends upon the temperature, steel quality and loading frequency. The temperature plays a vital role in determining fracture toughness, because the steel

becomes more brittle at low temperatures, resulting in a lower fracture toughness. The test results [29] for the fracture-toughness K_{IC} of A588 structural steel grade varied from 30 $MPa\sqrt{m}$ and 67$MPa\sqrt{m}$. This scatter can be possibly used, as the S355 steel grade was used in fatigue test. Therefore, this data was taken as the base of this study and applied to the XFEM-model assuming equal fracture modes tabulated in Table 4.3.

Table 4.3 Critical energy release rate Gc and Paris constant

Paris law constant (XFEM)		Critical energy release rate Gc (Nmm^{-1})			Exponent		
C_3	C_4	Mode I	Mode II	Mode III	α_m	α_n	α_o
12.99E-06	1.5	11.9	11.9	11.9	1	1	1

4.4.3 Output

Figure 4.13 display the output of automated XFEM simulation and crack growth mechanism. The crack initiating from the weld toe propagated in both longitudinal and vertical direction. It should be remembered that the direction of crack growth is governed by the distribution of SIF at the crack front. As the shape of the initial flaw was assumed to be semi-elliptical, the growth followed almost in elliptical fashion. Figure 4.13 (a) displays the crack growth at different stage in propagation. As the crack propagated in depth, three parameters namely crack size a, crack length $2c$ and corresponding number of cycles N were precisely noted. Figure 4.13 (d) displays the simulated crack front dimension after 2.30×10^5 cycles.

(a) $N_f = 1.2 \times 10^5$ cycles $N_f = 2.0 \times 10^5$ cycles $N_f = 2.15 \times 10^5$ cycles

(b)

7.5 mm

Initial crack flaw

(c)

15 mm

7.5 mm

(d)
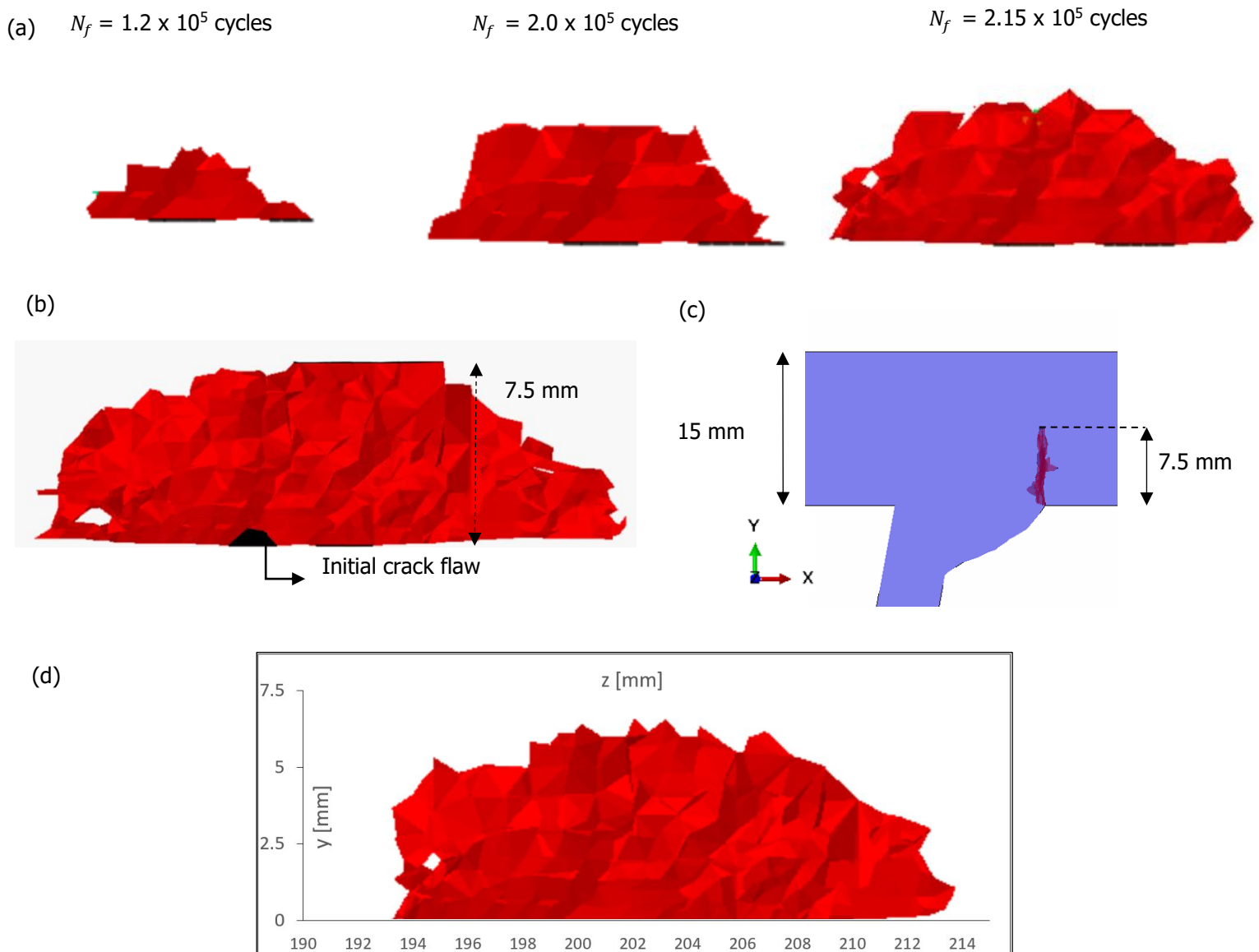
Figure 4.13 (a) Stages of crack propagation displayed as STATUSXFEM output (b) XFEM crack simulation including the initial semi-elliptical crack (c) Side view corresponding with the weld toe crack simulation (d) Crack front dimension

4.4.4 Results and Discussions

Figure 4.14 displays the results of fatigue crack growth obtained from XFEM simulation are compared with the test results [25]. The test results were derived from the beach marks measurement in 11 cycles intervals (Appendix B). Assuming the final failure when a crack size is one half of the deck plate's thickness [26], the results of XFEM simulation were calculated until the crack propagated to 7.5 mm in depth (Figure 4.14). The shape of fatigue crack propagated keeping the elliptical shape due to the use of tetrahedron elements the corresponding SIF distribution along the crack front of the assumed crack shape.
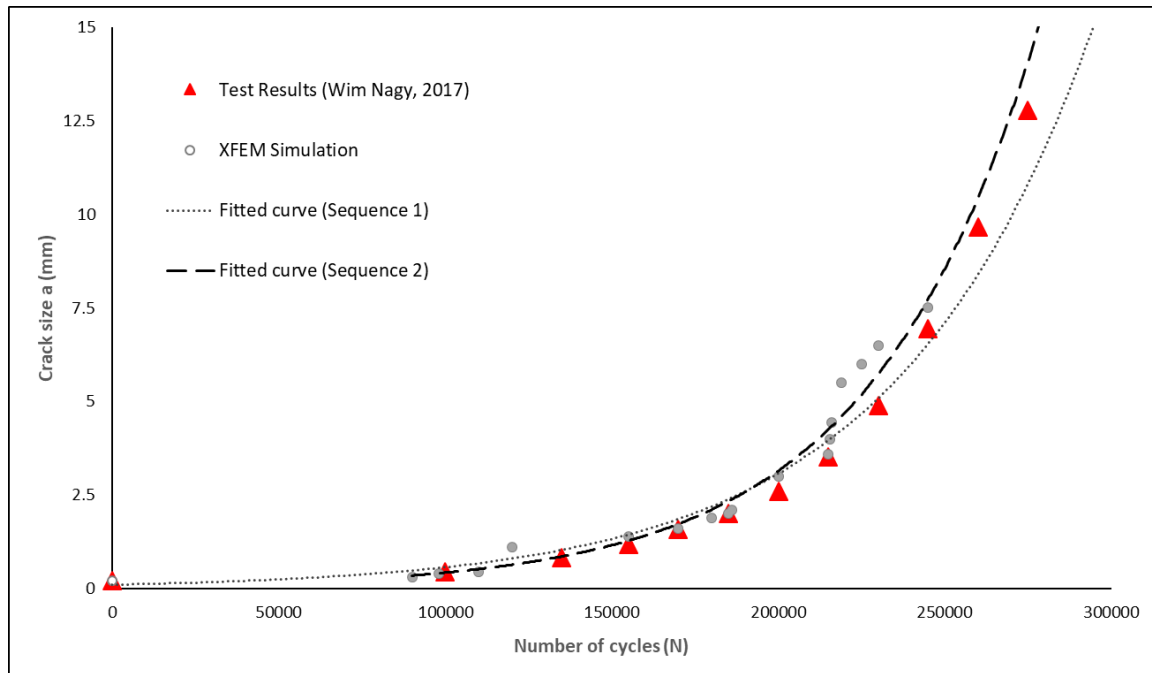
Figure 4.14 Fatigue crack growth from XFEM simulation is fitted with test results in two sequence

There are two different sequences considered to define the curve fitting. The first sequence is based on all the simulated crack results including the initial crack size whereas the second sequences is based on all the simulated crack results excluding the initial crack size. After a crack depth of 5 mm the crack growth seems to be arrested. The possible reason can be due to higher stress redistribution at the crack tip due to which the crack growth shifted in the longitudinal direction. Later, the crack growth becomes unstable after 7.5 mm resulting in irregular crack propagation.

From Figure 4.14 , it has been observed that the fitted curve of sequence 1 (includes initial crack size) overestimates the number of cycles to failure. Moreover, the final length is conservative and can be explained by the assumed size of the initial crack. Since the accuracy of the crack propagation analyse is extremely sensitive to the initial crack size, the conservative result in sequence 1 can be explained. Thereby, it is not desirable that the Paris constants depend on the size of the initial flaw. As a result, the initial crack size is not considered in the sequence 2. It is noted that sequence 2 resulted in the good correlation with the beach mark measurement and the calibrated Paris law constants C comes out to be 55 % lower when compared with recommended IIW standards [30]. Hence, sequence 2 can be used in estimating the number of cycles required the crack to reach the deck surface. Furthermore, this curve fitting (sequence 2) can be used to compute the initial crack size by extrapolation.

Chapter 5

FATIGUE LIFE ASSESSMENT: SUURHOFF BRIDGE

5.1 General

5.1.1 Motivation

Post world-war, many orthotropic steel bridges have been built between 1960 and 1980 across Europe, especially in the Netherlands. Since these bridges were not designed to withstand the current traffic intensities and are therefore prone to fatigue damage. Many localised failures have developed in welded steel bridge components due to fatigue crack propagation which eventually lead to brittle fracture. The amalgamation of low steel quality, high traffic intensities and suboptimal weld detailing can create fatigue issues in existing bridges that could compromise the structural integrity of the bridge. Numerous fatigue cracks are found in the welded connection which are susceptible to fatigue crack propagation only after they came into function. As the infrastructure ages, the costs of renovation and maintenance escalates and are becoming significant to the continued service. As such, no set of norms can adequately ensure the safety and reliability of all the existing structures [31]. As a result, periodic inspection is being executed at regular intervals to accumulate the damage.

5.1.2 Problem description

 At this moment, Rijkswaterstaat is busy with the detection, reparation and renovation of the existing steel bridges in Netherlands. Several fatigue crack problems are being regularly inspected in Suurhoff Bridge, Rotterdam. One such type of fatigue crack is the welded connection of the deck plate to the trapezoidal closed longitudinal closed ribs between the cross-beams. This detail is often decisive for the fatigue behaviour of the OSD because of high stress ranges and direct wheel loading. The closed ribs constrain the transverse deformations of the deck plate making this detail prone to fatigue failure [32]. Although these cracks do not endanger the overall structure, but the in-situ repairs are difficult and expensive. In 2016, a crack length of 230 mm was detected in the stiffener-to-deck plate connection at mid-span between two cross-beams using TOFD method. The crack propagated through the deck plate originating from the weld root. These types of cracks are generally considered dangerous as they are not visible when the crack starts to penetrate through the deck plate because of the location of the crack initiation. Moreover, these cracks already cause significant damage before the crack front reaches the surface. At this stage, the crack is not stable and propagates proportionally. Moreover, Rijkswaterstaat has set a permissible limit for deck plate crack length of 500 mm [33]. At this moment, these cracks must be repaired immediately.

To verify this issue, fracture mechanics can be an ideal choice since it can be used to model and analyse fatigue crack propagation till subsequent failure and correlate the results with inspection data. This approach is a reliable alternative, especially when the S-N curve-based calculation procedure does not predict enough structural capacity, consequently avoiding unnecessary strengthening of the detail. However, analyses based on fracture mechanics requires high computational effort and a detail insight of geometry, material condition. This method allows the concerned authority to choose between the renovation interval and the preventative strengthening.

5.1.3 Suurhoff bridge description

The Suurhoff bridge is a beam-girder bridge with an orthotropic steel deck, situated over the Hartelkannal in Rotterdam, Netherlands. It spans 232.75 [m] and is the last bridge of A15 national highway before reaching the Maasvlakte. The bridge is a combination of a steel girder bridge and bascule bridge. The movable part is located on the north side of the Hartelkannal. There is a connection of slow traffic on the eastern part of the bridge and a double-track railway line over a separate steel cable-stayed bridge is situated adjacently on the western side. Figure 5.1 depicts an overview of the location of the Suurhoff bridge.

In early 1970s, Suurhoff bridge was built at the time when the Hartelkanaal was dug. The bridge with 2x2 lanes opened for traffic in 1972. Next to the traffic bridge, a railway bridge was built in 1973. Both the bridges were named after Minister Suurhoff (1905-1967).
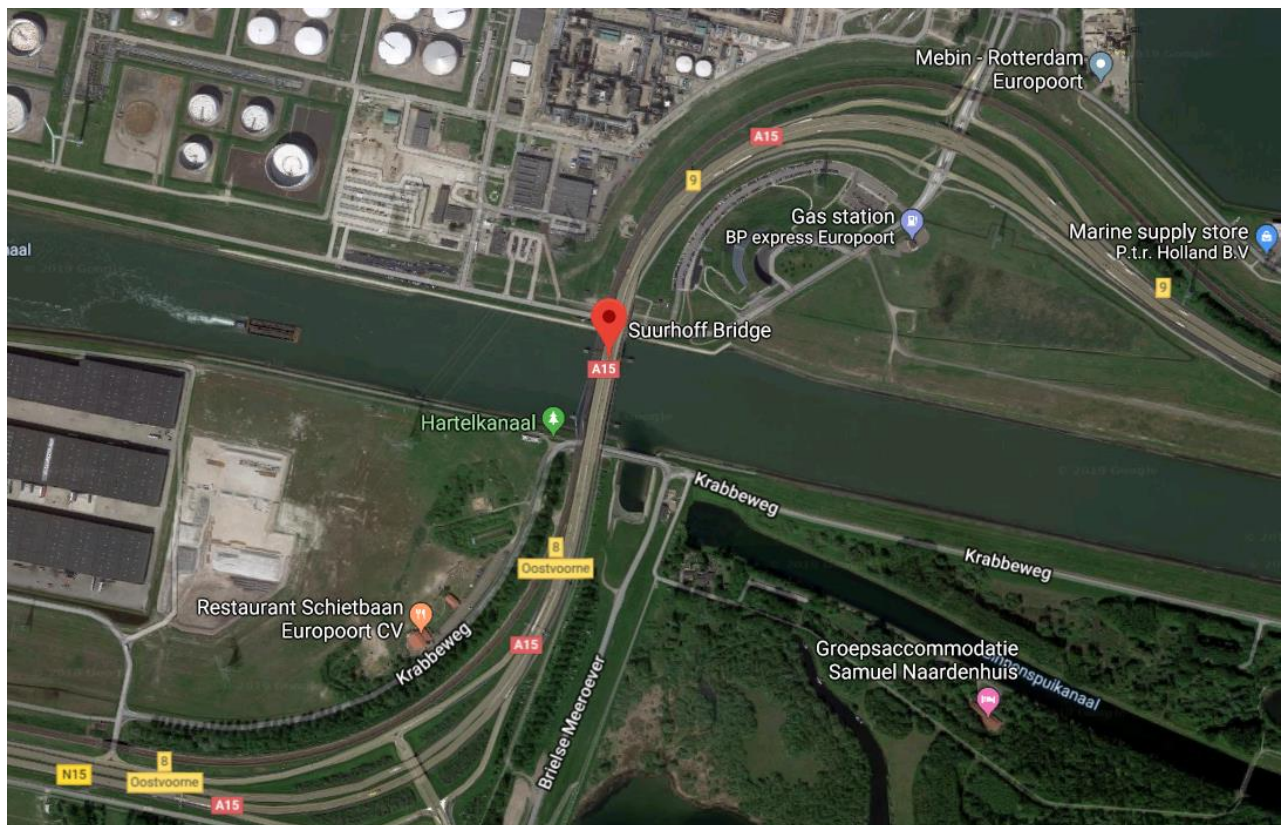
Figure 5.1 An overview of the location of the Suurhoff bridge

The steel road bridge consists of two parts: fixed and movable part which can be sub-divided into three segments as SV01, SV02, SB01. The movable part (SB01) is in between the fixed parts (SV01 and SV02). Thereby, the total length of 232.75 [m] is divided into 150.80 [m], 33.90 [m] and 48.05 [m] for SV01, SB01 and SV02 segment respectively (see Figure 5.2).
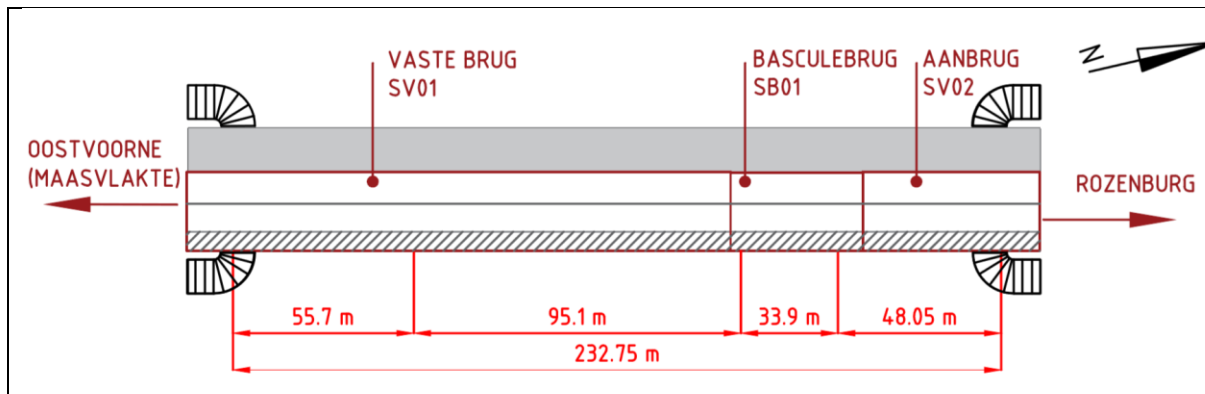
Figure 5.2 An overview of the global dimensions of the bridge (Top View)

The width of the bridge is 24.12 [m] consisting of 2x2 traffic lanes with a pedestrian lane on the eastern side as shown in Figure 5.3. The lane configuration has been used since the operation of the bridge in 1972. For current use, lane no. 1 and 4 are the slow lanes and lane no. 2 and 3 are fast lanes.
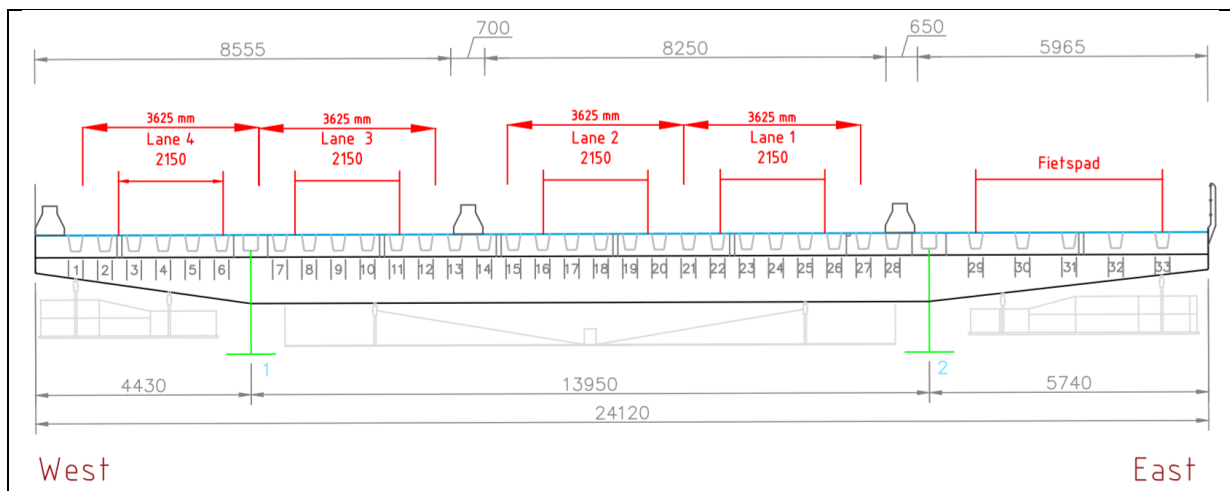
Figure 5.3 Cross-section of the fixed part of Suurhoff bridge (SV01 and SV02)

The OSD of the fixed part of bridge (SV01 and SV02) consist of a 10 mm deck plate with 50 mm asphalt surfacing is welded to 5 mm thick trapezoidal stiffeners. The longitudinal stiffeners are 320 mm high and 300 mm wide on top and have a width of approximately 200 mm with radius of 17 at the lower soffit. The spacing between the two consecutive longitudinal stiffeners is equal to 300mm. An overview of these dimensions is given in Figure 5.4. The spacing between the cross-beams is 4540 mm.
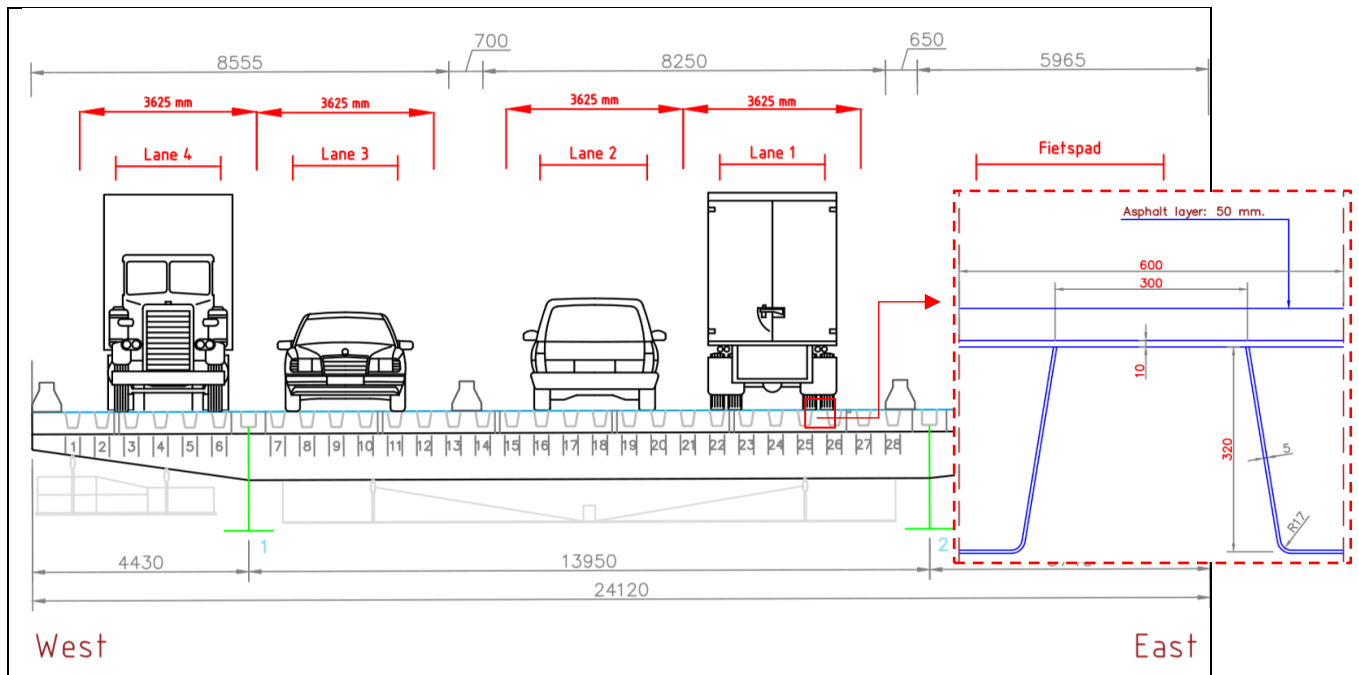
Figure 5.4 Details of the investigated bridge (units: millimetres) - Cross-section of the detail

The inspection was executed between trough number 24 and trough number 27 to accumulate the fatigue crack in the deck plate originating from the weld root using TOFD method in the fixed part (SV01) of the bridge. Therefore, this research focusses on the fatigue cracks originating from the root of the welded connection between the deck plate and longitudinal stiffener in the span between the cross-beam of SV01 segment of the bridge.
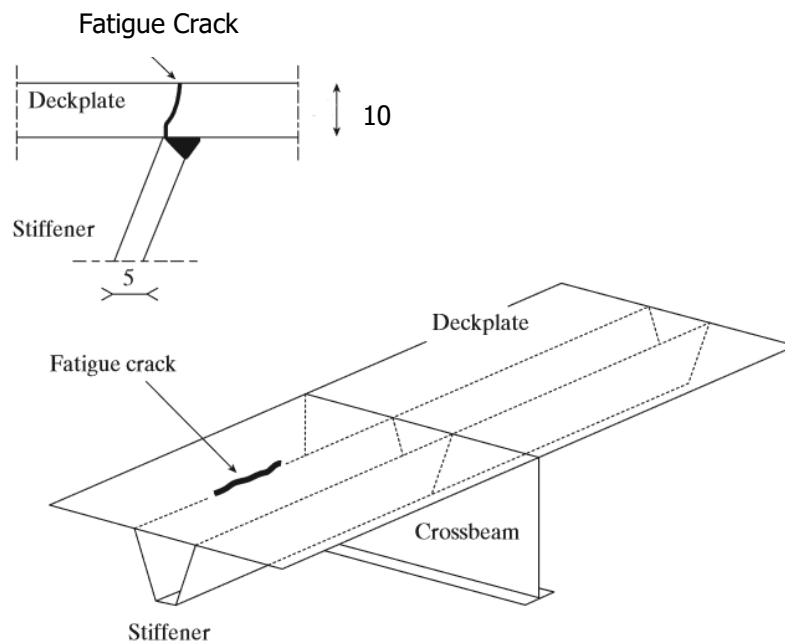
Figure 5.5 Location of the fatigue crack (units: mm)

5.2 Outline: Fatigue life Assessment

The main objective of the research is to develop a numerical model and correlate its simulated results with the inspection data and/or existing numerical model provided by Rijkswaterstaat in fatigue assessment. Later, the model will be used in predicting the permissible limit of deck plate i.e. 500 mm crack length. In developing the numerical model, some parameters were studied from the literature and implemented in the model. Further, the analysis is performed on fatigue assessment aiming to predict the crack initiation and crack propagation period. Thereby, this report is divided into two segments namely fatigue crack initiation period and fatigue crack propagation period. An outline of this research is illustrated in Figure 5.6.
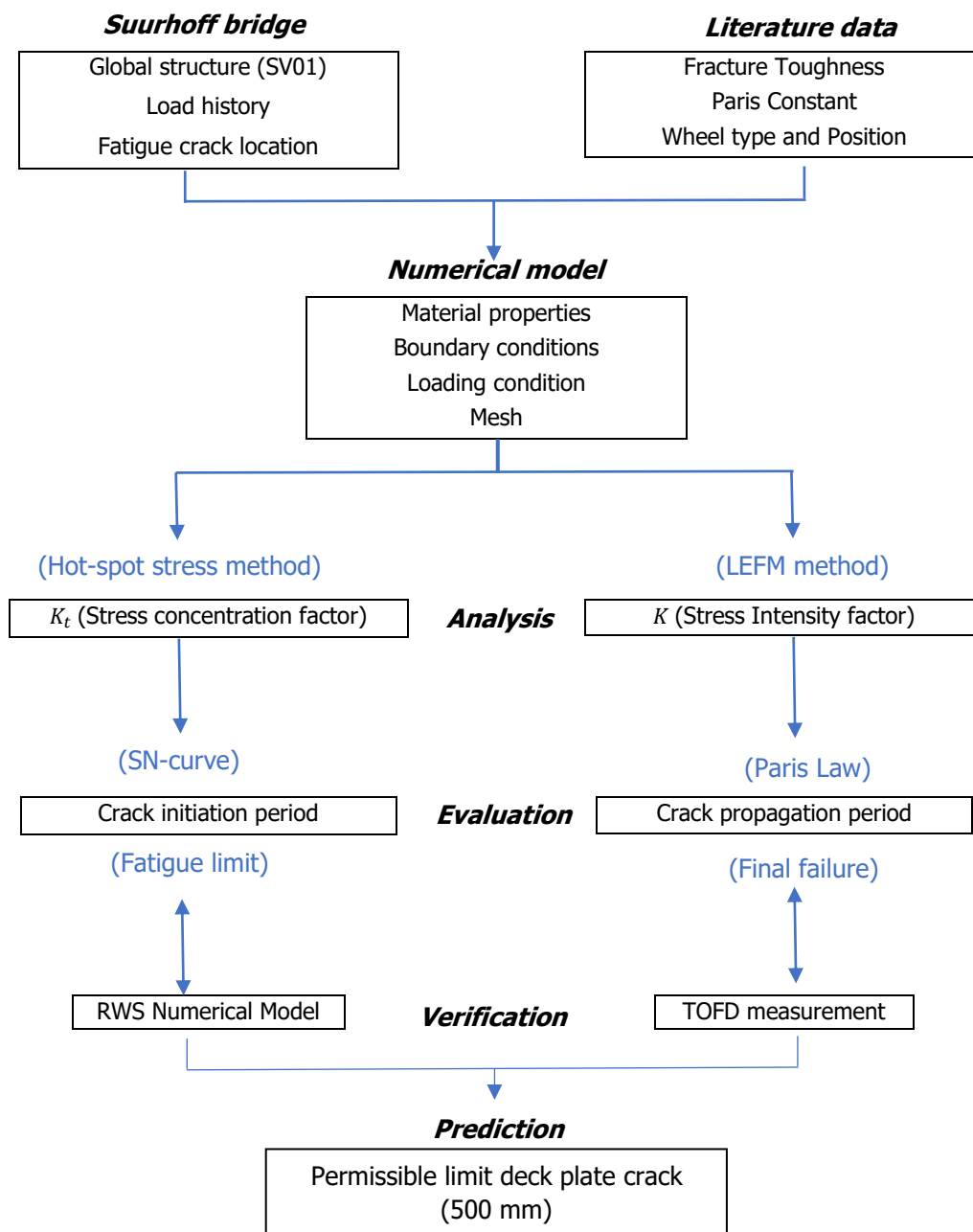
Figure 5.6 Outline of the research

5.3 Literature Data

5.3.1 Material Parameters

Fracture toughness

The steel grade of the OSD of Suurhoff bridge is S355. However, it should be noted that the fracture toughness depends upon the temperature, quality of steel and the loading frequency. From the comprehensive collection of data by [29], the value of plane-strain fracture toughness (K_{Ic}) varied from 27 $MPa\sqrt{m}$ and 60 $MPa\sqrt{m}$ for structural steel (A36) and from 30 $MPa\sqrt{m}$ and 67 $MPa\sqrt{m}$ for structural steel (A588).

The temperature plays a vital role in determining fracture toughness, as the steel becomes more brittle at low temperatures, resulting in a lower fracture toughness. Particularly for bridges in the Netherlands, the lowest possible service temperature is assumed to be -20 $°C$. Taking in account all the above factors, the fracture toughness is taken K_{Ic} = 50 $MPa\sqrt{m}$ as the base of this study.

However, it is advisable to either use existing test results or perform a new fracture toughness test to obtain more accurate value of fracture toughness.

Paris constants

Material dependent parameters C and m determines the quality of fatigue life prediction, when using Paris Law for describing the crack propagation. These parameters should be determined preferably based on field measurement or material test [34]. Since material tests of the base metal (deck plate and trough stiffener) are not available, the Paris constants used are based on the available literature. Many researches have tried to predict the material constant through fatigue experiments (Table 5.1). Unfortunately, these parameters vary significantly. Furthermore, a distinction should be made between the fatigue growth behaviour in the base metal, in the heat affected zone (HAZ) and in the weld metal for detail numerical analysis. Due to welding, different sub-layers with several microstructure changes the behaviour of the base metal. As a result, Paris law constant can differ at such location. The International Institute of Welding (IIW) [30] makes a distinction between the weld material and base material and recommended a value of C equals to 3×10^{-13} for the base material and 5×10^{-13} for the weld bead. In this research, the material constant of base-metal recommended by IIW is assumed constant in the OSD model as the crack encounters a minute region of HAZ while originating from the weld root and propagating in the deck plate.

Nevertheless, multiple standards/authors have proposed a safe value for Paris constants that have been used in the past is summarised in Table 5.1 and Figure 5.7.

Table 5.1 Paris constants proposed by different authors for structural steel

Source		C	m	ΔK_{th}	R	Reference
British Standards (2007)		5.21×10^{-13}	3	63	0	[35]
Kuhn *et al.* (2008)		$4.00 \cdot 10^{-13}$	3	170	0	[34]
Maljaars *et al.* (2012)		$3.00 \cdot 10^{-13}$	3	80	0	[36]
Bignonnnet et al. (1991)		4.25×10^{-13}	3	50-71	-1	[37]
Hobbacher (2015)	base metal	$3.00 \cdot 10^{-13}$	3	63	0	[38]
	weld metal	$5.21 \cdot 10^{-13}$	3	63	0	

*For dN in mm/cycle and ΔK in MPa√mm.
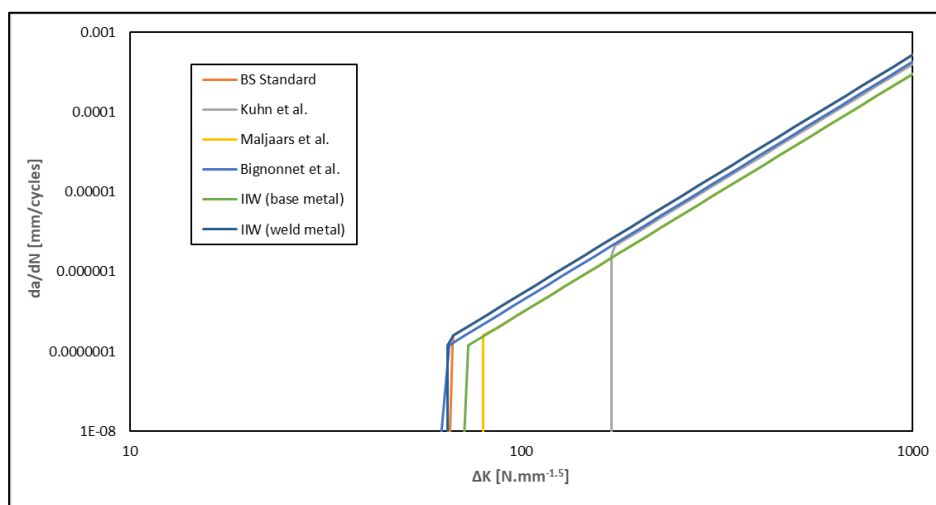
Figure 5.7 Crack propagation curves based on literature

5.3.2 Loading Parameters

Fatigue is a time-dependent phenomenon. Although the fatigue limit state is an ultimate limit state, the approach to design or verify is different because the failure is associated with the cumulative damage caused by repeated application of same levels of stress. Hereby, the ultimate strength is therefore irrelevant, and the stresses must be based on the elastic stress analysis.

Wheel type-position (Transversal):

In a numerical study [39] performed on the welded connection to determine the most unfavourable transverse position and type of the wheel load for weld root stress and the conclusion drawn are as follows:

- The bending moments (M_x) are smaller in the case of wheel type B (FLM4 Eurocode) due to larger dispersion of load over the surface.
- Wheel type A resulted in largest bending moment when the wheel load is in between the two longitudinal stiffeners ($x = -40\ mm$).

Position x indicates the left edge of the wheel with respect to the left edge of the left stiffener-to-deck plate connection (Figure 5.8).
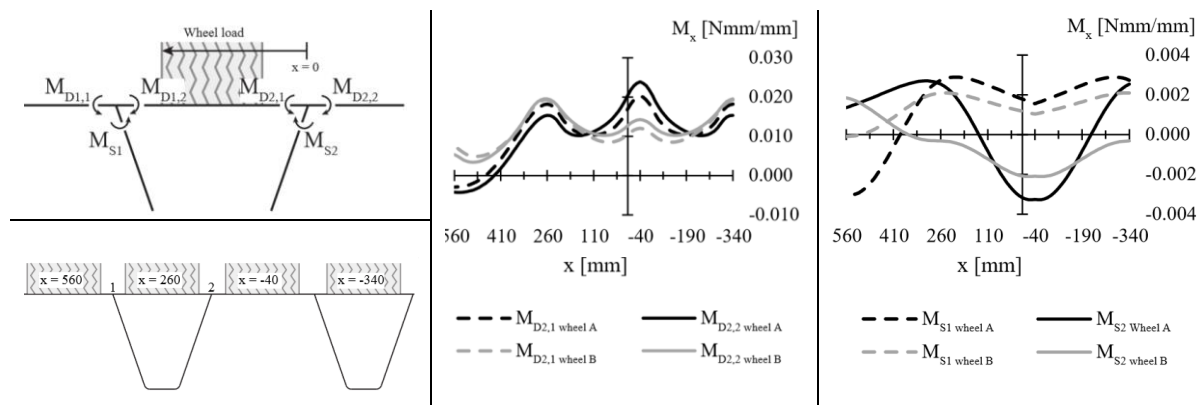
Figure 5.8 Influence lines of the bending moments in the deck plate and stiffener for an axle load of 1N using wheel type A and B. [39]

Since the geometry of the welded connection between the deck plate and stiffener resembles to the geometry of the numerical model, above conclusions can be used as the starting point and possible explanation of type of wheel selection. It is observed that wheel type B results in the least bending moment whereas, wheel type A and wheel type C are dominant in creating higher contact stresses at the weld location.

The usual practice for fatigue assessment is to assume high tensile residual stresses generated from the welding and neglect the mean stress effect. This results in the simplification of the entire stress range ($\Delta\sigma = \sigma_{max} - \sigma_{min}$) is effective in terms of fatigue crack growth and not as a function of mean stress. However, it is to be remembered that the fatigue crack growth depends on the loading sequence (stress ratio R = $\sigma_{min}/\sigma_{max}$) and the frequency of the load.

In this research, wheel type A (NEN 8701) for reverse stress ratio (R=-1) is adopted in the model situated at the middle of two longitudinal stiffener (trough no. 25 and 26) in the transversal direction (see
Figure 5.4) and at the centre between the two cross-beams in the longitudinal direction ensuring most unfavourable position for the weld root stress.

Number of cycles (N)

Fatigue load models were derived from the traffic measurements on Dutch highway bridges and implemented in NEN 8701 [40]. According to NEN 8701 Article 5.2 (3) the following fatigue load models (FLM) should be applied in the fatigue verification of steel road bridges:

- ✓ FLM 4a: set of 'standard lorries' (for materials primarily dependent on the stress ranges).
- ✓ FLM 5: based on recorded road traffic data.

Moreover, NEN 8701 Annex A.1 (2) recommended to determine the number of vehicles per location based on observation or based on the category classification of NEN -EN 1991-2 [41].

According to the standardised tables in Annex A.2 from NEN 8701, the recorded traffic data is categorised in three time periods as Opening (1972)-1990, 1991-2010 and 2011-future (2040) with different sets of vehicles in each period. The recorded traffic data on slow lane in one direction of the Suurhoff   bridge   is   graphically   represented   in
Figure 5.9. The detailed traffic distribution is tabulated and can be found in APPENDIX C. The dynamics effects and development in time are here excluded here (a load increase of 20% in 100 years is estimated).
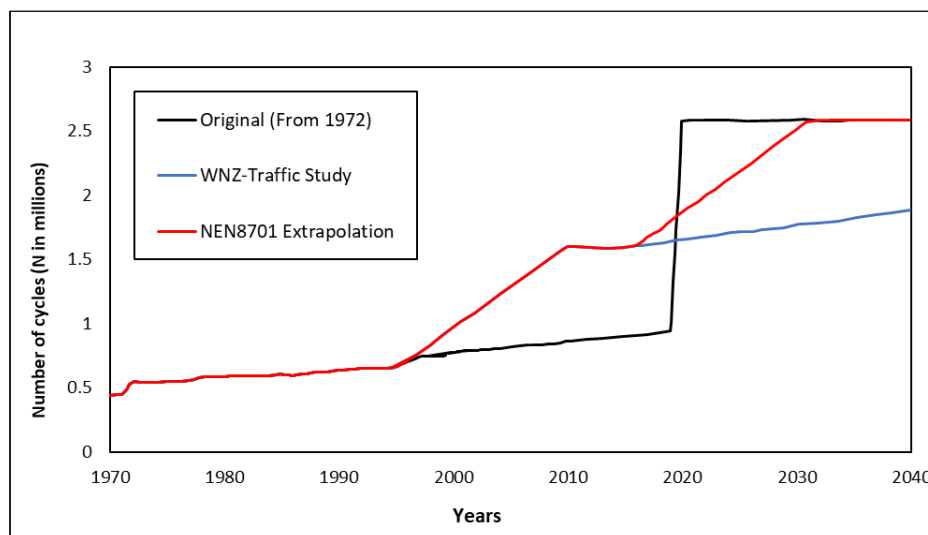
Figure 5.9 Recorded traffic numbers on the slow lane in one direction traffic [42]

It should be noted that the traffic increase is significant once the 2nd Maasvalakte becomes fully functional in 2020 (see Figure 5.9). Beside original traffic record, two types of traffic extrapolation were used. One based on NEN8701 [40], which estimates the traffic to be doubled in 100 years and the second is based on traffic study performed by Rijkswaterstaat West-Nederland Zuid (WNZ). The latter

seems to be the underestimated especially after 2020, therefore NEN8701 extrapolation is used in this research.

As the Suurhoff bridge (A15) serves an important link between the Maasvlakte and the western part of the Voorne-Putten and Botlek, Europoort and Rotterdam, heavy loaded lorries are expected and therefore long-distance traffic type with high vehicle load is considered. Based on NEN 8701 extrapolation, the recorded traffic data per period is summarised in Table 5.2.

Table 5.2 Summary of the recorded traffic number based on NEN 8701

Period	N_{obs}/period	N_{obs}/year	Reference Year	High Traffic (15%)
1972-1990	10582163	556956	1981	83543
1991-2010	20747690	1037384	2000	155608
2011-2040	64726301	2157543	2025	323632

N_{obs}: Traffic observations as number of cycles

5.4 Numerical model

To study and assess the fatigue behaviour in the welded connection between the trough and deck plate, a full-scale FE model (Figure 5.10) is developed in an adequate manner according to the cross-section described in the Figure 5.4 from trough no. 24 to trough no. 27. The model consists of a deck plate welded to the longitudinal stiffener spanning between two cross-beams and extended further to half the distance between the cross-beams on either side. The FEM calculation of such model can be time-consuming; therefore, the model is developed in combination of shell and solid elements. At the crack location, the part is replaced by solid elements for XFEM calculation. To ensure adequate connection between them, the solid face is constrained to shell edge using shell-to-solid coupling. Moreover, the nodes of the longitudinal stiffener at the crossbeam position are tied in all the degree of freedom to the nodes of the cross-beam using tie-constraint. A gap size of 1mm is been used in rib-to-deck welded connection at the root of the weld.

■ Solid part ■ Shell part   ■ Shell (cross-beams)
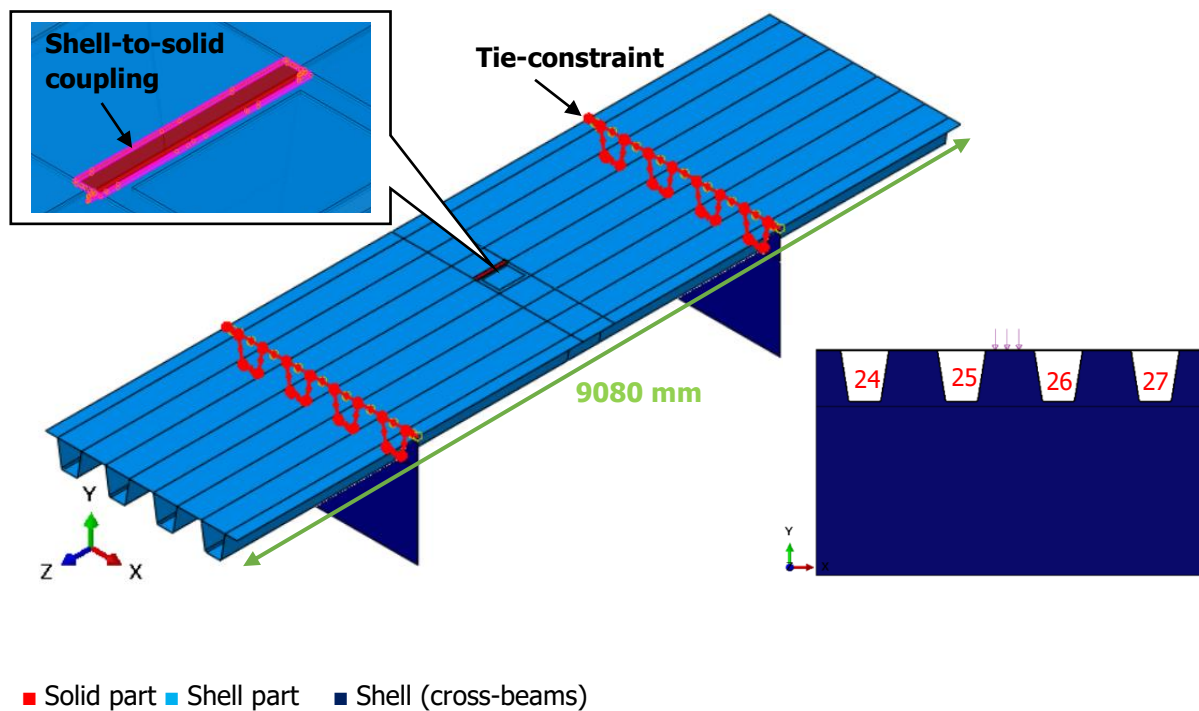
Figure 5.10 Illustration of numerical model

5.4.1 Material properties

There are three types of material parameters required for LEFM calculations. Firstly, the parameters defined in the elastic stage of the material i.e. Youngs' modulus and Poisons ratio which were assigned as 210000 MPa and 0.3 respectively. Secondly, the fracture toughness of the material which determines the ability to resist fracture. Thirdly, the materials constants (C and m) from the Paris Law equations which defines the rate of fatigue crack propagation. The latter two parameter types were adopted from the literature of existing steel bridge and will be discussed in LEFM implementation section.

5.4.2 Loading conditions

Figure 5.12 shows the configuration of wheel load type A (220 mm x 330 mm) used in the static analyses without considering the dispersion of load due to asphalt. In determining the hotspot stresses (static analyses) several loads are used ranging from 21.5 KN to 45 KN. However, a periodic cyclic loading sequence of reverse stress ratio is used in fatigue simulation varying from negative wheel load (KN) to positive wheel load (KN). Figure 5.11 depicts the loading sequence for a unit wheel load. Four types of wheel loads are used for automated crack propagation i.e. 40KN, 45KN, 50KN and 52.5KN. A positive load corresponds to a tensile load cyclic at the weld root. The direct cyclic loading parameters can be found out in Table 5.6.
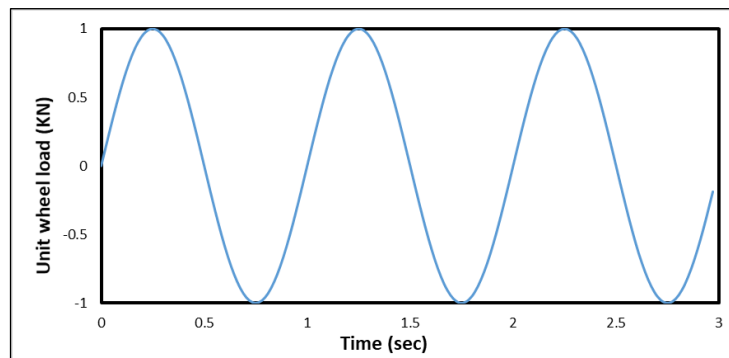
Figure 5.11 Loading sequence for fatigue simulation

5.4.3 Boundary conditions

In this research, a symmetric boundary condition is adopted as shown in Figure 5.12. The translation in x-direction is constrained along the deck plate boundaries and side edges of the cross-beams. Similarly, the translation of longitudinal troughs at either side of the longitudinal edges is restrained in z-direction. At two locations i.e., the bottom flange of the cross-beams and edges of the longitudinal troughs, vertical translation in y-direction is restrained. The crack flaw in the model is situated at the centre, the influence of boundary condition will hardly generate any error to the stresses near the crack tip.
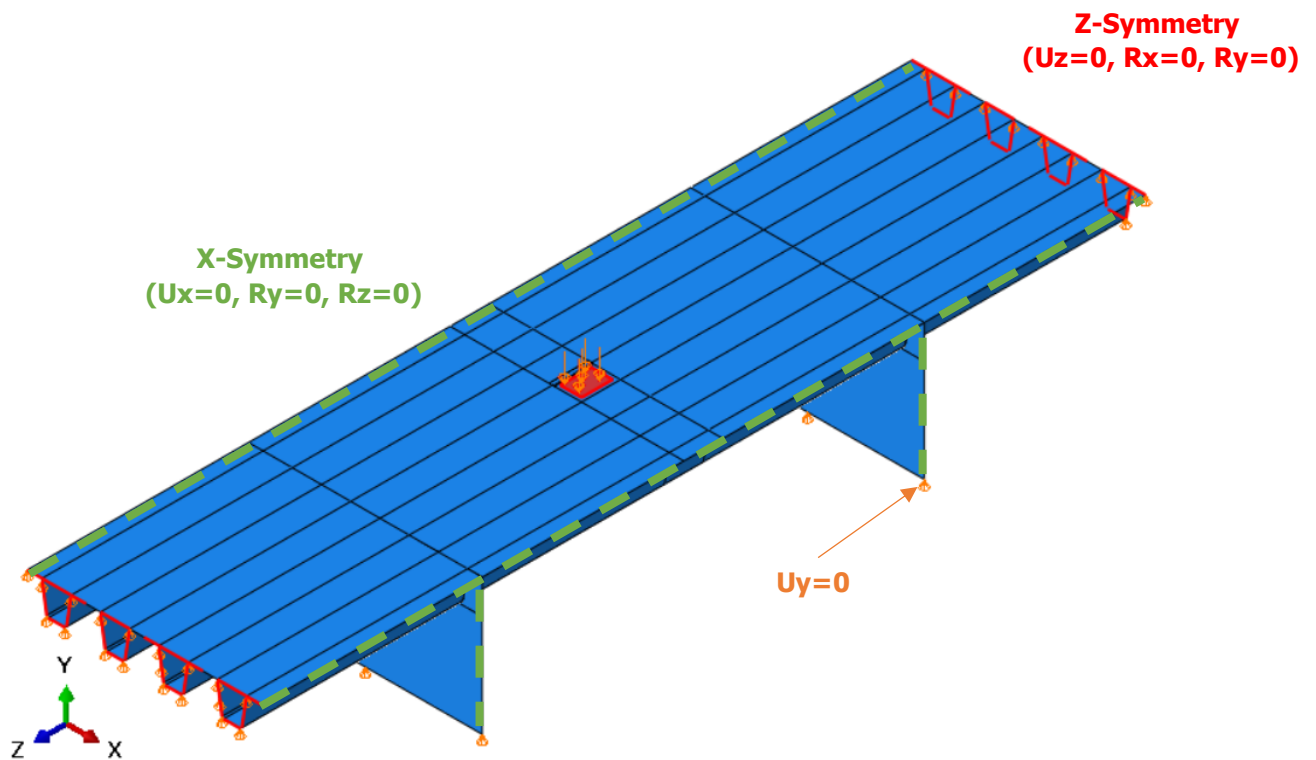
Figure 5.12 Numerical model: Boundary conditions

5.4.4 Mesh
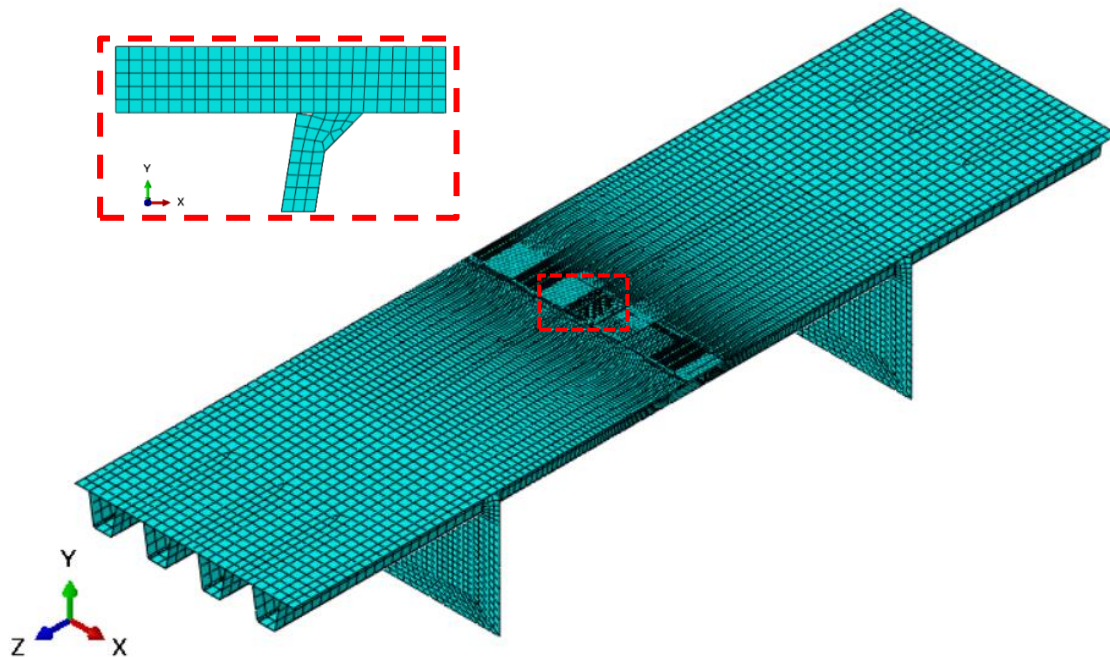
Figure 5.13 Numerical model: Mesh quality

The numerical model is built using shell elements excluding the crack region as shown in the Figure 5.13. The crack part (welded connection between deck plate and the stiffeners) of 400 mm is built with solid 8-noded brick elements as highlighted in the above figure. Particularly, at the loading region and crack location, a fine mesh should be used to accurately capture the stresses at the joint between the deck plate and longitudinal stiffeners. Since hotspot stress method requires to compute the stresses at 4 mm and 10 mm from the joint, the element size was therefore kept as 2mm. The size of the element is gradually increased to 25mm towards the cross-beams and 50mm in the remaining region to reduce the total number of elements. Due to its simplified geometry, the shape of the element is kept hexagonal throughout. For precision, 8-noded shell element (S8) of quadratic order was adopted at the loading region.

Table 5.3 Meshing details of the numerical model

Region	Element type	Mesh size
Solid part	8-noded brick element (C3D8)	2.00 mm
Shell (Loading region)	4-node shell (S4)	10 mm - 25 mm
Shell (Remaining region)	4-node shell with reduced integration (S4R)	50 mm

5.4.5 Output:

A preliminary stress distribution is presented in this section mainly focussing at the weld root and aiming to determine the unfavourable position, where the crack can be positioned.
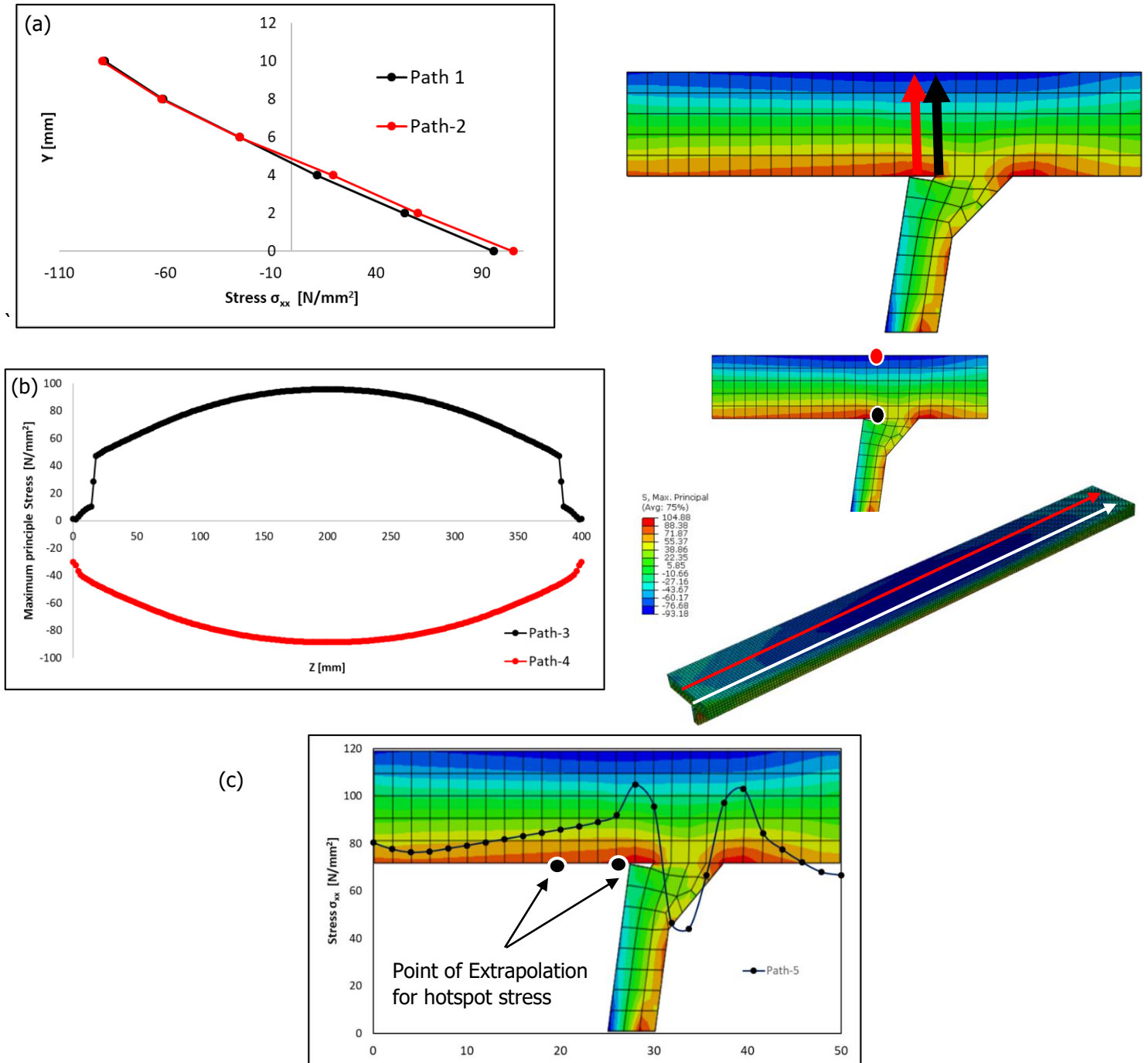
Figure 5.14 (a) Stress distribution along the thickness of the deck plate (b) Stress distribution at the weld root along the longitudinal direction (c) Stress distribution in the bottom part of the deck plate at the weld root (For wheel load = 45KN)

Note: All the output results presented in this section are obtained from the static load simulation for wheel load 45KN. Stress distribution mainly focusses at the weld root at the centre span between the cross-beams are obtained near the crack location.

Comparison with moving load

(a)
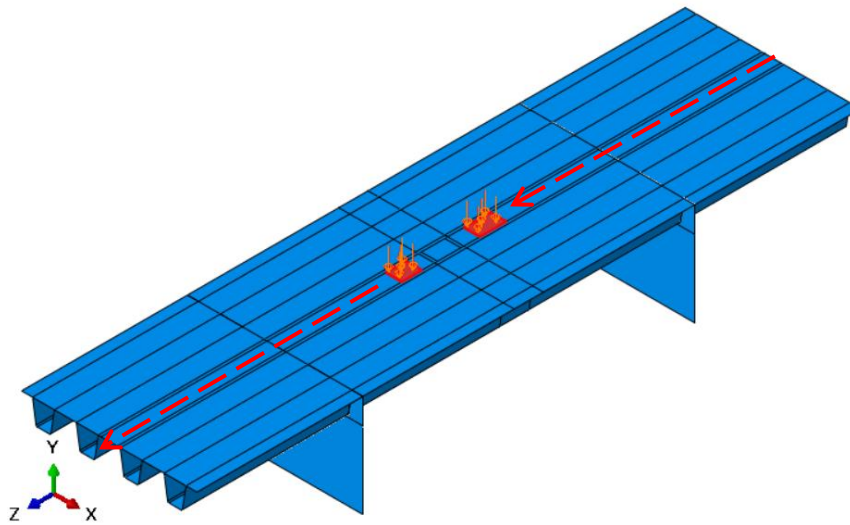
(b)
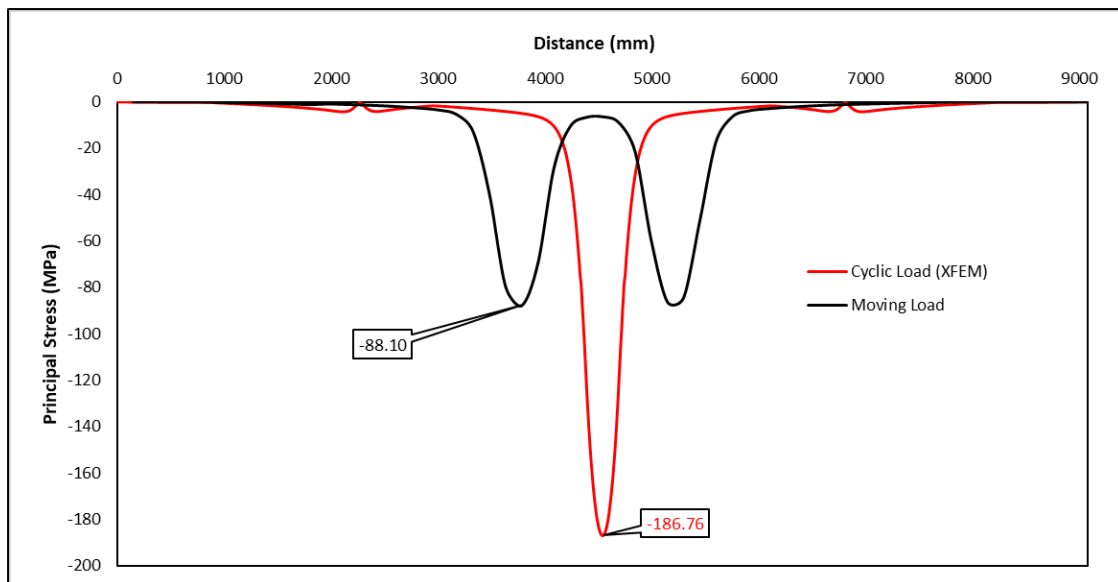
Figure 5.15 (a) Numerical model consisting of a moving load (b) Comparison of influence line between the cyclic load and moving load based on Max. Principal stresses

Since the numerical model consist of a single cyclic load acting at one position (centre), it is important to know the practical relevance by comparing with a moving vehicle. Therefore, the influence line based on cyclic load 45KN (for zero stress ratio) is been compared with a similar wheel load moving at speed of 100 km/hr. Figure 5.15 (b) depicts the comparison of principal stresses on the deck plate between the two scenarios. Firstly, it is clear that the most unfavourable case of position of load is at the centre (at 4540 mm) of the model. Secondly, the influence of load is localised, and it is mostly in region of 340 mm from the centre on either side for principal stress. From the comparison of peak principal stress, it has been observed that cyclic load produces 2.12 times higher than the vehicle moving with 100km/hr speed. It recommended to model the moving load in predict the crack propagation. Considering the computation effort require to model the moving load combined with XFEM calculation, this research is limited to a cyclic load acting at a single position and excludes other dynamics factors.

5.5 Fatigue crack initiation period

5.5.1 Fatigue detail category

The 'FAT' or detail category represents the fatigue stress range which gives the fatigue life at 2 million cycles. The shape of the fatigue strength S-N curves recommended in the IIW document for structural hotspot stress is similar to the direct nominal stress S-N curve consisting of a line with constant slope (m) of 3 when plotted in log-log graph. The fatigue limit is defined for stress range at 5 million load cycles below which the fatigue life is infinite for a constant amplitude loading.

This research focusses on the welded connection of the deck plate to the longitudinal stiffener at the span between the cross-beams. The welding detail is designed based on the available standards. According to the Eurocode 3 [41], a minimum weld penetration of 67%-75% should be achieved. Moreover, based on Kolstein research [43], a nominal value of penetration of 80% is suggested. Despite these recommended values, the manufacturer tries to achieve penetration as much as possible. Thereby, when the weld is executed with care, the fatigue strength increases. Therefore, the fatigue detail category for a single-sided fillet welded connection between the deck plate and longitudinal stiffeners differs.
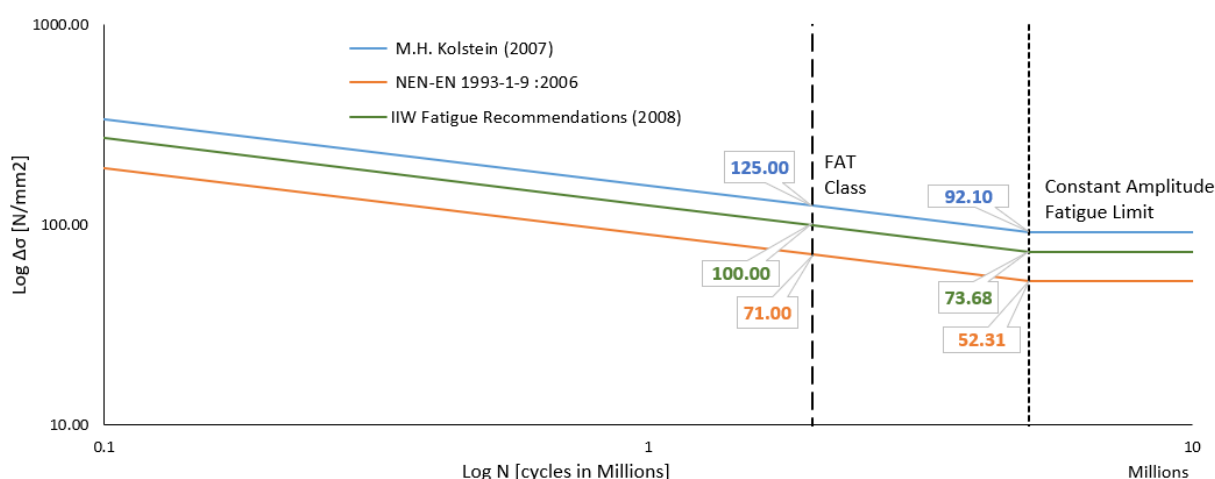
Figure 5.16 Fatigue strength curves for stiffener-to-deck plate connections

A reference value $\Delta\sigma_c$ of 71 MPa is defined in the Eurocode NEN-EN 1993-1-9 [27]. However, a recent fatigue test showed a reference value up to 140 MPa and proposed a detail category of 125 MPa for cracking in the deck plate [43]. Furthermore, Dutch national annex NEN-EN 1993-2+C1/NB recommended a value of 125 MPa for deck plate cracking originating from the weld root [44]. Moreover, IIW [30] recommends a FAT class 100 for this detail if the stresses are derived using hotspot method. For this research the fatigue life (crack initiation) prediction is carried out using hot-spot stress method. Therefore, a reference value of 100 MPa is adopted and the corresponding fatigue limit (CAFL) is evaluated as 73.68 MPa, ensuring no fatigue damage occurs below this stress range.

5.5.2 Hot spot stress method

The investigation of crack initiation at weld root is evaluated based on hot spot stress method. Firstly, the numerical model developed in this research is aimed to validate against the full-scale RWS existing numerical model. Mainly, the hotspot stress is compared with the hotspot stress obtained by the existing numerical model [42] developed by Rijkswaterstaat (RWS). The existing numerical model was developed on a full-scale (fixed part of the bridge) using beams elements in combination with shell elements (see Figure 5.17(a)) for recalculating the capacity of the existing bridges and to design strengthening schemes for fatigue and static strength. Particularly, for fatigue verification the RWS model consisted of one axle loading (type C axle of truck type 6) acting over 50 mm of hot asphalt (E=0.5 GPa) in local fatigue assessment (see Figure 5.17 (b)). However, the FEM-model developed in this research consist of a single wheel load (type C axle of truck type 6) acting over the deck plate.
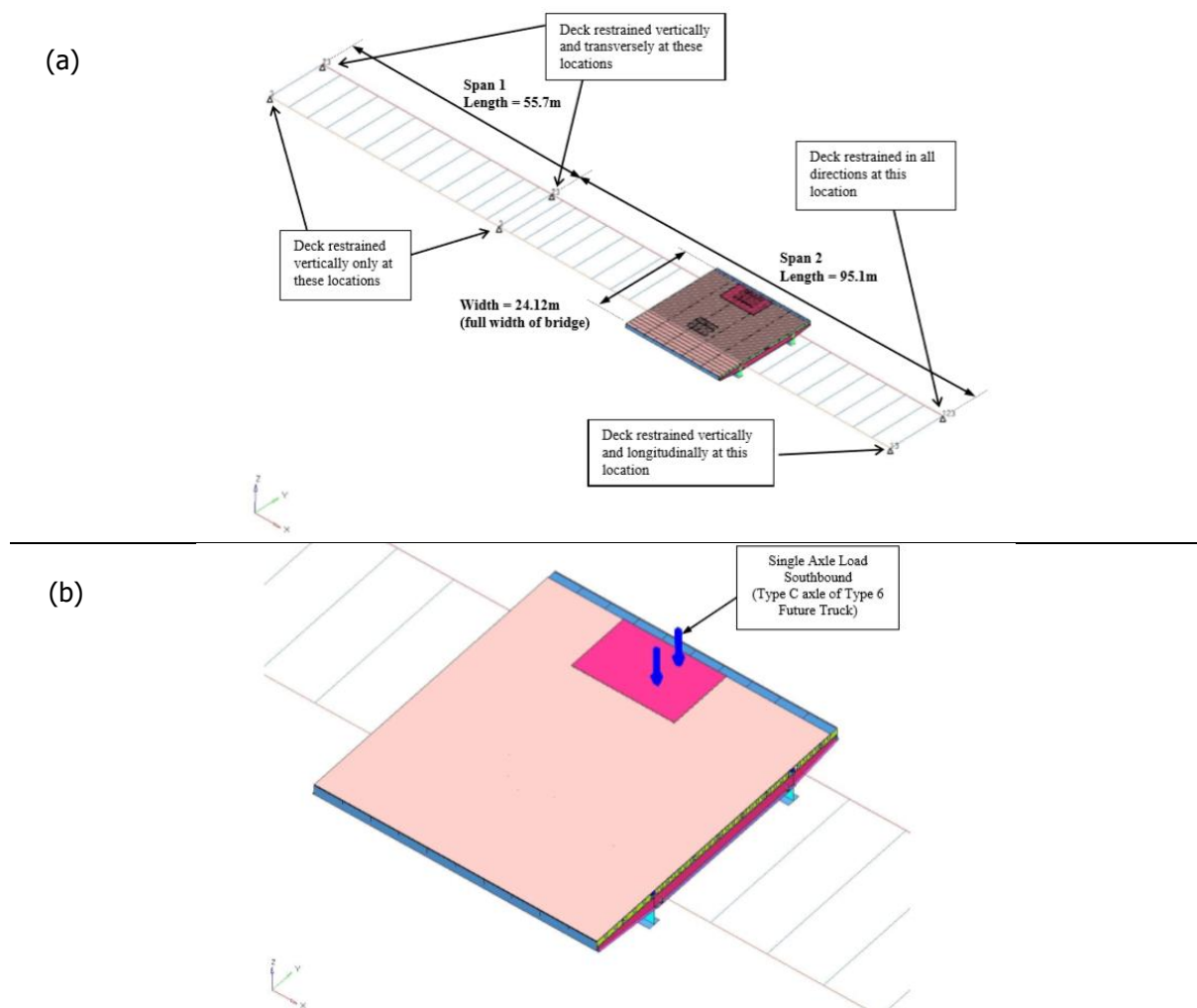
Figure 5.17 (a) Overview of the RWS numerical model (Fixed bridge) [42] (b) RWS Fatigue verification model under single-axle load C [42]

Figure 5.18 displays the output results of principal stress of both the models. Moreover, the comparison between the models is tabulated in Table 5.4.

FEM-model	RWS- Model
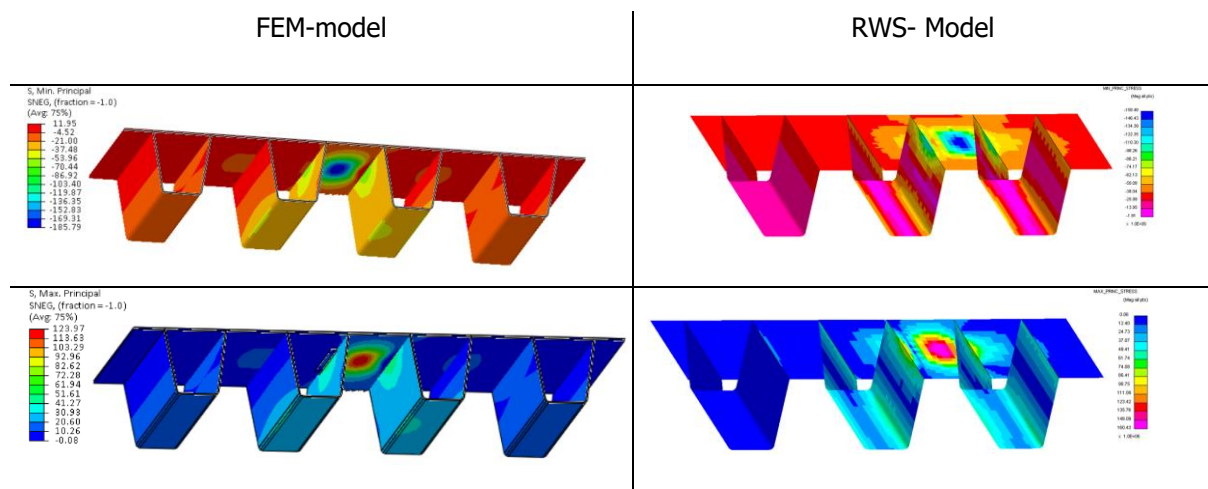
Figure 5.18 Comparison of max. and min. principal stresses of different model

From RWS model, the hotspot stress derived at the root of the weld was 109.08 MPa by extrapolating the stresses obtained at 5 mm (Point A) and 10 mm (Point B) away from the heel of the weld. On the other hand, the hotspot stress derived using a single wheel load (wheel print C) by extrapolating the stresses from 4mm and 10mm distance away from the weld root. The hotspot stress comes out to be to be 113.84 MPa, which is 4.3% higher than the existing model. The difference in the magnitude can be due to the dispersion of load from asphalt and difference in the points of extrapolation. Nevertheless, the XFEM numerical model showed a good correlation with the existing numerical model.

Table 5.4 Comparison of hotspot stresses (MPa) based on different models

Numerical model	Model Load (KN)	Max. Principal (MPa)	Min. Principal (MPa)	Max. Stress Point A (MPa)	Max. Stress Point B (MPa)	Hot spot Stress (MPa)
FEM-model	Wheel Load-52.5	123.9	-185.8	109.0	`101.8	113.84
RWS- Model	Axle Load-105	160.4	-158.5	108.0	104.3	109.08

After the validation of simulated results, the numerical model is used to determine the hot-spot stresses for different wheel loads with wheel print A throughout this research. It should be noted that the determination of stress range is highly sensitive to fatigue life estimation. With a twice increase in the stress range, the number of cycles can overestimate by 8 (2^3) times. Considering the importance of accuracy, the stress range is evaluated using shell and solid models.

According to NEN 8701, the wheel load (type A and type C) ranges from 21.25 KN to 45 KN for high traffic category. A comparison between their hotspot stress based on different approach for different wheel loads is tabulated in Table 5.5. It is noted that the variation of the hotspot stress between the solids and shell approach is constant (5.46 %) throughout from wheel load 21.25 KN to 45 KN. In solids, the geometry of weld is well defined and variation of stresses in through-thickness of the deck plate can be observed. This can be the possible reason between the difference of hotspot stresses in solids and shell model.

Table 5.5 Comparison of hotspot stresses (N/mm²) based on different approach

Model Approach	Wheel load - 45KN (Max.)	Wheel load - 21.25KN (Min.)
Solids Model	108.46	50.84
Shell Model	114.40	53.63

Further, hotspot stresses are derived using the solid model for several wheel loads and plotted against each other shown in Figure 5.19. Based on fatigue limit (see Figure 5.16), it is possible to segregate the wheel load which are not contributing to the fatigue damage. It was found that the wheel load more than 31 KN have an impact on fatigue life of the joint. With this analysis, the wheel load range is reduced to four types: 35KN, 40KN, 42.5KN and 45KN for further investigation.
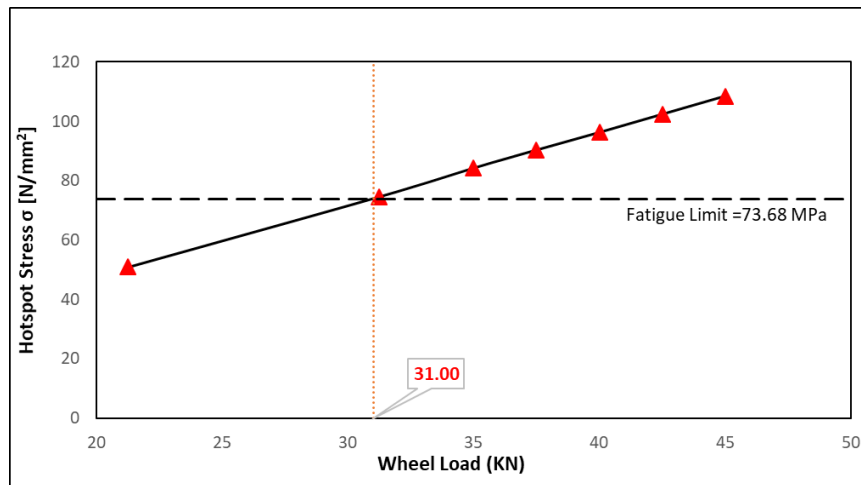
Figure 5.19 Hotspot stresses derived at the root of the wheel for various wheel loads

5.5.3 Fatigue Life prediction

It would be conservative to consider only the maximum load (45KN) to evaluate the fatigue life. The standard NEN8701 [40] provides the percentage of traffic based on the type of vehicle but does give a clear distribution of traffic based on wheel load. Since the hotspot is computed for a wheel load, therefore it was important to redefine the traffic distribution based on wheel load. Figure 5.20 represents the distribution of traffic based on wheel load for period 1972-2010.
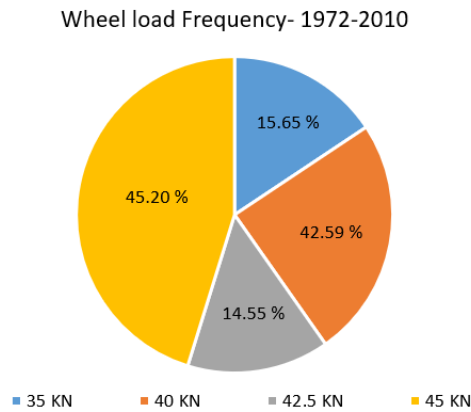
Figure 5.20 Wheel load frequency for 1972-2010 derived from the standard NEN 8701

It was found out that wheel load 45KN had maximum occurrence about 45.20 % and 42.5 KN being the least of about 14.55% for period 1972-2010.Taking the frequency of the wheel load in account, the fatigue life is evaluated using Palmgren-miner damage model (5.1).

$$D = \sum_{i=1}^{k} \frac{n_i}{N_i}$$
(5.1)

where k different stress level, N_i is the average number of cycles to failure, n_i is the number of cycles accumulated and D is damage fraction (when reaches 1, failure occurs).

The fatigue life is predicted to be 1.91 million load cycles which is equivalent to 20 years. In other words, it can be said that the fatigue crack initiated in the year 1992.

5.6 Fatigue crack propagation period

It is true that the accuracy of simulated fatigue crack propagation relies on various factors such as LEFM parameters, weld root conditions and most importantly the used traffic load. It is often assumed to consider the maximum axle load in predicting the fatigue crack propagation rate. However, this assumption is safe and reliable in accessing the extreme situation. Furthermore, this assumption can lead to underestimation of the remaining life of the structure. Thus, reducing the advantage of load-bearing capacity of OSD. Therefore, it is important to reduce the degree of conservative assumptions as much as possible and effectively utilise the capacity of numerical approach. Thereby, a range of wheel load is considered to predict the crack propagation period.

To predict the fatigue crack propagation period, numerical simulation can be performed in two ways using XFEM-model i.e. Stationary model and Propagating model. Stationary simulation refers to inserting certain number of crack fronts in the weld location and evaluating stress intensity factor. On the other hand, propagating simulation refers to evaluating the crack front using the full advantage of automated XFEM simulation. The procedure to predict the crack propagation period using stationary model is discussed briefly in this report but the final estimation to predict the crack propagation period is performed using propagating model.

5.6.1 Development of XFEM model

Although FE model with shell elements reflects the real behaviour of the structure, a more detail model is needed for studying the fracture crack growth behaviour. Therefore, the crack part was replaced with solid elements and LEFM based VCCT contact property was applied to it. While developing the XFEM model, certain assumptions were taken for numerical XFEM calculation. Firstly, the initial crack was assumed to be semi-elliptical of 1 mm half-length along both the major and minor axes. The selection of the initial crack flaw is extremely sensitive to the simulated results. The choice of the initial crack flaw often depends upon the welding detail, used manufacturing technologies and the lifetime of the structure. The initial crack length is generally selected between 0.1 to 1 mm [28]. Nowadays, the manufacturer tries to manage a higher degree of weld penetration during welding. Taking into the consideration of welding technology at the time of construction (1970s), the size of the initial crack is selected. Secondly, the fatigue crack is assumed to originate from the centre of the mid-span between the cross-beam. Therefore, the initial crack flaw was positioned at the weld root perpendicular to the deck plate. The implementation of the initial crack flaw is well illustrated in Figure 5.21.
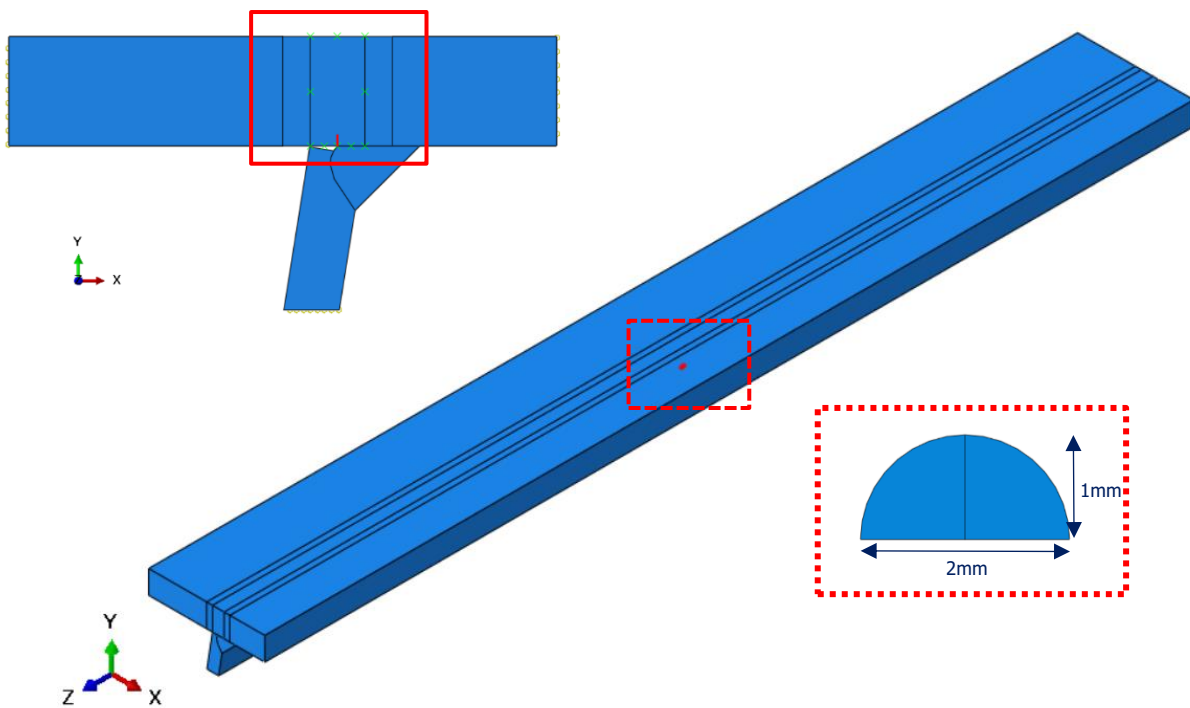
Figure 5.21 Location and definition of the initial elliptical shape

5.6.2 LEFM implementation

VCCT was used in the XFEM-based LEFM for crack propagation analysis using the direct cyclic approach with a time increment size of 0.05 per cycle. The direct cyclic load simulation is based on the periodic function (equation 2.12) and the parameter used for different wheel load is tabulated in Table 5.6. In this study, Power law mix-mode model is selected to determine the equivalent fracture energy release rate represented in the equation (2.15) because of its simplicity in the relation of different modes of fracture.

Table 5.6 Direct cyclic parameters

R_σ	Load (KN)	A_0	A_1	B_1	t_o	ω
0.00	40	0	0	1	0	2π
0.00	45	0	0	1	0	2π
0.00	50	0	0	1	0	2π
0.00	52.5	0	0	1	0	2π

5.6.3 Time-of-flight-diffraction (TOFD) measurement

On 8th October 2016, a semi-mechanized TOFD was conducted to inspect fatigue cracks in selected areas on the east side, direction of the Maasvlakte of the Suurhoff bridge. TOFD equipment consisted of two ultrasonic transducer which were positioned on either side of the weld between cross-beam no. 29 and 32. A crack length of 230 mm was measured at the west side of the trough no. 25 after the asphalt was removed. The crack originated from the weld root and was reached the surface of the deck plate. The placement of the ultrasonic transducer and corresponding TOFD data [45] can be found in Appendix E.

Table 5.7 Crack dimension obtained using TOFD method

Location	Start (mm)	Length (mm)	Depth (mm)	Height (mm)	Remarks
25 trough (West)	8460	230	0.0	10.0	Surface Breaking
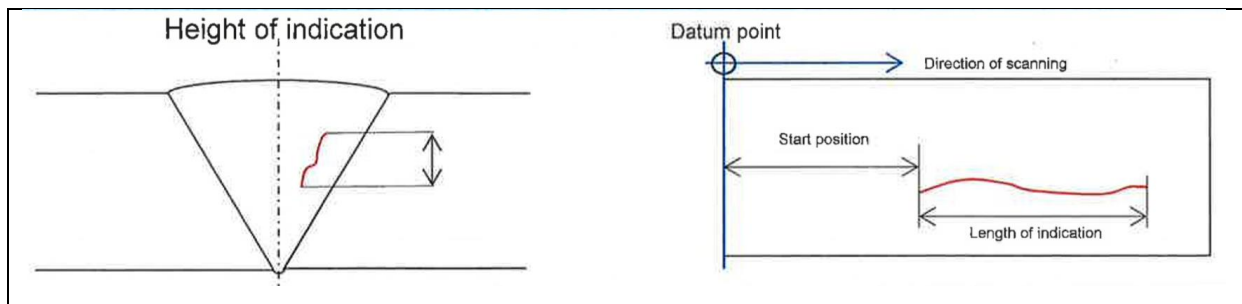
Figure 5.22 Representation of TOFD measurement [45]

5.6.4 Stationary model

From the TOFD measurement, the final dimension of the crack front can be obtained. Furthermore, the crack front can be divided into certain number of equal intervals (da) including the dimension of the initial crack flaw. In this way, the stress intensity factor at the tips of the various crack fronts can be computed. This parameter is most important in predicting the crack growth and its lifetime using the Paris Law equation (5.2).

$$\frac{da}{dN} = C.\Delta K_I^m \tag{5.2}$$

where C and m are the material parameters and ΔK_I represents the stress intensity factor range for mode I cracks. Paris law constant C and m are adopted from the literature as discussed previously. Knowing the stress intensity factor range for a different range of crack dimension (da), it is possible to compute the required number of cycles (N) using equation (5.3) manually.

$$N_f = \int_{a_i}^{a_f} \frac{da}{C.\Delta K_I^m} \tag{5.3}$$

Furthermore, geometrical dependent parameter f(a) can be evaluated from equation (5.4).

$$\Delta K_I = f(a).\Delta\sigma.\sqrt{\pi.a} \hspace{8cm} (5.4)$$

where $\Delta\sigma$ is the stress range at the crack front and a is the crack length. $f(a)$ is the geometrical parameters which not only depends upon the crack length a but also on the overall dimension of the bridge. However, computing geometrical factor $f(a)$ is beyond the scope of this research.

5.6.5 Propagating model

It is to be noted that the stationary model gives limited information of number of cycles (N) as it is derived only through stress intensity factor range for mode I fracture. However, in complex structures such as OSD model, mode II and mode III can have significant effect in crack propagation. Therefore, a second and more accurate method to evaluate the crack front including three modes of fracture using automated crack propagation simulation. This method utilises the full advantage of XFEM possibilities and even is able to determine the crack propagation path in a complex three-dimensional way. Although, it requires a high computational effort, this method has the potential to evaluate the weld geometry and its corresponding cracks. At the beginning, an initial crack is positioned in the model and material parameters of fracture is applied to it. Later, the XFEM-model uses the Paris law to simulate the crack propagation automatically. This simulation is carried out using fracture energy-based criterion which uses the least energy to crack.

The crack growth is characterized by the Paris law, which relates the relative fracture energy release rates to fatigue crack growth rate (Figure 2.11). These fatigue crack growth rates are evaluated based on assigned VCCT technique. The crack propagation appears when the energy available for the crack is high enough to overcome the fracture resistance of the material. Since ABAQUS® analyses the fracture by the Griffith energy criterion approach, the Paris law parameters C_3 and C_4 were calculated assuming plane stress situation see equation (2.8) and (2.14) listed in Table 5.8.

Table 5.8 Paris constants C_3 and C_4

	Literature Data		ABAQUS (XFEM)	
	C	**m**	**C_3**	**C_4**
Hobbacher (2015)	3.00×10^{-13}	3	28.87×10^{-6}	1.5

To ensure the start of crack growth process, material constants C_1 and C_2 were kept negligible as 0.001 and 0 respectively. Once the onset of the fatigue crack growth is satisfied (see equation 2.13), the crack propagation rate can be computed based on the fracture energy release rate (equation 2.14). The material fracture property was implemented using Power law mix-mode behaviour illustrated in Table 5.9.

Table 5.9 Critical energy release rate G_c

	Critical energy release rate Gc (Nmm^{-1})			Exponent		
	Mode I	**Mode II**	**Mode III**	**am**	**an**	**ao**
Numerical model	11.9	11.9	11.9	1	1	1

5.6.6 Output
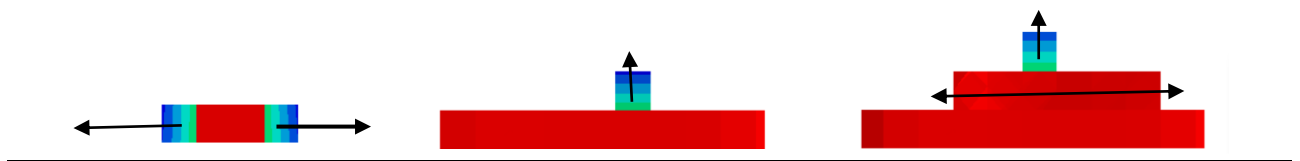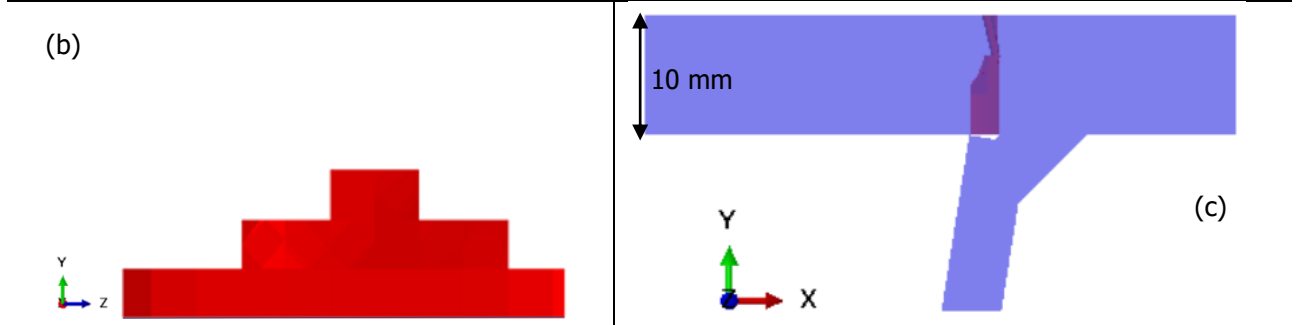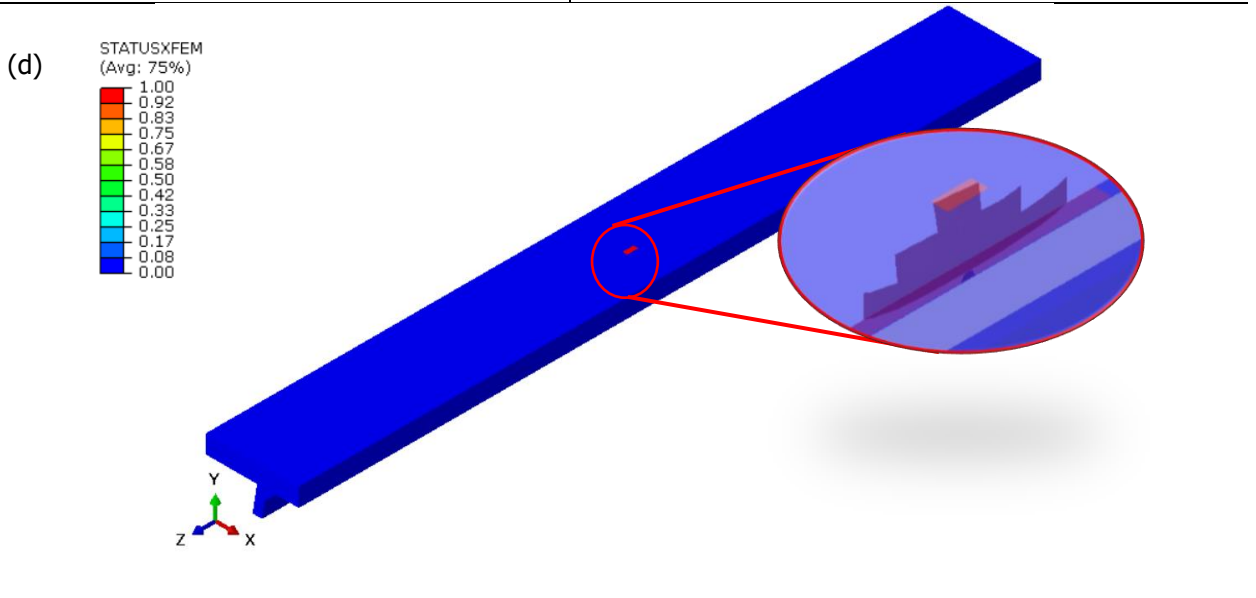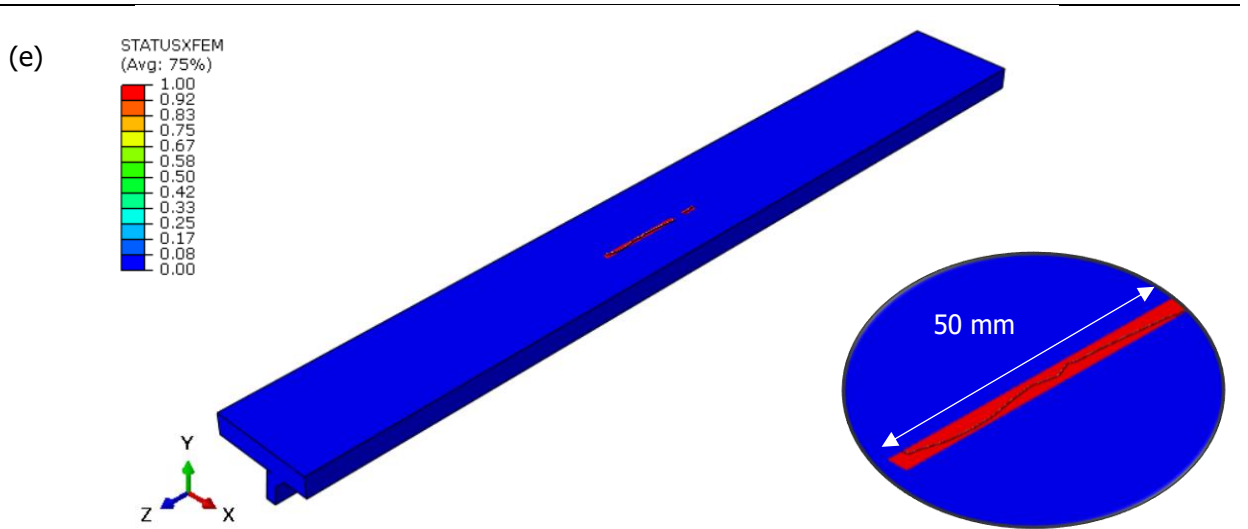
Figure 5.23 (a) Stages of crack propagation displayed as STATUSXFEM output variable (b) Crack propagation mechanism (c) Side view corresponds with the weld root (d) Isometric view of the crack on the surface of the deck plate (e) Deck plate crack length for wheel load 45 KN

5.6.7 Result and Discussion

Due to reversed loading, the weld root is affected by both tensile and compressive stress. However, it should be noted that compressive stresses have no effect on the crack propagation. As a result, all the negative SIF values are set to zero in LEFM. In the absence of residual stresses, the crack propagation is limited to half-thickness of the deck plate until where the tensile stress is present for zero stress ratio. As the crack front the neutral axis of the deck plate, the crack propagation stops. This is one of the main reasons behind the consideration of reverse load cycles. It is assumed that fatigue resistance becomes critical when the crack has propagated through the deck plate and reaches the surface. However, the fatigue crack growth will not immediately develop into the unstable stage. Nevertheless, immediate action is necessary to remedy this situation.

Although the crack propagation path is not the same, the crack propagation mechanism was similar for all the wheel loads (Table 5.6). The crack initiating from the weld root propagates in both longitudinal and vertical direction in the deck plate. However, the propagation rate in both directions was different. Firstly, the crack propagates in a longitudinal direction for a certain length until it starts propagating in a vertical direction. This process continues symmetrically until the crack reaches the deck plate surface forming an elliptical shape (see Figure 5.23 (b)). An example is presented in Figure 5.23 (a), for wheel load 35 KN where the crack length is 33 mm followed by 18mm in the next row. Despite the use of 8-noded brick hexagonal elements, the crack propagated in a semi-elliptical fashion. This is mainly due to the distribution of the stress intensity factor at the crack front. This trend holds for all the range of wheel loads considered in the simulation.

Using the XFEM model, the fatigue crack growth originating from the weld root and propagating into the deck plate thickness is studied in this section. The simulated results of crack growth in the through-thickness direction of the deck plate are plotted against the number of load cycles for various wheel loads as shown in Figure 5.24. The wheel load is adapted from the NEN 8701 for the period (2011-2040) ranging between 40 KN and 52.5 KN.
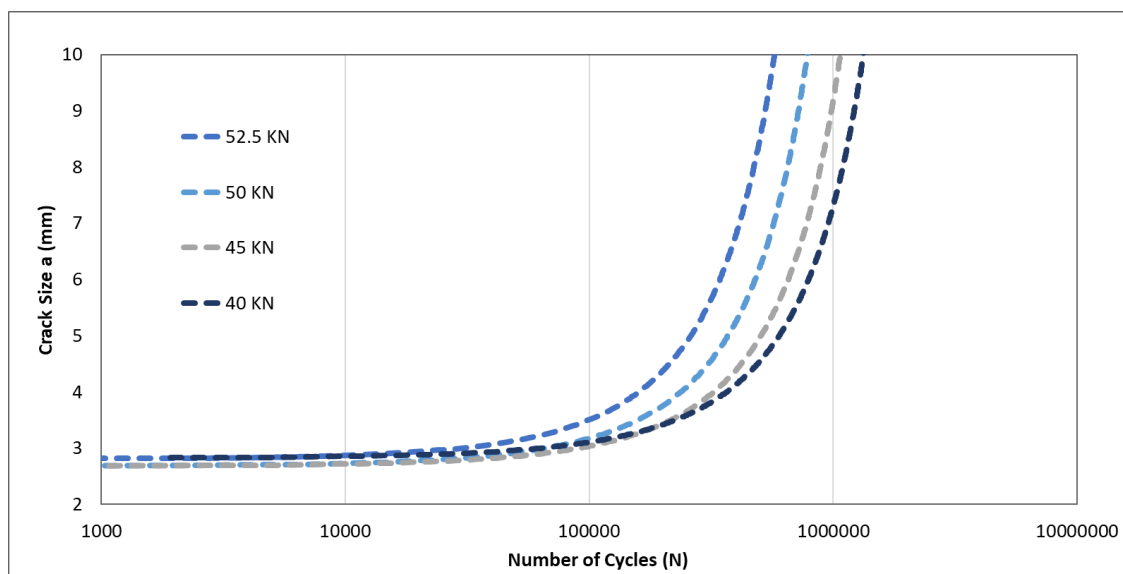
Figure 5.24 Fatigue crack growth for several wheel loads in through-thickness direction

From Figure 5.24, exponential crack growth is observed. The rate of crack propagation in through-thickness increases with an increase in the wheel load. Moreover, the variation in the growth is observed after 100,000 cycles, especially for wheel load 52.5KN. For every 12.5 % increase in wheel load from 40KN to 52.5KN, the decrease in the cycles to the critical stage (the fatigue crack reaches to the surface of the deck) is not constant. It is clear from the graph, as the load decrease, the difference in the cycles to a critical stage decrease. For instance, the difference in the cycles for wheel load 52.5KN and 50KN is about 24% whereas the difference diminishes to 10% in the case between wheel load 40KN and 42.5KN. This difference is mainly governed by bending stresses caused by the wheel load and corresponding variation of the stress intensity factor at the crack front. As a result, the crack propagation path varies. From the Paris law, it is clear that with a slight change in the stress intensity factor, the rate of the propagation drastically increases which can be the possible explanation for the degree of variation.
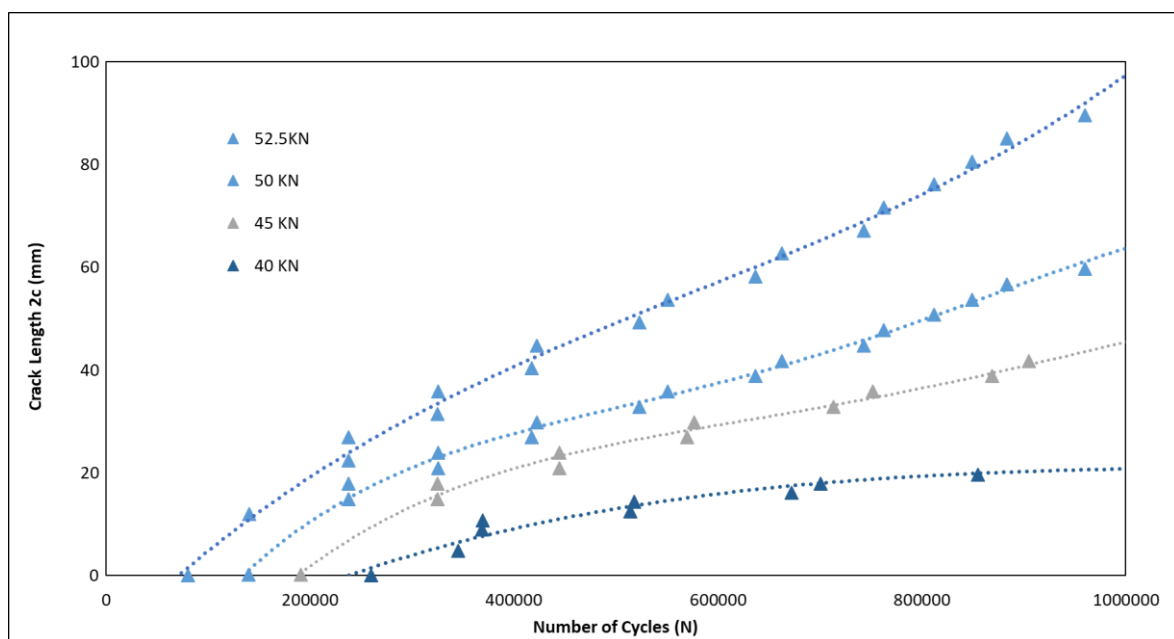
Figure 5.25 Fatigue crack propagation in the surface of the deck plate

Once the crack touches the surface of the deck plate, the crack seems to be arrested. The possible explanation can be the absence of SIF at the crack front in the top side. As a result, the crack propagation shifts in the longitudinal direction. An example of crack propagation in the deck plate for wheel load 45 KN at 1.1 million cycles is illustrated in Figure 5.23(d) for a crack length of 50 mm. Figure 5.25 displays the curves of crack propagation in the surface of the deck plate for various wheel loads. At this moment, it was not possible to simulate the crack until a crack length is found like the Suurhoff bridge of 230 mm due to convergence problem in the simulation. However, if an exponential extrapolation function is used based on the simulated crack lengths, it is possible to predict the number of load cycles required to reach a crack length of 230 mm. Moreover, the prediction of the number of load cycles will depend upon the wheel load considered.
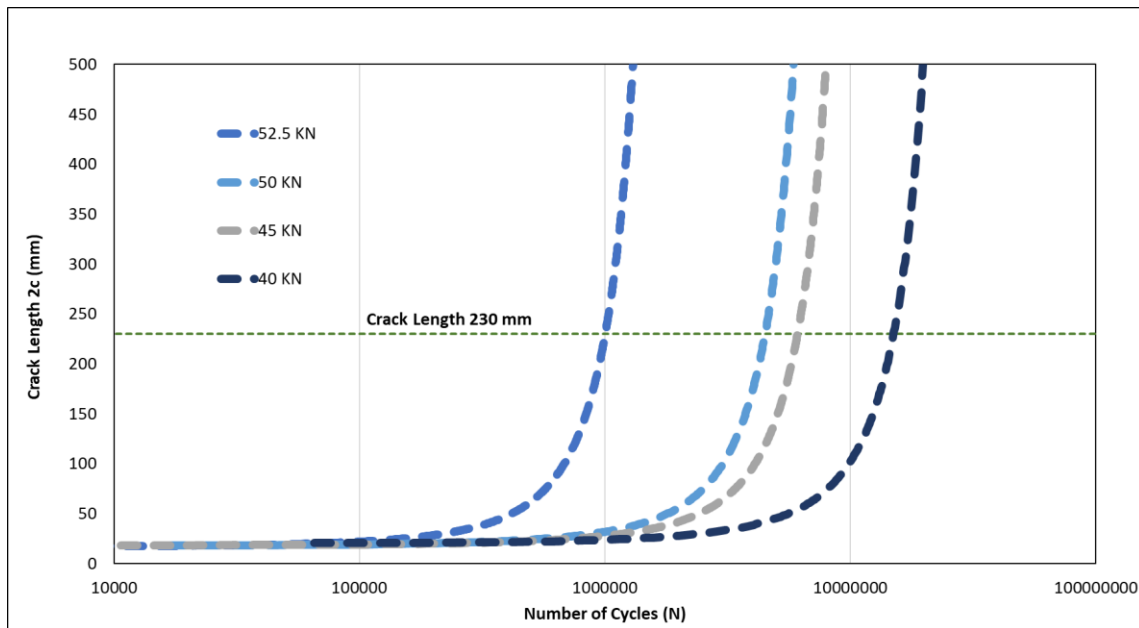
Figure 5.26 Fatigue crack propagation in a longitudinal direction on the deck plate surface

Figure 5.26 displays the exponential extrapolated curves of crack propagation in the surface of the deck plate for various wheel loads. From the graph, the number of load cycles requires to reach a crack length of 230 mm is predicted in the range between 0.99 and 15.03 million load cycles for wheel load 52.5 KN and 40 KN respectively. In order to predict a reliable value from the range, the traffic distribution (period 2011-2040) based on frequency of wheel load is considered. Since the frequency of the wheel load 45KN is 49.3% (maximum) to the total distribution of traffic (Figure 5.27) wheel load 45KN will be used for prediction.
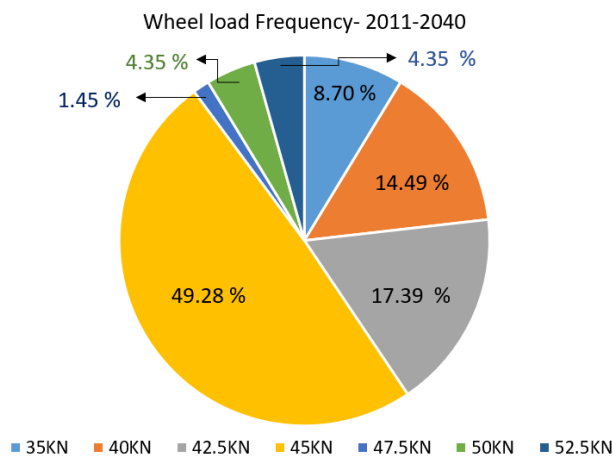
Figure 5.27 Wheel load frequency for 2011-2040 derived from the standard NEN 8701

Therefore, if an exponential extrapolation is made for the wheel load 45KN, the crack will reach a length of 230mm after 5.95 million load cycles. Whereas, in reality, it just requires 4.75 million load cycles after the crack initiation. The XFEM model predicted more than the required number of cycles due to

multiple reasons. It must be remembered that the model does not include residual stresses and initial imperfection. The initial imperfection can significantly influence the fatigue life. However, the residual stresses effect may either be beneficial or detrimental, depending on their magnitude of compression or tension and distribution in the connection. The effect of residual stresses is expected to be high as a large amount of weld is concentrated at one location. Moreover, the welds are not chamfered at the surface to reduce the effect of residual stresses. On the other hand, the weld material is homogenous (without any defects) in the XFEM model. This can be a possible explanation for this overestimation. Nevertheless, this numerical model showed a good correlation with the real scenario. Furthermore, this numerical model is used in predicting the permissible limit of deck plate cracks length for 500 mm. If an exponential extrapolation is made to a crack length of 500 mm for the wheel load 45KN, the number of load cycles comes out to be 8.02 million load cycles. In other words, it will take 34 years more after the crack initiation to reach a deck plate crack length of 500mm. This information helps to determine the renovation and inspection interval.

5.7 Combined fatigue assessment

With the help of the numerical model, it was possible to determine the total fatigue life of the bridge. The determination of crack initiation period and crack propagation period were derived independently. The fatigue life was determined based on SN-curves and the hypothesis of Palmgren-Miner. Whereas the fracture assessment was carried out using automated XFEM simulation. Since the numerical model consisted of a single wheel load it was important to redefine the traffic distribution based on wheel load. Thereby, the total fatigue assessment was estimated taking into account the frequency distribution of the wheel load for given three periods (1972-1990, 1991-2010, 2011-2040) as per prescribed in NEN8701. Moreover, based on the fatigue limit, the wheel loads were categorised.

Based on the hotspot stress method, the crack initiation period is predicted to be 1.91 million load cycles which is equivalent to 20 years. In other words, it can be said that the fatigue crack initiated in the year 1992. In continuation to that, automated crack propagation resulted in 5.95 million load cycles to reach a crack length of 230 mm in the deck plate surface. So, if both the periods are combined, the numerical model predicts the total fatigue life to be 7.86 million load cycles which is equivalent to 48 years for the crack length of 230 mm. However, in reality, a similar crack length was detected after a service life of 44 years. Although a bit optimistic, the numerical model showed good agreement with the TOFD measurement. Furthermore, the numerical model predicted 8.02 million load cycles for a deck plate crack length of 500 mm which is equivalent to 34 years after the crack initiation period. Therefore, the total fatigue life for deck plate crack length of 500 mm is predicted to be 54 years. Nevertheless, the fracture mechanics approach showed a sign of improvement of the fatigue life assessment.
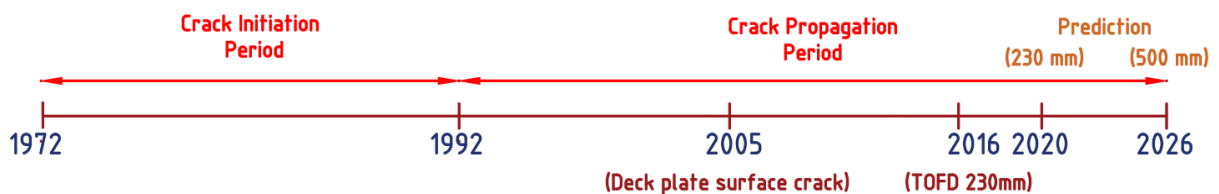

Figure 5.28 Summary of fatigue life estimation

Chapter 6

CONCLUSIONS AND RECOMMENDATIONS

6.1 Conclusions

The implementation of LEFM as a fatigue assessment tool showed promising results for assessing fatigue cracks, particularly when combined with the XFEM-model in ABAQUS®. A detailed 3D-visualization of crack propagation could be observed. In addition to that, some explicit information such as SIF for every crack tip/front is available, which were helpful to determine other fracture parameters easily. The results of these parameter (SIF) is investigated in CT-Specimen and found be to in good agreement with the standard formulation, which signifies the reliability of this tool. However, some limitations were encountered during this research. The determination of SIF around the crack front in the presence of tetrahedral elements was not possible based on the contour-integral method. Moreover, the crack propagation based on LEFM does not affect the compression zone. Also, ABAQUS® does not provide a clear indication of the choice of mix-mode behaviour to evaluate the equivalent fracture energy release rate. Nevertheless, the automated crack simulation based on Paris law showed good correlation with the test result and turns out to be conservative mainly because of its simplistic nature. One of the important assumptions which still need to investigate is the choice of initial crack size and shape. The size of the initial crack flaw is extremely sensitive to fatigue crack simulation result in XFEM. A slight change in the dimension can shift the result from being unsafe to being conservative. To evaluate the modelling efficiency, the Paris constant should be preferably verified with the test result. Since the material test result of OSD specimen was not available, the constant was thus compared with the standard and proved to be indeed less conservative. Furthermore, threshold SIF should be considered in the formulation to improve the accuracy of Paris Law.

The main objective of the research was to numerically model and verify the problem of fatigue crack propagation using XFEM-model based on LEFM and VCCT. Based on the set of simulation executed, the conclusion of each model and corresponding answers to the research questions can be stated as follows:

1.1.   How to implement the material parameters and formulate Paris law in the XFEM model for numerical simulation of fatigue crack propagation?

The Paris law implementation in ABAQUS® for constant C_3 and C_4 were computed corresponding to the material constant C and m from the following relationship between strain energy release rate and stress intensity factor: $C_4=m/2$ and $C_3=C.E*^{C_4}$ where $E*=E$ for plane stress condition and $E*=E/(1-u^2)$ for plane strain condition.

2.1.   What is the accuracy of XFEM model developed in this research to predict the fatigue crack propagation rate in CT-specimen for different stress ratios?

- The fatigue crack propagation rate in 2D CT-specimen was predicted based on assumed VCCT fracture property using XFEM-model. The simulated crack propagation rate was validated against the test results with a maximum difference of 0.03% in the slope (m) and 1.48% in the intercept (C) of the power law equation.

- The simulated result of 2D-XFEM model was able to explain the crack closure mechanism

through the similarity principle for several stress ratios. Moreover, the simulated result showed good agreement with Elber's equation $U = 0.5 + 0.4R$, the relationship between the effective stress intensity factor ratio (U) and stress ratio (R).

- The crack propagation mechanism in 3D-XFEM is studied for various mesh sizes and it was found that the crack propagation starts from the centre of the thickness and propagates towards the edge of thickness for every crack length increment. This is mainly due to the stress intensity distribution along the crack front.

- The fatigue crack growth in 3D-XFEM model showed a good correlation with 2D-XFEM until a crack size of 17.8 mm with a maximum difference of 13.8% for stress ratio R=0.50. This difference is mainly due to the assumed straight crack front and corresponding non-uniform stress intensity factor distribution along the crack front in through-thickness direction.

- The stress intensity factor distribution is not constant along the crack front i.e. maximum in the middle and minimum at the edges. Based on the investigation, it was found out that SIF at the edges can be a reliable technique in predicting SIF when compared with the ISO 12108 formulation for SIF for a maximum difference of 1.16 %.

- From crack simulation of 3D-XFEM, a regular propagation mechanism is been observed up to a crack size of 17.8 mm until the crack encounter the top-face of the element. Based on the results up to 17.8 mm, 3D-XFEM- model were roughly in good agreements with the test results in predicting the crack propagation rate for a maximum difference of 25.23% in the slope of the power law equation.

2.2.   How to predict the Paris law constants (C and m) using XFEM-model based on the beach mark measurement?

- The fatigue crack growth was predicted based on assumed VCCT material property using XFEM-model. The simulated results of fatigue crack originating from the weld toe in the deck and propagating to the surface were correlated with the beach mark measurement obtained from the fatigue test. The calibrated Paris law constants C comes out to be 55 % lower when compared with the recommended value in IIW standards.

- In ensuring the actual behaviour of the test specimen, static analyses were performed. It was noticed the simulated vertical deformation overestimated with a maximum difference of 18 % at 40 KN when compared to the test measurement. This difference can be possible when the hydraulic jack setup is slightly inclined. Furthermore, the simulated strain results showed a good correlation with the test results along the longitudinal direction for the respective plates (deck plate and stiffener). It was observed that the peak appears at one-quarter of the specimen in both cases which can be due to the distribution of line load. Lastly, the method of determining the hot-spot stress showed its reliability as the numerical results were in good agreement with the test data.

2.3.   What is the total fatigue life (crack initiation period and crack propagation period) of the Suurhoff bridge (existing bridge) based on numerical analyses?

- In ensuring adequate behaviour of assumed boundary conditions, the numerical model is thus compared with a full-scale RWS existing numerical bridge model. Based on similar wheel load, the results of numerical model showed a good correlation in determining the stresses at the weld root using hotspot stress method with a difference of 4.3%.

- The total fatigue life of the bridge was predicted based on an assumed material property using a numerical model (FE and XFEM). The determination of crack initiation period and crack propagation period were derived independently. The crack initiation period was predicted to be 1.91 million load cycles which is equivalent to 20 years based on SN-curves and the hypothesis of Palmgren-Miner. Whereas the crack propagation period was predicted to be 5.95 million load cycles using automated XFEM simulation for a crack length of 230 mm.

- The numerical model predicted a total fatigue life to be 7.86 million load cycles which is equivalent to 48 years for the crack length of 230 mm. However, in reality, a similar crack length was detected after a service life of 44 years. This can be possible as residual stresses; weld defects were not implemented in the XFEM model. Nevertheless, the fracture mechanics approach showed a sign of improvement of the fatigue life assessment.

- Finally, the numerical model predicted a total service life of 54 years for a deck plate crack length of 500 mm.

6.2 Recommendations for future studies

6.2.1 CT-Specimen

Although 2D-XFEM model were in good agreements with the test result, it is to be noted that the crack propagation rate is depended on the thickness of the specimen. Based on three samples out of seven given samples of different thicknesses, it is difficult to conclude. Therefore, a parametric study is recommended to study the thickness effect on crack propagation rate.

It is advised to model the crack propagation, by placing the crack tip/front in the middle of element to obtain regular crack growth. Furthermore, a straight crack front is been assumed in this research which leads to non-uniform distribution of stress-intensity factor along the crack front. It would be interesting to investigate the shape of curved crack front, which can lead to uniform distribution of SIF. Based on the investigation on different crack profile such as elliptical, polynomial mathematical function, it was found 4th order polynomial returns a constant energy release rate value along the thickness [46].

The effect of boundary conditions caused a detrimental effect in crack propagation path as observed in this research for 3D-XFEM model. It is recommended to use a semi-circular section (separate part) attached to the respectively holes of the CT-specimen in applying loading/boundary conditions. Furthermore, the material parameters and through-thickness effect based on three-dimensional model needs to be further investigated to obtain comparable results with the test data till the final failure of the model.

6.2.2 OSD- Specimen

It should be remembered that a constant material property was assigned to the OSD model. However, it is to be noted that the fatigue crack propagation rate is different for the base material, welds and HAZ zones and thereby Paris law constants can differ at such location. Furthermore, the effect of residual stresses and microstructure change can be implemented in the XFEM-model. This can be a possible investigation in the future in predicting more accurate results.

Furthermore, the imperfection in implementation of line-load causes a non-uniform distribution of load over the surface, which can be further improved. In addition to that, contact property such as friction should be implemented. Consequently, the marginal error observed in FE analyses can be resolved. It is possible to predict the material parameter (Paris constant C and m) through XFEM simulation. However, to determine the modelling efficiency, the predicted material constant should be compared with the test sample.

6.2.3 Suurhoff Bridge

It is well known that material parameters fracture toughness K_{IC} and Paris constants (C and m) determines the quality of the fatigue life and are used in describing the crack propagation. These parameters should be determined based on the material test before implementing in the model. Furthermore, the application of loading (cyclic) resulted in 2.1 times higher stresses compared to a

moving vehicle of similar wheel load which is quite significant. Moreover, the magnitude of load should be calculated depending upon on location in the bridge lane preferably based on probabilistic approach.

References

1. Xin, H. and M.J.E.F.M. Veljkovic, *Fatigue crack initiation prediction using phantom nodes-based extended finite element method for S355 and S690 steel grades.* 2019. **214**: p. 164-176.
2. Kolstein, M.H., *Fatigue classification of welded joints in orthotropic steel bridge decks*. 2007.
3. Nagy, W., H. De Backer, and P. Bogaert, *Crack propagation in a stiffener-to-deckplate connection of an orthotropic steel bridge deck*. 2012. 1-8.
4. *D. Simulia "ABAQUS v6.14 - Documentation" ABAQUS*.
5. Griffith, A.A., *The phenomena of rupture and flow in solids.* Philosophical Transactions of the Royal Society of London, A, 221 (582–593), 1921: p. 163-198.
6. Erdogan, E., *Fracture Mechanics.* International Journal of Solids and Structures, 37, 2000: p. pp. 171-183.
7. *Stress Intensity Factors of Cracks*, in *Fatigue of Structures and Materials*, J. Schijve, Editor. 2009, Springer Netherlands: Dordrecht. p. 105-140.
8. *Fatigue Crack Growth. Analysis and Prediction*, in *Fatigue of Structures and Materials*, J. Schijve, Editor. 2001, Springer Netherlands: Dordrecht. p. 174-214.
9. *Fatigue as a Phenomenon in the Material*, in *Fatigue of Structures and Materials*, J. Schijve, Editor. 2009, Springer Netherlands: Dordrecht. p. 13-58.
10. Hellen, T., *How to undertake fracture mechanics analysis with finite elements*. 2001: NAFEMS.
11. Paris, P. and F. Erdogan, *A Critical Analysis of Crack Propagation Laws.* Journal of Basic Engineering, 1963. **85**(4): p. 528-533.
12. Zerbst, U., M. Madia, and D. Hellmann, *An analytical fracture mechanics model for estimation of S–N curves of metallic alloys containing large second phase particles.* Engineering Fracture Mechanics, 2012. **82**: p. 115-134.
13. Cui, C., et al., *Strain energy-based fatigue life evaluation of deck-to-rib welded joints in OSD considering combined effects of stochastic traffic load and welded residual stress.* 2017. **23**(2): p. 04017127.
14. Qian, Z.H. and D. Abruzzese, *Fatigue failure of welded connections at orthotropic bridges*. Vol. 9. 2009.
15. Nagy, W., H. De Backer, and P. Bogaert, *Fracture mechanics as an improvement of fatigue life assessment in orthotropic bridge decks*. 2013. 211-212.
16. Nagy, W., P. van Bogaert, and H. de Backer, *LEFM Based Fatigue Design for Welded Connections in Orthotropic Steel Bridge Decks.* Procedia Engineering, 2015. **133**: p. 758-769.
17. Ju, X., S.-M. Choi, and K. Tateishi, *Analytical Study on Crack Propagation at Rib-to-Deck Welded Joints in Orthotropic Steel Decks.* Kou kouzou rombunshuu, 2012. **19**(73): p. 73_85-73_94.
18. Belytschko, T. and T. Black, *Elastic crack growth in finite elements with minimal remeshing.* International Journal for Numerical Methods in Engineering, 1999. **45**(5): p. 601-620.
19. Melenk, J.M. and I. Babuška, *The partition of unity finite element method: Basic theory and applications.* Computer Methods in Applied Mechanics and Engineering, 1996. **139**(1): p. 289-314.
20. Cihal, V.J.K.M., *Corrosion of Metals and Alloys--Stress Corrosion Testing. II. Recommendations for Making Bent-Beam Specimens.* 1986. **24**(4): p. 389-398.
21. Standard, A.J.S.T.M.f.M.o.F.C.G.R., *E647-00.* 2000. **100**.
22. , A.M.P.d.J., et al., *A comparison of the fatigue behavior between S355 and S690 steel grades.* A comparison of the fatigue behavior between S355 and S690 steel grades, 2012: p. 140-150.
23. Bozkurt, F. and E. Schmidová, *Fracture Toughness Evaluation of S355 Steel Using Circumferentially Notched Round Bars*. 2018.
24. Elber, W., *The significance of fatigue crack closure*, in *Damage tolerance in aircraft structures*. 1971, ASTM International.

25.   Nagy, W., *Fatigue assessment of orthotropic steel decks based on fracture mechanics*, in *Faculty of Engineering and Architecture*. 2017, Ghent University: Ghent.

26.   Bignonnet, A., Carracilli, J. & Jacob, B. , *´ETUDE en FATIGUE des PONTS M´ETALLIQUES par un MOD`ELE de M´ECANIQUE de la RUPTURE*. 1991. p. 57–96.

27.   EN, B.J.B.S.I., London, *1-9 (2005): Design of Steel Structures. Part 1.9: Fatigue.* 1993.

28.   De Backer, H., *Optimalisatie van het vermoeiingsgedrag van het orthotrope brugdekconcept door verbeterde dispersie van de verkeersbelasting (in Dutch)*. 2006, Ghent University: Ghent, Belgium.

29.   Rippling, E. and P.J.U.D.o.T. Crosley, Federal Highway Admin, *Narrative summary on fracture control in relation to bridge design.* 1983.

30.   Hobbacher, *Recomendations for Fatigue Design of Welded Joints and Components*. 2015.

31.   Menzemer, J.W.F.C.C., *FATIGUE CRACKING IN WELDED STEEL BRIDGES*, ed. T.R. Board. 1990.

32.   Xiao, Z.-G., et al., *Stress analyses and fatigue evaluation of rib-to-deck joints in steel orthotropic decks.* 2008. **30**(8): p. 1387-1397.

33.   *Technische Specificatie (Reparaties orthotrope rijdekken met trogprofielen)*. 2017, Rijkswaterstaat Grote Projecten en Onderhoud p. 57.

34.   Kuhn, B., et al., *Assessment of existing steel structures: Recommendations for estimation of remaining fatigue life.* 2008. **1**: p. 1-90.

35.   Standard, B.J.G.t.M.f.A.t.A.o.F.i.M.S., " London, UK, *BS 7910: 2005,".* 2007.

36.   Maljaars, J., F. van Dooren, and H.J.S.C. Kolstein, *Fatigue assessment for deck plates in orthotropic bridge decks.* 2012. **5**(2): p. 93-100.

37.   Bignonnet, A., J. Carracilli, and B. Jacob. *ÉTUDE en FATIGUE des PONTS MÉTALLIQUES par un MODÈLE de MÉCANIQUE de la RUPTURE*. in *ANNALES DE L'INSTITUT TECHNIQUE DU BATIMENT ET DES TRAVAUX PUBLICS*. 1991.

38.   Hobbacher, A., *Recommendations for fatigue design of welded joints and components*. 2015: Springer.

39.   Nagy, W., et al., *Development of a fatigue experiment for the stiffener-to-deck plate connection in Orthotropic Steel Decks.* 2017. **17**(4): p. 1353-1364.

40.   8701, N., *Asessment of exisiting structures in case of reconstruction and disapproval- Actions*. December 2011.

41.   Eurocode, C.J.B., Belgium: Comité Européen de Normalisation, *1: Actions on structures-Part 2: Traffic loads on bridges, NEN-EN 1991-2: 2003.* 2003: p. 168.

42.   Bruggen, M.R., *Suurhoffbrug Phase 2 Technical Assessment Report* 2013: Utrecht, Netherlands.

43.   Kolstein, M.H., *Fatigue classification of welded joints in orthotropic steel bridge decks.* 2007.

44.   *NEN-EN 1993-1-9+C2 Eurocode 3: Design of steel structures - Part 1-9: Fatigue* 2009.

45.   Buyck, V., *Renovatie Suurhoffbrug- TOFD*, in *OPLEVERDOSSIER*. 2016.

46.   Roger, J., et al., *Three-Dimensional Simulation of Fatigue Crack Growth Considering Through-Thickness Effects in Epoxy Resins*. 2007.

Appendix

A. Paris law formulation

Table A.8.1 Keyword: Paris law formulation implemented for CT-specimen in XFEM-model

R=0.0	*FRACTURE CRITERION, TYPE=fatigue, MIXED MODE BEHAVIOR=POWER, TOLERANCE=0.001 0.001,0,7.84199E-06,1.7811,0,0.85,6.5,6.5 6.5,1,1,1
R=0.25	*FRACTURE CRITERION, TYPE=fatigue, MIXED MODE BEHAVIOR=POWER, TOLERANCE=0.001 0.001,0,19.80264E-06,1.85795,0,0.85,6.5,6.5 6.5,1,1,1
R=0.50	*FRACTURE CRITERION, TYPE=fatigue, MIXED MODE BEHAVIOR=POWER, TOLERANCE=0.001 0.001,0,18.7685E-06,1.94535,0,0.85,6.5,6.5 6.5,1,1,1

Table A.8.2 Keyword: Paris law formulation implemented for OSD-specimen in XFEM-model

R=0.0	*FRACTURE CRITERION, TYPE=fatigue, MIXED MODE BEHAVIOR=POWER, TOLERANCE=0.001 0.001,0, 12.99E-06,1.5,0,0.85,11.9, 11.9 11.9,1,1,1

Table A.8.3 Keyword: Paris law formulation implemented for Suurhoff bridge in numerical model

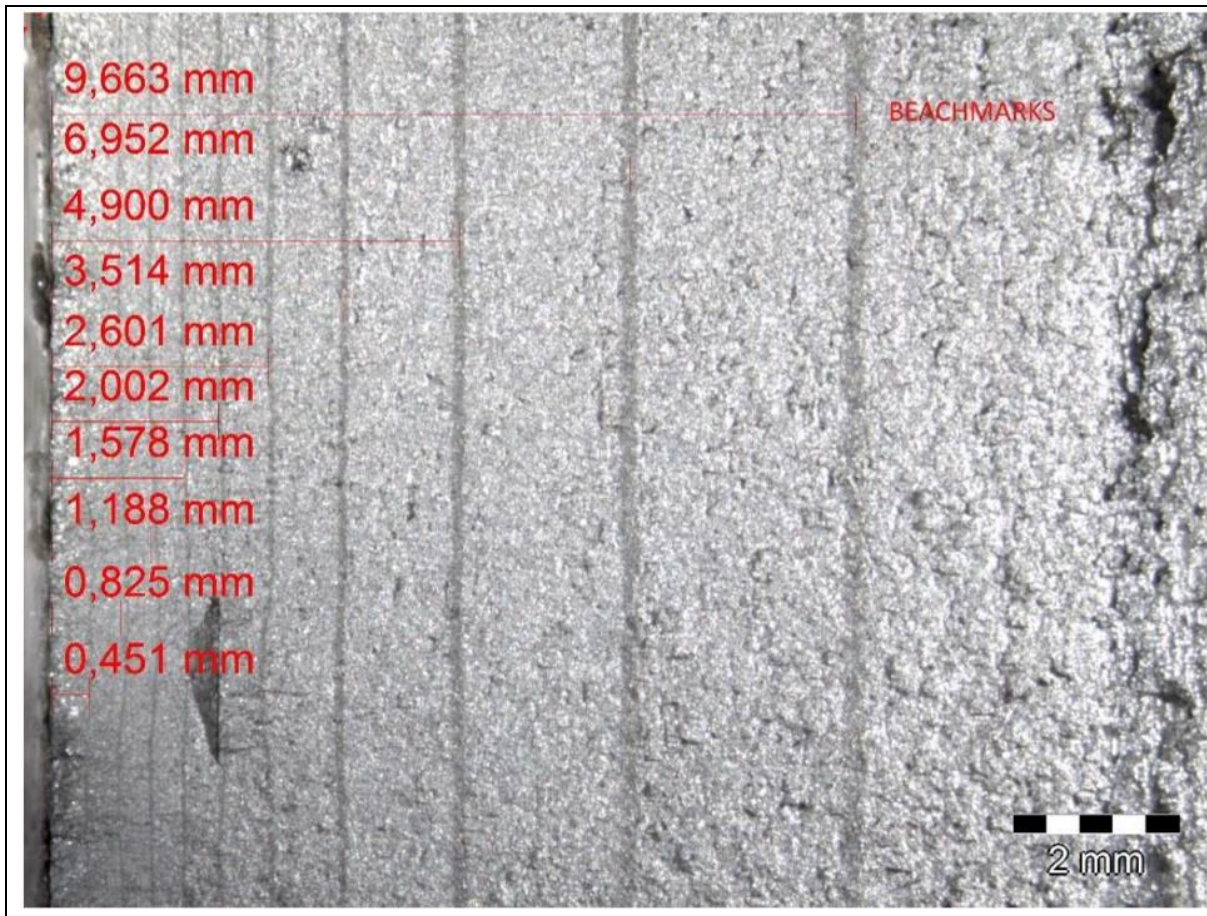| R=0.0	*FRACTURE CRITERION, TYPE=fatigue, MIXED MODE BEHAVIOR=POWER, TOLERANCE=0.001 0.001,0, 28.87E-06,1.5,0,0.85, 11.9, 11.9 11.9,1,1,1

B. Beach mark measurement

Figure B.8.1 Beach mark measurement by microscope [25]

C. Traffic distribution

Table C.8.4 NEN 8701: Period 1972-1990

Period	1972-1990	10582163	cycles
Average cycles per year		556956	cycles
Reference Year		1981	
High Traffic: Cycles per year		83543	cycles

Type	Long Traffic %	Wheel type	Wheel load(KN)	Cycles
V11	10	A	35	8354
		B	25	
V12	10	A	45	8354
		B	31.25	
		B	25	
T1102	25	A	35	20886
		B	27.5	
		B	21.25	
		B	21.25	
T1103	50	A	40	41772
		B	31.25	
		B	22.5	
		B	22.5	
		B	22.5	
T1203	5	A	40	4177
		B	22.5	
		B	28.75	
		B	26.25	
		B	26.25	
		B	26.25	

Table C.8.5 NEN 8701: Period 1991-2010

Period	1991-2010	20747690	cycles
Average cycles per year		1037384	cycles
Reference Year		2000	
High Traffic: Cycles per year		155608	cycles

			High	
Type	Long Traffic %	Wheel type	Wheel load(KN)	Cycles
V11	10	A	35	15561
		B	25	
V12	10	A	45	15561
		B	31.25	
		B	25	
T1102	25	A	35	38902
		B	27.5	
		C	42.5	
		C	42.5	
T1103	50	A	40	77804
		B	31.25	
		C	45	
		C	45	
		C	45	
T1203	5	A	40	7780
		B	22.5	
		B	28.75	
		B	26.25	
		B	26.25	
		B	26.25	

Table C.8.6 NEN 8701: Period 2011-2040

Period	2011-2040	64726301	cycles
Average cycles per year		2157543	cycles
Reference Year		2025	
High Traffic: Cycles per year		323632	cycles

			High	
Type	**Long Traffic %**	**Wheel type**	**Wheel load(KN)**	**Cycles**
V11	10	A	35	32363
		B	25	
V12	10	A	45	32363
		B	31.25	
		C	50	
T1102	20	A	35	64726
		B	27.5	
		C	42.5	
		C	42.5	
T1103	50	A	40	161816
		B	31.25	
		C	45	
		C	45	
		C	45	
V12A12	5	A	45	16182
		B	31.25	
		C	47.5	
		C	50	
		C	42.5	
		C	42.5	
T1203A2	5	A	45	16182
		B	22.5	
		B	28.75	
		C	52.5	
		C	52.5	
		C	52.5	
		C	42.5	
		C	42.5	

D. Fatigue detail category

Table D.8.7 Fatigue detail category

| Source	Detail Category	Structural Detail	Description
Eurocode 3: Design of steel structures - Part 2: Steel bridges [44]	71		Weld connecting deck plate to trapezoidal ribs; Partially penetrated weld with a>t; Nominal Stress range assessment
NEN-EN 1993-1-9+C2 [44]	125		Calculated as nominal local stress on the underside of the cover plate at the crack initiation point, calculated with a 3D model
M.H. Kolstein [43]	125		Cracking in the deck plate; Assessment based on the nominal stress range in the deck plate
IIW Recommendations for fatigue design of welded joints and components [30]	FAT 100		Ends of the longitudinal stiffeners; Fillet welded; Fatigue resistance against hotspot stresses
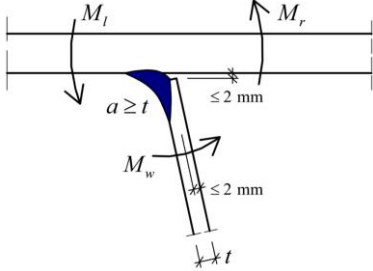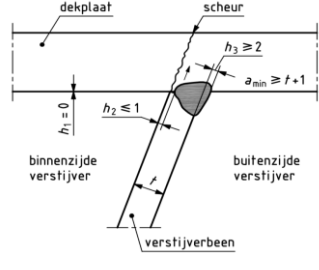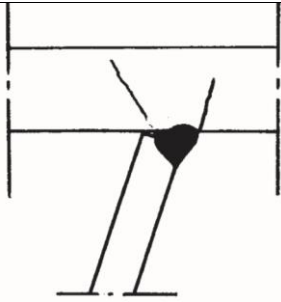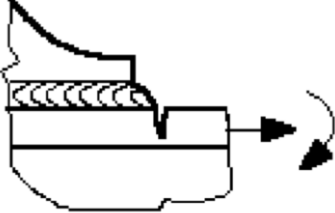
E. TOFD result
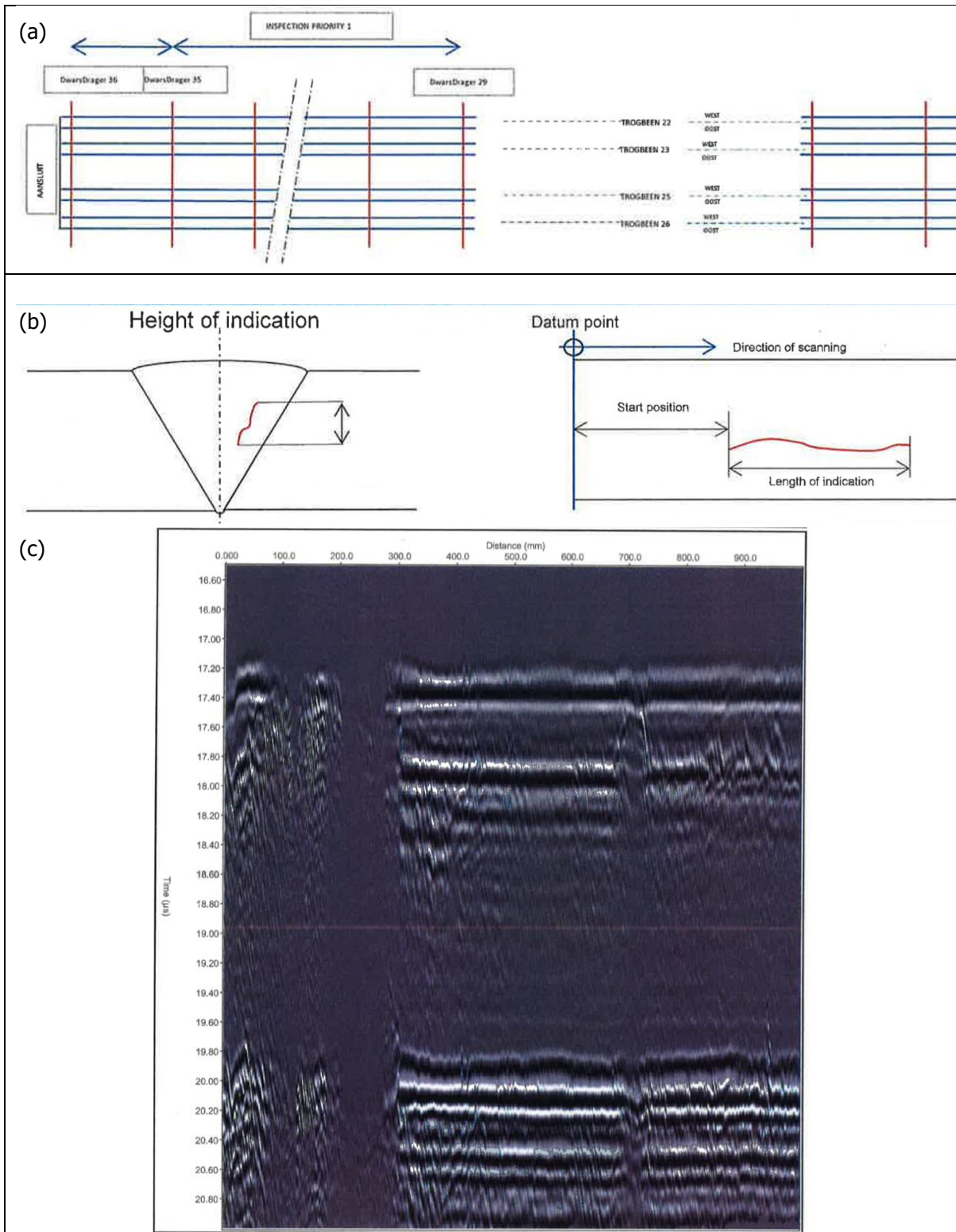
Figure E.8.1 (a) Illustration of location (top view) of TOFD measurement using skectches (b) Explanation of crack detection of TOFD method using sketches (c) TOFD scan [45]